A FINITE-ELEMENT METHOD FOR THE SOLUTION OF TURBINE-GENERATOR END-ZONE FIELDS

by

THOMAS WILLIAM PRESTON

Submitted for the Degree of Master of Philosophy

at

The University of Aston in Birmingham

September 1974

SUMMARY

The growth of demand for electrical power has led to large increases in the unit ratings of turbine-generators; typically, maximum 2-pole ratings have increased from 100 MW 20 years ago, to 660 MW today, with 1300 MW units being seriously considered.

The growth in unit output has been made possible by major improvements in design, particularly the introduction of direct cooling of the windings, which has allowed the electric loading to be greatly increased. The end-region flux densities have increased in consequence, and core end-heating and end-winding forces are major factors to be considered in the design. It is thus essential to be able to calculate end-zone fields accurately.

This thesis describes a finite-element method of predicting fields in the air space, allowing for complexities of boundary geometry. To economise in computer store, it is assumed that all functions vary sinusoidally in the peripheral direction, so that the 3-dimensional problem can be treated by a "quasi-3-dimensional" method, involving radial and axial distances only. The solution is obtained as a scalar potential distribution, from which the component flux densities can be derived.

Following proving of the method by application to problems for which analytic solutions exist, flux density distributions have been calculated for a short-core replica of a 500 MW generator and a production 660 MW generator. Agreement with test results is good.

Finally, the value of the method has been demonstrated by application to problems arising in the end-zone design of superconducting field and fully slotless generators.

ACKNOWLEDGMENTS

The work presented in this thesis was carried out at the Stafford Laboratory of G.E.C. Power Engineering Limited, Stafford, under the supervision of Mr. A.B.J. Reece, Head of Electromagnetics Section. The author is extremely grateful to him for his advice and encouragement throughout the whole project. The author is indebted to Professor E.J. Davies for suggesting the suitability of the work for a Master of Philosophy thesis, and to Dr. M. Jevons for his interest and valuable advice. He wishes to express his gratitude to the Management of the Stafford Laboratory, especially Mr. V.A. Hughes, for allowing him to present this work, and to Mr. A. Hunt, Chief Engineer of the Generator Division of G.E.C. Turbine Generators Limited, for permitting the inclusion of Company information. Thanks are also due to Miss A.G. Harrower for typing the thesis at such short notice.

Finally, the author wishes to express special thanks to his wife for her encouragement and forbearance over the last two years.

INDEX

LIST OF SYMBOLS

(S.I. Units are used)

$\bar{A}$ - vector magnetic potential

$\hat{A}_{i,j,m}$ - peak vector magnetic potential at the nodes of the general triangle

$\hat{A}_{r,z,\theta}$ - peak radial, axial and peripheral components, respectively, of vector magnetic potential

$\bar{B}$ - flux density

$B_{r,z,\theta}$ - instantaneous radial, axial and peripheral flux densities respectively

$\hat{B}_1$ - peak load flux density

$\hat{B}_n$ - peak normal component of flux density

$\hat{B}_{oc}$ - peak open-circuit flux density

$\hat{B}_{r,z,\theta}$ - peak radial, axial and peripheral components, respectively, of flux density

$\hat{B}_{sc}$ - peak short-circuit flux density

C_1 - $\frac{\text{rotor fundamental mmf}}{\text{rotor peak mmf}}$

E - induced voltage (rms)

$\bar{H}$ - magnetic field intensity

$\hat{I}$ - peak conductor current

I_{rms} - stator winding current (rms)

I_r - rotor winding current

$\bar{J}$ - current density

$\hat{J}_{r,z,\theta}$ - peak radial, axial and peripheral current densities, respectively, in the stator or rotor windings

K_d - distribution factor

K_w - winding factor

R - stator resistance

R_1 - rotor radius

R_2 - stator radius

T_{ph} - turns per phase

T_r - rotor turns per pole

U - peak scalar magnetic potential

U' - instantaneous value of scalar magnetic potential

$U_{i,j,m}$ - peak scalar magnetic potential at the nodes of the general triangle

V - terminal voltage

X_1 - stator leakage reactance

X - functional in terms of scalar magnetic potential

$X_{r,z,\theta}$ - functional in terms of the radial, axial and peripheral components, respectively, of vector magnetic potential

a_{ij} - general term in coefficient matrix

d - depth of penetration $\left\{= \sqrt{\frac{\rho}{\mu_o \mu_r \omega}}\right\}$.

d_r - axial length of bent portion of rotor winding

d_s - length of straight portion of stator end-winding

d_w - axial length of evolute of stator end-winding

n - number of unknown scalar magnetic potentials

p - pole pairs

r - radial distance

$r_{i,j,m}$ - radial co-ordinates of nodes i, j and m, respectively, of the general triangle

$\underline{r}$ - unit radial vector

v - harmonic order

x - distance in 'x' direction

y - distance in 'y' direction

z - axial distance

$z_{i,j,m}$ - axial co-ordinates of nodes i, j and m, respectively, of the general triangle

$\underline{z}$ - unit axial vector

Δ - area of triangle

ΔU - scalar magnetic potential difference

θ - peripheral distance

$\underline{\theta}$ - unit peripheral vector

μ_o - permeability of free space, $4\pi \times 10^{-7}$

μ_r - relative permeability of magnetic material or screen

ρ - resistivity of screen material

ρ' - fractional coil pitch

ω - angular velocity

CHAPTER 1

INTRODUCTION

1.1 General Remarks

The increasing demand for electric power has led to the production of turbine-generators of larger unit rating. The dramatic increase in turbine-generator capacity over the last thirty years is shown in Fig. 1.1:

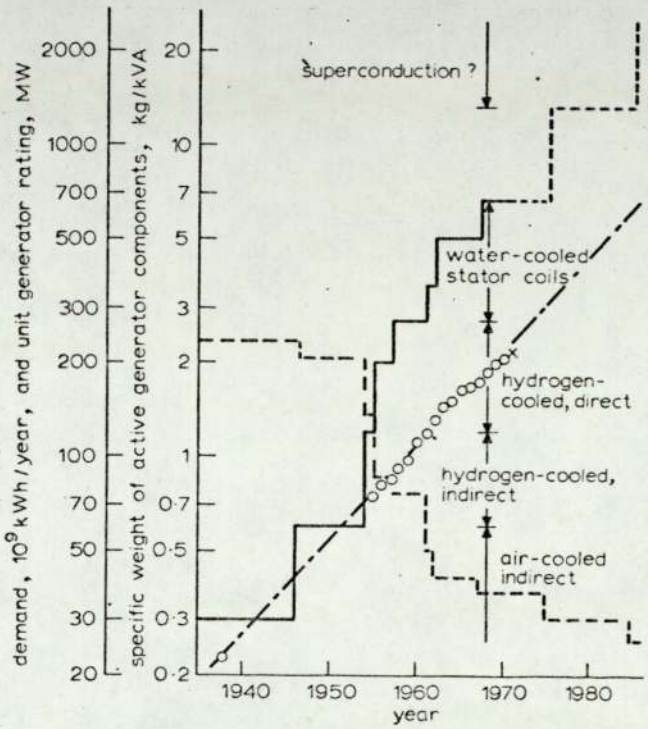

Sales of electricity (excluding Northern Ireland):
O *Reference 1*
× *Reference 2 (adjusted)*
—— *unit-generator rating, detailed design*
----- *specific weight of active components*

Fig. 1.1: Growth of electricity supply in U.K. since 1938 (Ref. (1))

In 1940, the rating of new sets was 30 MW; by 1960 this had risen to 270 MW, and at present 660 MW units are being commissioned in the United Kingdom, with serious thought being given to 1300 MW sets.

The increase has been made possible by major advances in design, particularly in the cooling of windings: this has led to a decrease in the active weight per unit power, also shown in Fig. 1.1.

The improvements made in cooling have allowed the electric loading to treble in the last ten years, and normal design methods have

not always been adequate to deal with the problems associated with the higher loadings.

1.2 Problems associated with the End-region

The higher outputs and electric loadings have created a particular design problem in the end-region, shown in Fig. 1.2. The main cause is the increase in the fringe and leakage fluxes, due to the larger air-gap and stator currents respectively. The increase in fluxes has the following effects in the end-region:-

(i) The eddy current losses in the stator core end-iron are a consequence of end-region fluxes normal to the core end-surface. These losses are mainly associated with the toothed region, since the core-back portion of the laminations is usually protected from the fluxes by a copper screen, as shown in Fig. 1.2. Excessive temperatures have occurred in the stator core due to these fluxes, and in some cases partial rebuilding of the core-end has been necessary. The losses increase still further on leading power factor operation, as is now required, at times, for turbine-generators connected to the 400 kV system.

(ii) The end-winding forces, which are proportional to the product of local leakage flux density and current, and hence to $(\text{current})^2$, have increased considerably with the higher electric loadings. The forces exerted on the end-windings of a 500 MW generator, under short-circuit conditions, can be as high as 400 kN/m, which is about 7 times the value for generators built ten years ago. As a result of these exceptionally large forces, and fatigue failures associated with the much smaller normal load forces, the end-winding bracing system has had to be re-designed.

(iii) The end-winding leakage reactance contributes about 25% and 15% to the sub-transient and transient reactances respectively, and is directly dependent upon the leakage flux distribution. It is important that these reactances are accurately known, so that the

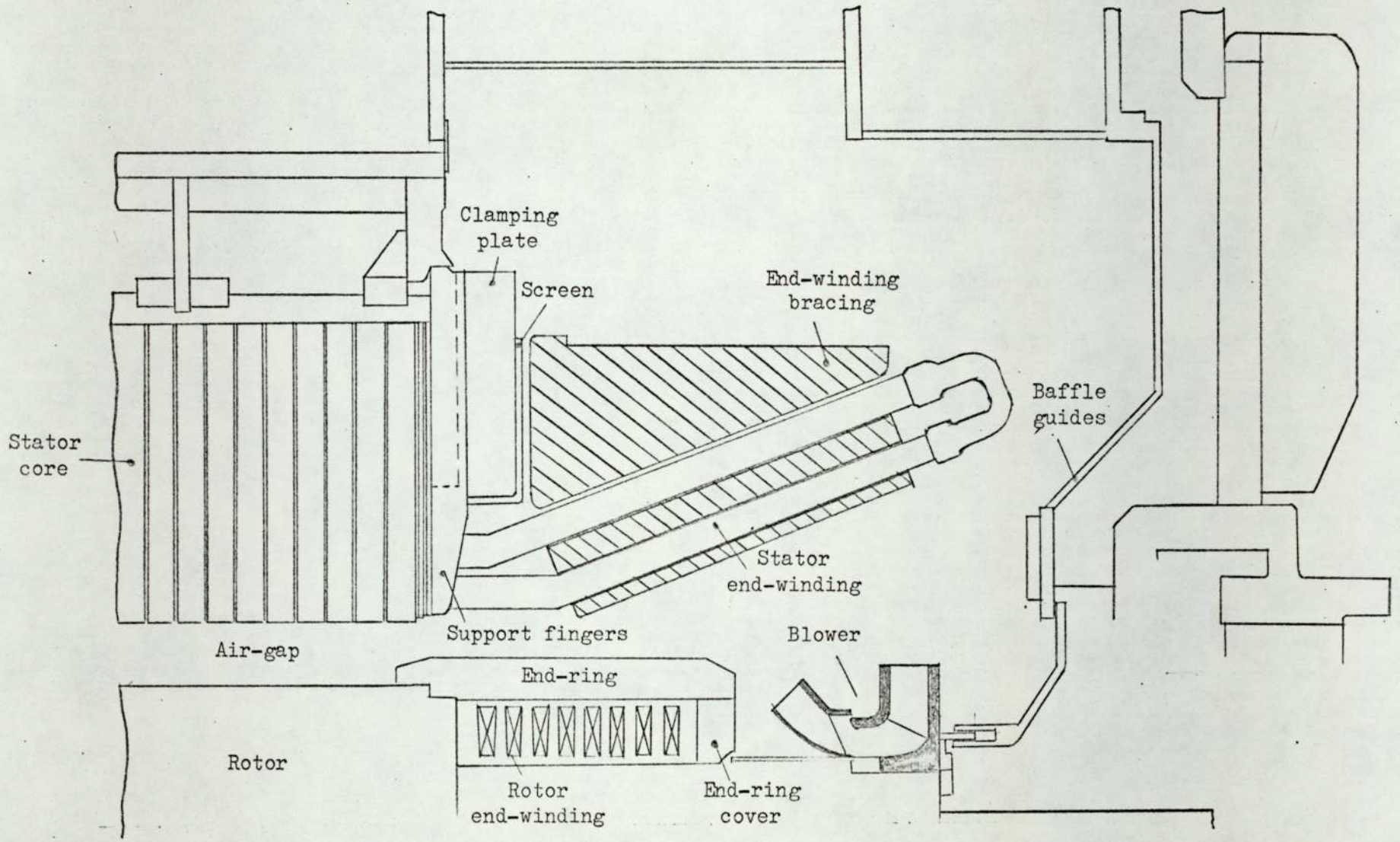

Fig. 1.2: End-region of a 660 MW turbine-generator

maximum switchgear ratings and the system stability can be determined.

(iv) Losses caused by eddy currents flowing in individual strips, and between strips, of the stator winding will increase as a result of the higher leakage fluxes.

If the eddy current losses, end-winding forces and reactances are to be controlled, it is essential to derive accurately the flux distribution within the end-region, allowing for the distributed winding, geometrically complicated boundaries, different types of boundary conditions, and internal conducting members, such as screens, clamping plates, etc.

1.3 Review of Previous Work

1.3.1 General

There are several possible approaches to the solution of the field distribution within the end-region, viz.:

(i) Analytic

(ii) Analogue

(iii) Numeric

1.3.2 Analytic

The mathematical approach involves the solution of Laplace's equation between two concentric cylinders, normally the outer casing and rotor shaft. Some examples are described in Refs. 2 - 9, where the main differences in approach are in the treatment of the stator and rotor windings and the surface boundary conditions.

An early contribution was made by Smith[2], whose object was to calculate the end-winding reactance of turbine-generators. He used the scalar magnetic potential approach, and the winding currents were represented by current sheets having axial and peripheral currents only. These currents were simulated by a potential difference between the surface of a magnetically

insulating shell, which divided the end-region into two zones. The potential difference distribution was represented by a double Fourier series, and the separation of variable method was used to solve Laplace's equation for the potential in each zone. All outer boundaries were assumed to be infinitely permeable, except the stator core-end-surface, which was treated as a screen to magnetic flux.

Honsinger[3,4] used a similar treatment to establish relationships for the end-winding reactance of an induction motor; however, all boundaries were treated as infinitely permeable, and the results were presented in the form of generalised curves. An approximate allowance was made for finite conductor dimensions.

Reece and Pramanik[5] followed a similar approach, but pointed out inaccuracies in both the Smith and Honsinger treatments of the potential difference set up by the current sheet. They derived the flux distribution within the end-region, using a scalar potential approach with all the outer boundaries treated as infinitely permeable; it was mentioned that the core-end-surface could also be treated as a screen to magnetic flux. Air-gap fringing was allowed for approximately by the use of fictitious coils on the core-end-surfaces.

Hammond and Ashworth[6] used a vector potential approach to give the potential distribution due to "coils" with axial, radial, or peripheral currents. The windings were modelled from a series of cylindrical- and disc-shaped coils, and their individual fields added to give the resultant. However, in this approach, all iron boundaries were ignored. Tegapoulos[7] extended this work by allowing approximately for all containing boundaries.

Lawrenson[8] determined the flux density within the end-region by summing the contribution of small elements of the end-winding, using the Biot-Savart law. This technique allows the end-winding

shape to be treated accurately, but it is difficult to take account of boundaries other than the plane formed by the core-end-surfaces. The method is essentially a computer method, since numerous calculations are required to determine the density within the end-region. Tegapoulos[9] reduced the number of calculations required by approximating the shape of the end-windings.

1.3.3 Analogue

Analogue studies have generally used an electrolytic tank or conducting paper (Teledeltos), but hand flux-plotting techniques have been used, for example, by Darrieus[10]. Winchester[11] modelled the assumption of sinusoidal variation of all functions around the periphery by a wedge-shaped electrolytic tank, with source voltages on the sides of the wedge. The screen and clamping plate were represented, and losses in the screen were obtained. Although Teledeltos paper has been used for many years, Hawley et al[12] were the first to publish any extensive work on its application to the end-region of the turbine-generator. Results showed reasonable agreement with test values.

Oberretl[13] improved the analogue representation of the end-region by simulating the magnetic non-linearity of the stator core and eddy currents with a network consisting of semiconductor diodes, capacitors and resistors.

1.3.4 Numeric

With the availability of large fast digital computers, numerical methods have tended to replace both the analytical and the rather cumbersome analogue methods. One of the first attempts to use the numerical approach for the end-region studies was made by Sarma et al[14]. The paper describes a 3-dimensional, vector potential solution for the distribution of fluxes in the end-region of a homopolar machine. Although the boundaries and the excitation windings were represented reasonably accurately,

it was difficult to specify the boundary conditions on the outer surfaces, because of the use of the vector potential. A major disadvantage of this approach was the large number of nodes, about 12,000, which were needed to represent the end-region in detail. This proved expensive because the computer times involved were large.

Okuda[15] made use of Winchester's assumption of sinusoidal variation of all functions peripherally to reduce the numerical study from three to two dimensions. This greatly reduced the number of nodes required to detail the end-region, as only the radial-axial plane needed defining. A finite-difference approach was used to determine the vector potential distribution, but the outer boundary conditions had to be simplified, as in the work of Sarma et al. This problem was overcome by Nomura[16], who formulated the same problem in scalar potential terms.

1.4 Solution Method selected

If larger unit rating turbine-generators are to be built with confidence, designers must be able to determine accurately the distribution and magnitude of the end-zone fluxes.

Analytical approaches have proved useful in the past, but they can only deal with problems with simple boundaries, and therefore, in general, cannot give the accuracy required. Whilst analogue methods can readily deal with mixed boundary conditions and irregular boundaries, they tend to be expensive, and an experienced operator is essential. The numerical method is normally more convenient than the analogue method, and complicated boundaries and internal members can be represented without much difficulty. Although the full 3-dimensional numerical solution of the end-zone would be very expensive, substantial economy can be obtained by using Winchester's assumption of sinusoidal variation of all functions peripherally, i.e. by a quasi-3-dimensional approach. This reduces the problem to a 2-dimensional study.

The quasi-3-dimensional scalar potential numerical approach is the basis for the work described in this thesis, with the finite-element method being preferred to the finite-difference method used by Nomura. The advantages of the finite-element method are:

(i) Regions of particular interest, such as the stepped portion of the stator-core end-surface, have to be greatly refined so as to determine accurately the rapidly varying distribution of flux densities caused by irregularities in the boundary surfaces. This refinement is not needed in less important regions, and can be avoided by the finite-element method, as shown in Fig. 1.3:

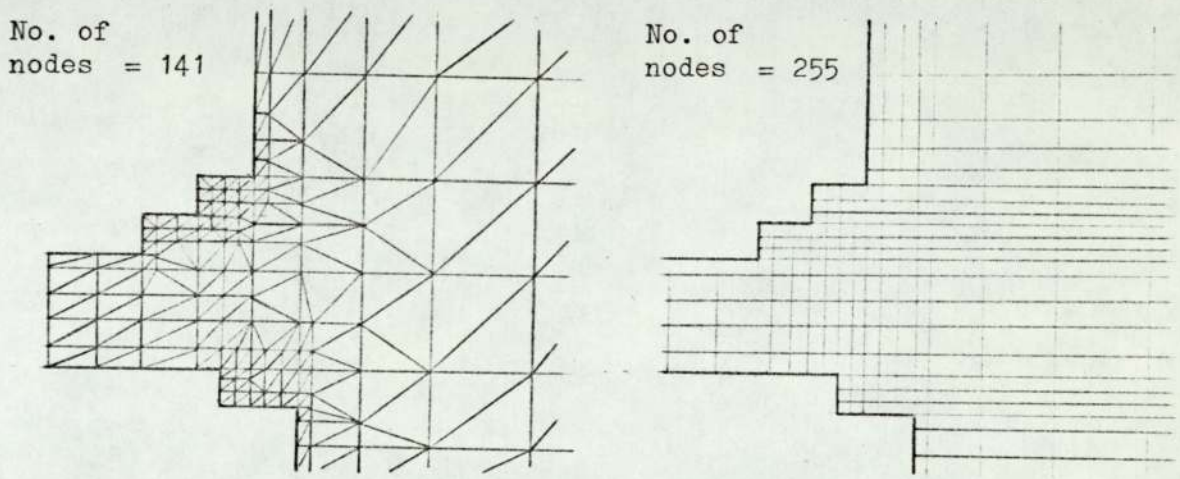

Fig. 1.3: Finite-element representation — Finite-difference representation

(ii) Non-radial and axial boundaries can be easily represented without special treatment.

(iii) Iron-air boundaries can be simply represented by allocating the appropriate permeability to the elements on either side of the boundary concerned.

1.5 Purpose of Thesis

The thesis describes the development of a method for determining the distribution of flux densities in the end-region of a turbine-generator. Although vector potential and flux density solutions are considered, the method chosen is a quasi-3-dimensional scalar potential formulation, solved numerically by a finite-element approach.

Boundaries are treated as being infinitely magnetic or infinitely conducting. Internal regions of finite permeability are also represented.

The method has been tested on problems for which analytical solutions are available. As a further check, end-zone flux densities calculated by the method have been compared with some experimental values obtained on a replica of a 500 MW turbine-generator and a 660 MW production generator. The variation with power factor of flux density normal to the core-end-surface of a 660 MW generator is given.

The flux densities normal to the stator-core end-surface of superconducting field and fully slotless generators have also been obtained using this method.

CHAPTER 2

THE END-REGION AND ITS MATHEMATICAL REPRESENTATION

2.1 General

It was concluded in the previous chapter that a quasi-3-dimensional numerical treatment is the most suitable for determining the flux density distribution in the end-region of a turbine-generator.

Before establishing the numerical form of the electromagnetic equations, the end-region will be described, and the assumptions needed to enable mathematical modelling discussed.

2.2 End-region Description

The end-region, shown in Fig. 1.2, contains the stator and rotor end-windings, and is bounded by the stator and rotor end-surfaces, the shaft, the outer casing, and the end cover. (In this study, the end-region is regarded as extending into the air-gap, to a position where the axial flux is zero, i.e. where the effect of fringing is insignificant.)

The main components within the end-region which influence the flux distribution will be described in the following sections:-

2.2.1 Stator winding

The stator windings are normally of the 2-layer type, short-pitched, with two conductors per slot. The coil-ends are

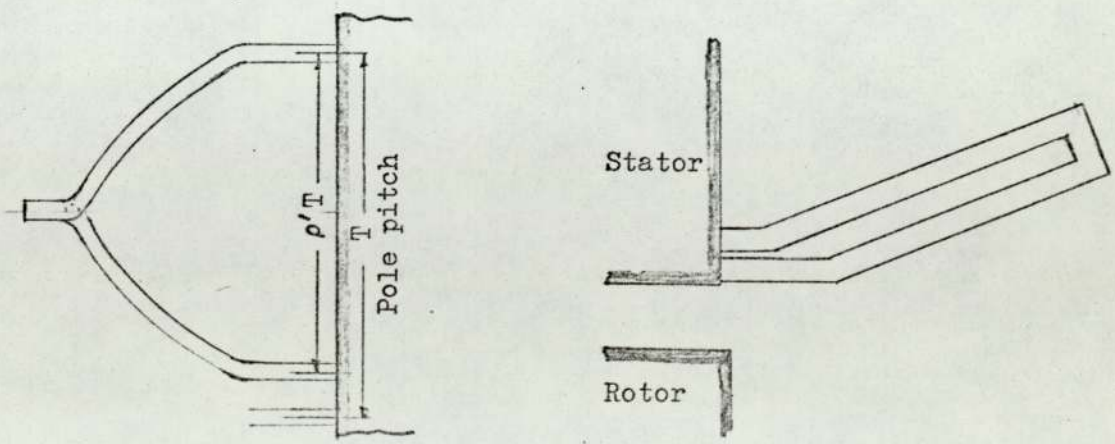

Fig. 2.1: Stator winding end-turn

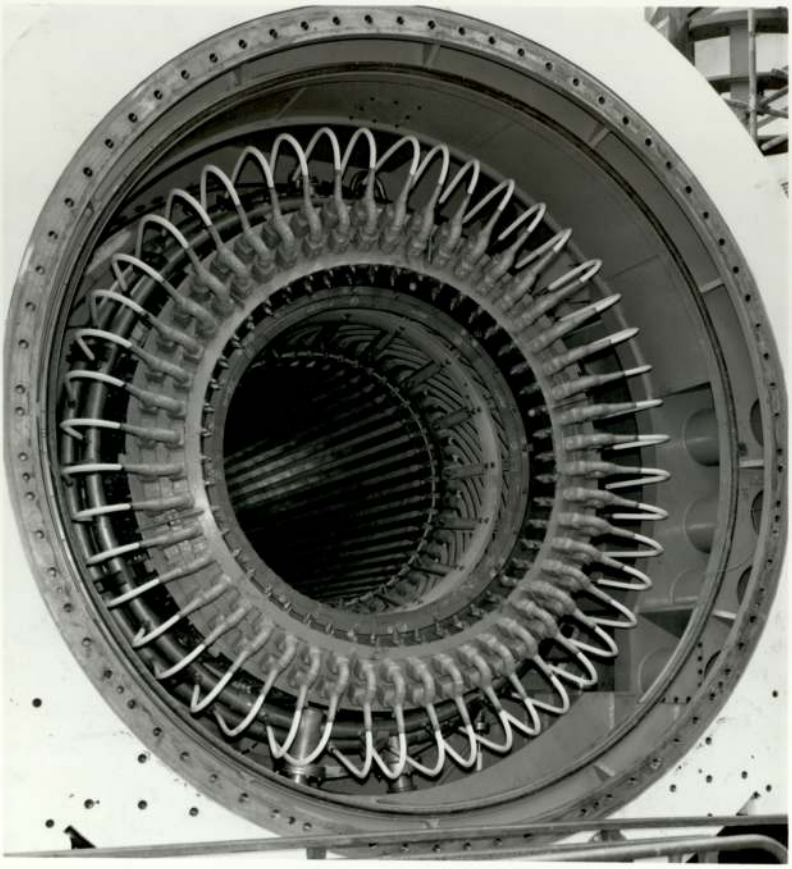

Fig. 2.2: Stator end-winding of a large turbine generator

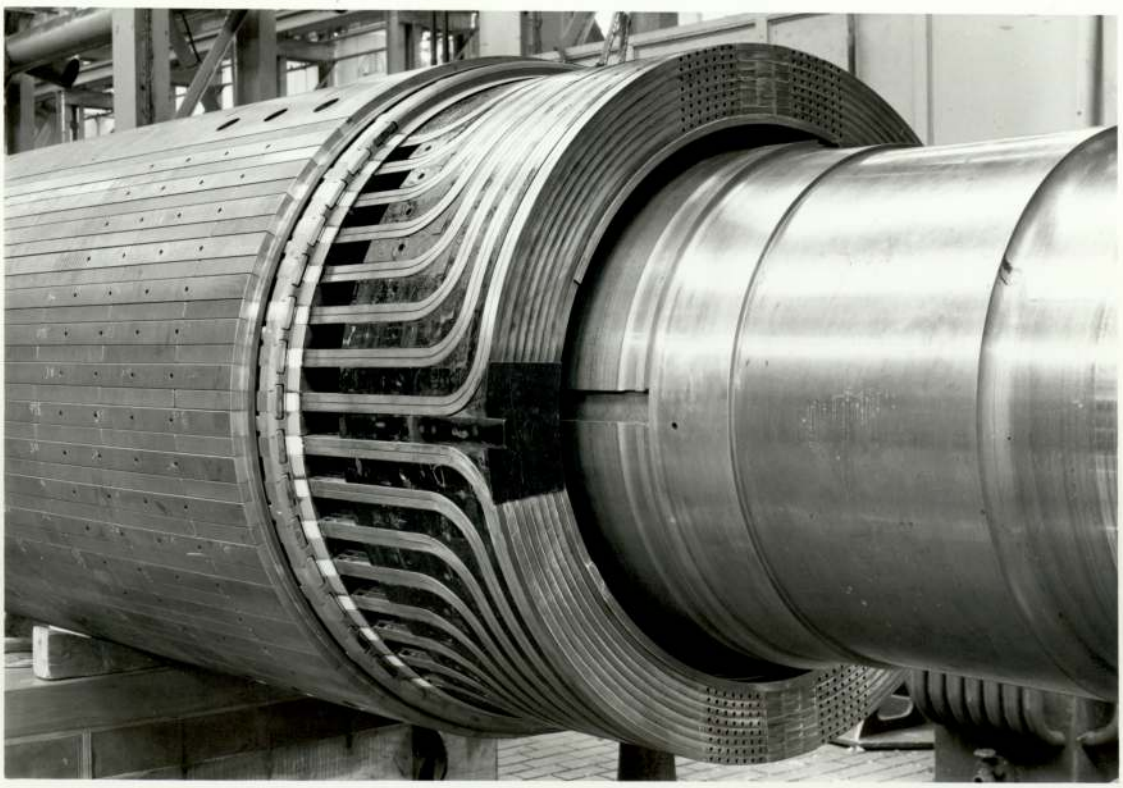

Fig. 2.3: Rotor end-winding of a large turbine generator

composed of short straight sections where the coil-sides emerge from the slots, joined by involute sections lying on the surface of a cone. Fig. 2.1 shows a developed view of a single stator conductor.

The complete assembly of conductors forms the conical shape as shown in Fig. 2.2.

Winding support members may be ignored, since they are non-magnetic and, in the main, non-conducting.

2.2.2 Rotor winding and end-ring

Fig. 2.3 shows the layout of the rotor coils, which are of the concentric type, lying on a cylindrical surface, and approximately rectangular.

The rotor end-windings experience large centrifugal forces, and movement radially outwards is restrained by a large metallic cylinder (the end-ring) normally shrunk onto the rotor end; the other end of the end-ring is supported on a magnetic ring (the end-ring cover). The end-ring is normally constructed from a non-magnetic material, to reduce rotor leakage and end-zone fluxes.

2.2.3 Clamping plate and support fingers

The combination of clamping plate and support fingers is used to compress and hold rigid the stator core, so as to reduce the core vibration set up by the main flux. Fig. 2.4 shows the position of the support fingers, which are recessed into the inner rim of the clamping plate and follow the profile of the stator teeth, as shown in Fig. 2.5. The fingers are constructed from a non-magnetic material, such as Nodumag, and are

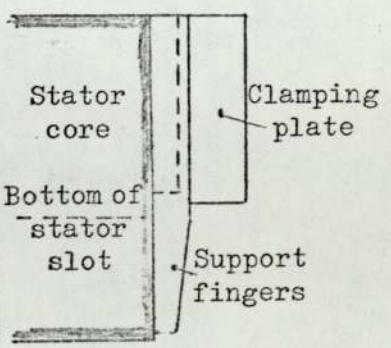

Fig. 2.4: Support finger arrangement

Fig. 2.5: Support fingers on a large turbine generator

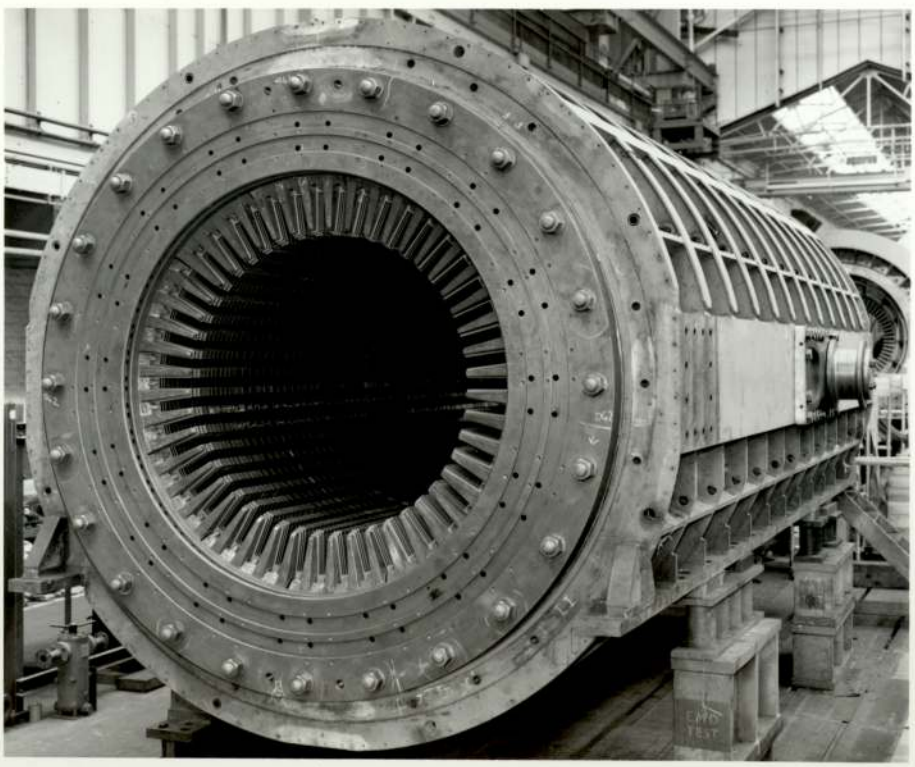

Fig. 2.6: Clamping plate on a large turbine generator

extended to the full depth of the stator core, behind the clamping plate, by thick radial members.

Fig. 2.6 indicates the arrangement of clamping plate and support fingers. The clamping plate may be of magnetic or non-magnetic material.

2.2.4 Screens

To prevent flux penetration into the end-laminations and the clamping plate (if magnetic), a copper screen is shaped around the clamping plate, as shown in Fig. 2.7. This tends to deflect the flux away from the stator-core end-region, and reduces the overall loss in the structural members, although substantial losses occur within the screen itself.

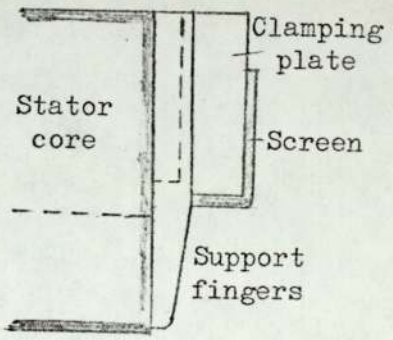

Fig. 2.7: Screen arrangement

Losses in the clamping plate can also be reduced by a high resistivity laminated flux diverter. This construction has been used by Westinghouse, but gives increased end-winding reactance.

2.3 Mathematical Representation of the End-region

2.3.1 General description

The method of end-field determination used in this thesis is based on the work of Nomura, but is solved numerically by the finite-element technique.

The reduction of the end-region from three dimensions to two dimensions is based on the assumption that the excitation currents, flux densities, etc., are sinusoidally distributed around the periphery. The validity of this assumption has been investigated experimentally by measurement of flux density around the periphery of the end-winding of a short-core replica of a

500 MW turbine-generator. The variations of measured flux densities normal to the inner stator winding surface are shown in Fig. 2.8, and are reasonably sinusoidal:

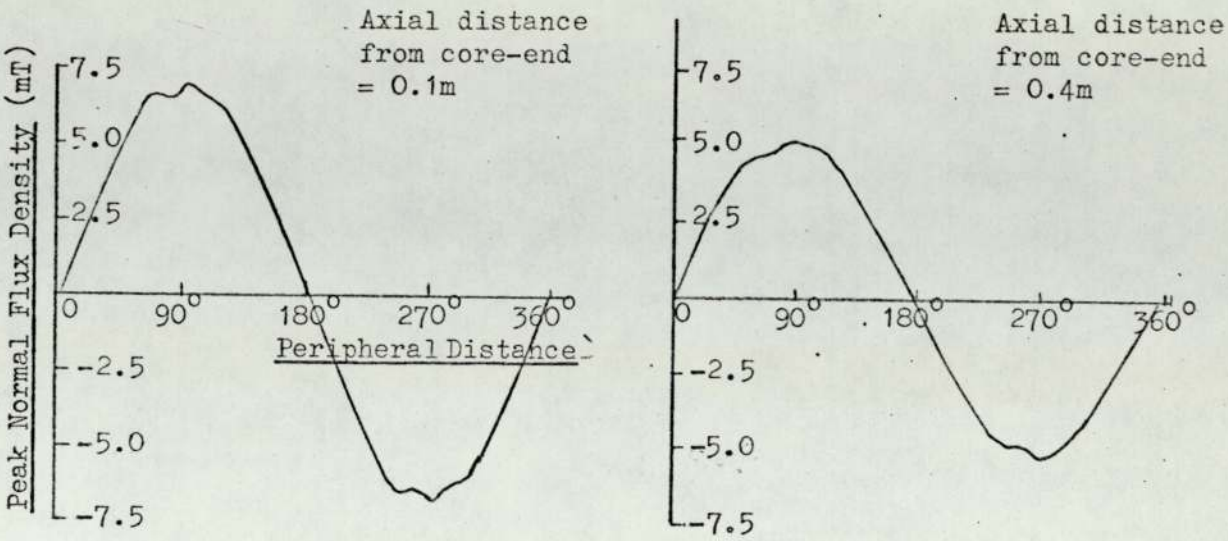

Fig. 2.8: Measured flux densities normal to the inner surface of the stator winding

This assumption reduces the problem to a 2-dimensional numerical solution of scalar potential within the end-region shown in Fig. 2.9:

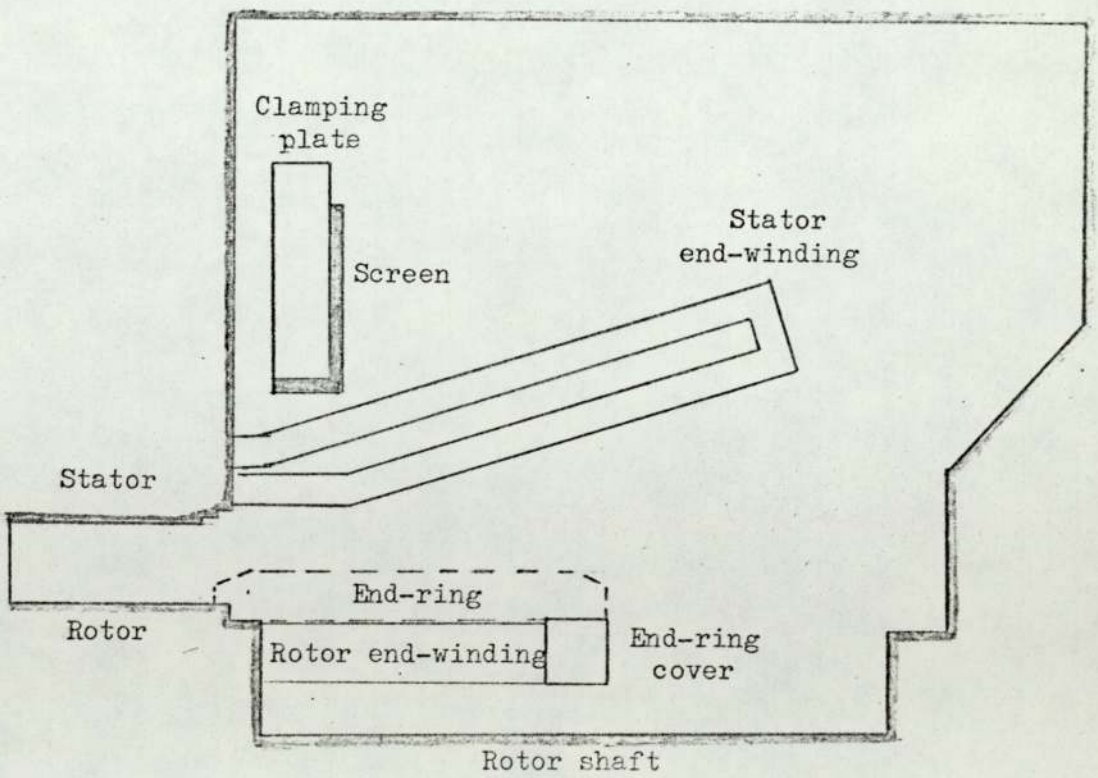

Fig. 2.9: Outline of end-region for solution purposes

The electromagnetic equations may be formulated in terms of:

(a) Vector potential

(b) Flux density

(c) Scalar potential

2.3.2 Vector potential solution

The vector potential approach was initially selected so that the excitation windings could be accurately represented, but a full analysis, given in Section 8.1, brought several disadvantages to light: these are:

(i) Three solutions are required to obtain the components of vector potential, which give directly the values $\hat{B}_z$, $\hat{B}_r$ and $\hat{B}_\theta$.

(ii) To calculate A_r, a gradient term, $\partial A_z/\partial z$, is needed so that discretisation errors from the A_z solution are introduced into the determination of A_r.

(iii) The boundary condition on the external surfaces cannot be defined in terms of any one component of potential, and, unless an iterative scheme is used, approximations are necessary.

2.3.3 Flux density solution

Formulation in terms of flux density eases the problem of specifying boundary conditions, but leaves the other disadvantages of the vector potential approach: this was not pursued further. A brief description of this approach is given in Section 8.2.

2.3.4 Scalar potential solution

The attraction of the scalar potential approach is the ease with which boundary conditions can be specified, and the economy resulting from the need to determine only one distribution. A disadvantage of the method is that current-carrying conductors

cannot be as accurately represented as with the vector potential approach, but it will be shown in Section 3.4.1 that this difficulty can be satisfactorily overcome. This was the method chosen to determine the distribution of fluxes within the end-region.

2.3.5 Equation of the end-region

In addition to the assumption of sinusoidal variation peripherally, the following assumptions are needed to enable the problem to be represented in a mathematical form:-

(i) Boundaries are represented as

either (a) infinitely permeable (the Dirichlet condition),

or (b) infinitely conducting, i.e. $\partial U/\partial n = 0$ (the Neumann condition).

(ii) Surfaces with induced currents are treated as infinitely-conducting surfaces.

(iii) Saturation of magnetic structures, such as the stator core, clamping plate, etc., is ignored.

Since there are no magnetic sources within the end-region, the divergence of flux density is zero, i.e.

$$\text{Div } \bar{B} = 0$$

In cylindrical co-ordinates, this expands to:

$$\frac{\partial B_r}{\partial r} + \frac{B_r}{r} + \frac{1}{r}\frac{\partial B_\theta}{\partial \theta} + \frac{\partial B_z}{\partial z} = 0 \qquad \ldots\ldots (2.1)$$

where: $B_r = \hat{B}_r \sin p\theta$

$B_z = \hat{B}_z \sin p\theta$

$B_\theta = \hat{B}_\theta \cos p\theta$

p = number of pole pairs

Scalar potential U' is related to $\bar{B}$ by:

$$\bar{H} = -\text{ grad } U' \qquad \ldots\ldots (2.2)$$

$$\bar{B} = \mu_o \mu_r \bar{H} \qquad \ldots\ldots (2.3)$$

From Eqns. (2.2) and (2.3) the following are derived:-

$$B_r = -\mu_o\mu_r \frac{\partial U'}{\partial r} \qquad \ldots\ldots (2.4)$$

$$B_\theta = -\frac{\mu_o\mu_r}{r} \frac{\partial U'}{\partial \theta} \qquad \ldots\ldots (2.5)$$

$$B_z = -\mu_o\mu_r \frac{\partial U'}{\partial z} \qquad \ldots\ldots (2.6)$$

Eqns. (2.4) - (2.6) are substituted in Eqn. (2.1) to give the scalar potential equation for the end-region as:

$$\mu_o\mu_r \left\{ \frac{\partial^2 U'}{\partial r^2} + \frac{1}{r}\frac{\partial U'}{\partial r} + \frac{1}{r^2}\frac{\partial^2 U'}{\partial \theta^2} + \frac{\partial^2 U'}{\partial z^2} \right\} = 0 \qquad \ldots\ldots (2.7)$$

The term $\mu_o\mu_r$ can be ignored if the region is homogenous, but in the end-region there are regions of different permeability, and for generality $\mu_o\mu_r$ is retained.

The scalar potential, U', can be written as:

$$U' = U(r, z) \sin p\theta$$

Eqn. (2.7) can then be reduced to its quasi-3-dimensional form, viz.:

$$\mu_o\mu_r \left\{ \frac{\partial^2 U}{\partial r^2} + \frac{1}{r}\frac{\partial U}{\partial r} - \frac{p^2}{r^2} U + \frac{\partial^2 U}{\partial z^2} \right\} = 0 \qquad \ldots\ldots (2.8)$$

This is the partial differential equation which describes the potential variation in the end-region.

2.4 Conclusions

The scalar potential approach has been selected to determine the flux distribution in the end-region because of the ease with which it can represent boundaries and the economy obtained in having to solve for only one component. A quasi-3-dimensional relationship has been derived for the scalar potential in the end-zone. This relationship is to be solved numerically by the finite-element method, and the following chapter details the development of the numerical equations.

CHAPTER 3

NUMERICAL FORMULATION

3.1 General

The partial differential equation describing the end-region scalar potential distribution has been derived in the previous chapter. This chapter derives the corresponding numerical equations for the finite-element solution, and describes the treatment of excitation windings and boundaries.

3.2 Finite-element Theory

3.2.1 Variational principle

The finite-element approach uses the Calculus of Variations to establish, from the governing differential equations, an integral, X, which, when extremised, gives the correct solution. The integral, which is a function of the unknown scalar potentials, is known as the "functional".

This can be written for the end-region problem in scalar potential terms as:

$$X = \iiint_V f\left\{r,\ \theta,\ z,\ U,\ \frac{\partial U}{\partial r},\ \frac{\partial U}{\partial \theta},\ \frac{\partial U}{\partial z}\right\} r\ dr\ dz\ d\theta \qquad \ldots\ldots\ (3.1)$$

The equation for the function inside the integral is obtained from the governing differential equations by using Euler's theorem.

This theorem, which is derived from the Variational Principle (Franklin[17]), states that the volume integral X will have a stationary value if the unknown function, $U(r, z, \theta)$, satisfies the following equation:-

$$\frac{\partial f}{\partial U} - \frac{\partial}{\partial r}\left\{\frac{\partial f}{\partial\left(\frac{\partial U}{\partial r}\right)}\right\} - \frac{\partial}{\partial \theta}\left\{\frac{\partial f}{\partial\left(\frac{\partial U}{\partial \theta}\right)}\right\} - \frac{\partial}{\partial z}\left\{\frac{\partial f}{\partial\left(\frac{\partial U}{\partial z}\right)}\right\} = 0 \qquad \ldots\ldots\ (3.2)$$

3.2.2 Determination of the functional for the end-region

The functional for the end-region problem is determined from Euler's theorem, as described in Section 8.3, giving:

$$X = \iiint_V \frac{\mu_o \mu_r}{2} \left[\left\{\frac{\partial U}{\partial r}\right\}^2 + \left\{\frac{\partial U}{\partial z}\right\}^2 + \frac{1}{r^2}\left\{\frac{\partial U}{\partial \theta}\right\}^2 \right] r \, dr \, dz \, d\theta \quad \ldots\ldots (3.3)$$

If correct, this should reduce to the energy equation for the end-region: this can be verified by recasting Eqn. (3.3) in terms of flux density, i.e.:

$$\left\{\frac{\partial U}{\partial r}\right\}^2 = \frac{B_r^2}{(\mu_o \mu_r)^2}$$

$$\left\{\frac{\partial U}{\partial z}\right\}^2 = \frac{B_z^2}{(\mu_o \mu_r)^2}$$

$$\frac{1}{r^2}\left\{\frac{\partial U}{\partial \theta}\right\}^2 = \frac{B_\theta^2}{(\mu_o \mu_r)^2}$$

Therefore substituting in Eqn. (3.3) gives:

$$X = \iiint_V \left\{ \frac{B_r^2}{2(\mu_o \mu_r)} + \frac{B_z^2}{2(\mu_o \mu_r)} + \frac{B_\theta^2}{2(\mu_o \mu_r)} \right\} r \, dr \, dz \, d\theta$$

which is the stored magnetic energy of the end-region.

Eqn. (3.3) is the functional for a fully 3-dimensional region, whose scalar potential distribution is described by Eqn. (2.7). However, the assumption made in Section 2.3.1 allows the end-region equations to reduce to the 2-dimensional form of Eqn. (2.8), giving:

$$X = \iint_S \frac{\mu_o \mu_r}{2} \left[\left\{\frac{\partial U}{\partial r}\right\}^2 + \left\{\frac{\partial U}{\partial z}\right\}^2 + \frac{p^2}{r^2} U^2 \right] r \, dr \, dz \quad \ldots\ldots (3.4)$$

(The term $\int d\theta$ introduces a constant, π, in the above equation, but can be ignored, as shown in Section 3.3.4.)

3.2.3 Extremised functional

The functional, Eqn. (3.4), is extremised by differentiating it with respect to the variable, U, and equating to zero:

$$\frac{\partial X}{\partial U} = \iint_S \frac{\mu_o \mu_r}{2} \frac{\partial}{\partial U} \left[\left\{\frac{\partial U}{\partial r}\right\}^2 + \left\{\frac{\partial U}{\partial z}\right\}^2 + \frac{p^2}{r^2} U^2 \right] r \, dz \, dr = 0 \quad \ldots\ldots (3.5)$$

The problem becomes one of deriving a variation of the unknown potential, U, in terms of r, z and θ, such that it satisfies Eqn. (3.5). This variation is solved numerically by the

finite-element method, and the following sections describe the development of these numerical equations for the end-region.

3.3 Numerical Formulation

3.3.1 General

The finite-element approach for determining the potentials requires a longitudinal section through the end-region to be sub-divided into elemental areas, such as triangles, rectangles, etc. A potential variation, defined by the corner node co-ordinates and potentials, is assumed over the elements. The numerical representation of the potential distribution is substituted into the functional equation, (3.4), which is then extremised with respect to potentials at all nodes, giving the numerical form of Eqn. (3.5). This results in an equation for every node, and the potential variation is determined by solving 'n' simultaneous equations with 'n' unknowns.

3.3.2 Element sub-division

The element used to sub-divide the end-region can be of many shapes, the simplest form being a triangle. This element is flexible enough to fit most irregular boundary shapes, and finer elements can be readily used where the potential field varies rapidly. Because there are only three nodes to consider, the

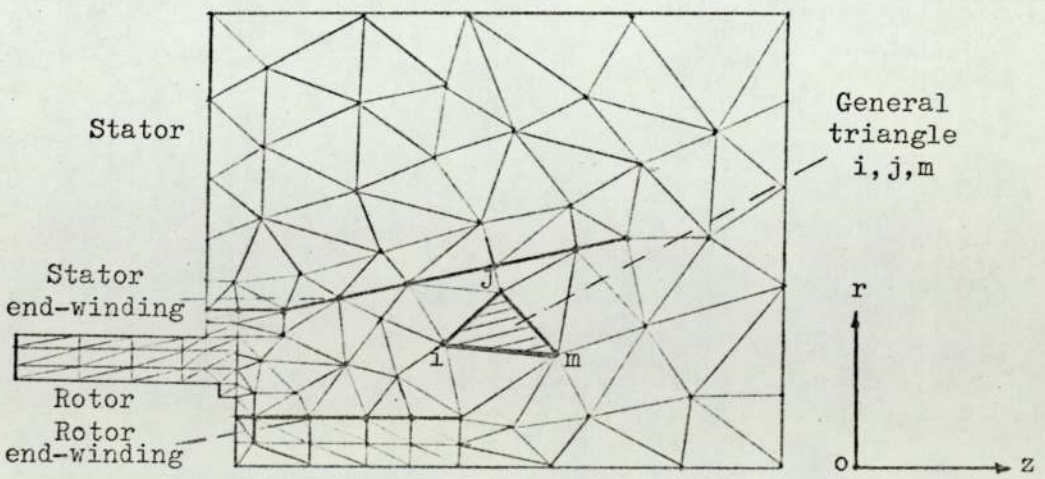

Fig. 3.1: Sub-division of an end-region by triangular elements

computational time required to determine the coefficients associated with the element is less compared with other types of element. This element is the type used in solving problems arising within this thesis, and Fig. 3.1 shows the triangular sub-division of an end-region.

3.3.3 Derivation of potential variation over an element

It is necessary to assume a function to describe the variation of potential within the element. This function is termed the "shape function", and is represented by a polynomial of an order consistent with the number of nodes available along any edge of a triangle, e.g. a linear polynomial requires two nodes per side, a quadratic three nodes per side. The higher the order of polynomial, the more complex become the numerical equations, but greater accuracy is obtained. Therefore, a balance of cost against accuracy must be achieved, and for a 2-dimensional study with simple boundary conditions, the linear polynomial suffices.

The linear variation of potential over a triangular element may be written as:

$$U = \alpha_1 + \alpha_2 r + \alpha_3 z \qquad \ldots\ldots\ldots (3.6)$$

where α_1, α_2 and α_3 are coefficients related to the nodal co-ordinates and potentials of the triangle concerned. These coefficients can be derived by substituting into Eqn. (3.6) the co-ordinates and potentials at each vertex, giving, for the general triangle of Fig. 3.1, the following:-

$$U_i = \alpha_1 + \alpha_2 r_i + \alpha_3 z_i$$

$$U_j = \alpha_1 + \alpha_2 r_j + \alpha_3 z_j$$

$$U_m = \alpha_1 + \alpha_2 r_m + \alpha_3 z_m$$

Solving for α_1 gives:

$$\alpha_1 = \frac{\begin{vmatrix} U_i & r_i & z_i \\ U_j & r_j & z_j \\ U_m & r_m & z_m \end{vmatrix}}{\begin{vmatrix} 1 & r_i & z_i \\ 1 & r_j & z_j \\ 1 & r_m & z_m \end{vmatrix}}$$

Therefore:

$$\alpha_1 = \frac{U_i(z_m r_j - z_j r_m) + U_j(z_i r_m - z_m r_i) + U_m(z_j r_i - z_i r_j)}{z_m(r_j - r_i) + z_i(r_m - r_j) + z_j(r_i - r_m)}$$

$$= \frac{a_i U_i + a_j U_j + a_m U_m}{2\Delta}$$

where: Δ = area of the triangle

$$= \frac{\{z_m(r_j - r_i) + z_i(r_m - r_j) + z_j(r_i - r_m)\}}{2}$$

$$a_i = z_m r_j - z_j r_m$$

$$a_j = z_i r_m - z_m r_i$$

$$a_m = z_j r_i - z_i r_j$$

Similarly for α_2 and α_3:

$$\alpha_2 = \frac{b_i U_i + b_j U_j + b_m U_m}{2\Delta}$$

where: $b_i = z_j - z_m$

$$b_j = z_m - z_i$$

$$b_m = z_i - z_j$$

and:

$$\alpha_3 = \frac{c_i U_i + c_j U_j + c_m U_m}{2\Delta}$$

where: $c_i = r_m - r_j$

$$c_j = r_i - r_m$$

$$c_m = r_j - r_i$$

Thus, if α_1, α_2 and α_3 are substituted into Eqn. (3.6), the potential distribution within any triangle becomes:

$$U = \frac{\{(a_i + b_i r + c_i z)U_i + (a_j + b_j r + c_j z)U_j + (a_m + b_m r + c_m z)U_m\}}{2\Delta} \quad \ldots\ldots (3.7)$$

where the terms $\frac{(a_n + b_n r + c_n z)}{2\Delta}$ are called the shape functions ($n = i, j$ or m).

3.3.4 Numerical equivalent of the extremised functional

The numerical equivalent of Eqn. (3.5) is obtained by substituting Eqn. (3.7) into the functional equation (3.4) and extremising with respect to potentials at all nodes. Thus extremisation at node 'i' of the general triangle in Fig. 3.1 is obtained by differentiating with respect to U_i, summing similar equations formed from connected triangles with node 'i', and equating to zero, i.e.:

$$\sum \frac{\partial X^e}{\partial U_i} = 0 \quad \ldots\ldots (3.8)$$

where $\sum$ represents the summation of all connected triangles.

The following example illustrates this:

Consider node 'i' in Fig. 3.2, then the complete variational equation for this node is:

$$\frac{\partial X_1}{\partial U_i} + \frac{\partial X_3}{\partial U_i} + \frac{\partial X_4}{\partial U_i} + \frac{\partial X_9}{\partial U_i} + \frac{\partial X_{12}}{\partial U_i} + \frac{\partial X_{30}}{\partial U_i}$$

$$= \sum \frac{\partial X^e}{\partial U_i}$$

$$= 0$$

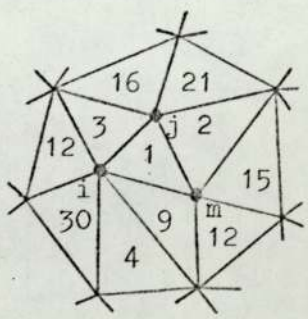

Fig. 3.2: Element array

The variational becomes, when expanded:

$$\sum \frac{\partial X^e}{\partial U_i} = \sum \iint_S \mu_o \mu_r \left[\frac{\partial U}{\partial r} \frac{\partial}{\partial U_i} \left\{ \frac{\partial U}{\partial r} \right\} + \frac{\partial U}{\partial z} \frac{\partial}{\partial U_i} \left\{ \frac{\partial U}{\partial z} \right\} + \frac{p^2}{r^2} U \frac{\partial U}{\partial U_i} \right] r \, dr \, dz$$

which gives, when substituting for U from Eqn. (3.7):

$$\begin{aligned} \sum \frac{\partial X^e}{\partial U_i} = \iint \frac{\mu_o \mu_r}{4\Delta^2} \Bigg[& r \left(b_i U_i + b_j U_j + b_m U_m \right) b_i \\ & + r \left(c_i U_i + c_j U_j + c_m U_m \right) c_i + \frac{p^2}{r} \left(a_i + b_i r + c_i z \right) \\ & \times \Big\{ \left(a_i + b_i r + c_i z \right) U_i + \left(a_j + b_j r + c_j z \right) U_j \\ & + \left(a_m + b_m r + c_m z \right) U_m \Big\} \Bigg] dr \, dz \end{aligned}$$

$$+ \text{ the contributions from the other associated triangles}$$

$$= 0 \qquad \ldots\ldots\ldots (3.9)$$

The integral over the area of the triangle is evaluated, as described in Section 8.4, and leads to the following numerical equation:-

$$\begin{aligned} \sum \frac{\partial X^e}{\partial U_i} = \frac{\mu_o \mu_r}{(2\Delta)^2} \Big\{ & \left(b_i^2 \bar{r} \Delta + c_i^2 \bar{r} \Delta + p^2 a_i^2 W + p^2 b_i^2 \bar{r} \Delta \right. \\ & \left. + p^2 c_i^2 S + 2p^2 b_i a_i \Delta + 2p^2 a_i c_i Q + 2p^2 b_i c_i \bar{z} \Delta \right) \\ & \times U_i + \left(b_i b_j \bar{r} \Delta + c_i c_j \bar{r} \Delta + p^2 a_i a_j W \right. \\ & + p^2 b_i b_j \bar{r} \Delta + p^2 c_i c_j S + p^2 a_j b_i \Delta + p^2 a_i b_j \Delta \\ & + p^2 b_i c_j \bar{z} \Delta + p^2 c_i b_j \bar{z} \Delta + p^2 c_i a_j Q \\ & \left. + p^2 a_i c_j Q \right) U_j + \left(b_i b_m \bar{r} \Delta + c_i c_m \bar{r} \Delta + p^2 a_i a_m W \right. \\ & \left. + p^2 b_i b_m \bar{r} \Delta + p c_i c_m S + p^2 b_i a_m \Delta + p^2 a_i b_m \Delta \right. \end{aligned}$$

$$+ p^2 b_i c_m \bar{z} \Delta + p^2 c_i b_m \bar{z} \Delta + p^2 c_i a_m Q$$

$$+ p^2 a_i c_m Q)U_m \Big\} + \text{similar expressions for}$$

other associated triangles

$$= 0 \qquad \ldots\ldots (3.10)$$

where: $Q = \iint \frac{z}{r} \, dr \, dz$ $\qquad \bar{r} = \frac{r_i + r_j + r_m}{3}$

$W = \iint \frac{1}{r} \, dr \, dz$ $\qquad \bar{z} = \frac{z_i + z_j + z_m}{3}$

$S = \iint \frac{z^2}{r} \, dr \, dz$

(From Eqn. (3.10) it can be seen that if one of the connecting triangles has a different μ_r, then it is wrong to ignore this term, whereas the μ_o and the π from the $\int d\theta$ are common to all triangles, and can be ignored.)

3.3.5 Development of matrix equation

An expression similar to Eqn. (3.10) is obtained for each node within the end-zone, so a set of simultaneous equations of 'n' unknowns are formed which can be represented in matrix form as follows:-

$$\begin{bmatrix} a_{11} & a_{12} & & \\ a_{21} & a_{22} & & \\ a_{31} & & a_{3j} & \\ \vdots & & \vdots & \\ a_{i1} & a_{i2} & a_{ij} & a_{ii} \\ & & & \\ & & & a_{nn} \end{bmatrix} \cdot \begin{bmatrix} U_1 \\ U_2 \\ \\ \\ U_i \\ \\ \\ U_n \end{bmatrix} = \begin{bmatrix} V_1 \\ \\ \\ \\ V_i \\ \\ \\ V_n \end{bmatrix}$$

Coefficient array — Unknowns — Source array

The matrix formed from the finite-element expressions is symmetric about the leading diagonal, as illustrated by the

following example:-

An equation similar to (3.10) is formed when extremising about node 1 of Fig. 3.3. This can be written in the following terms as:-

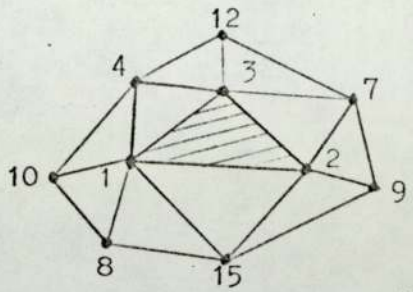

Fig. 3.3

$$a_{11}U_1 + a_{12}U_2 + a_{13}U_3 + a_{14}U_4 + a_{18}U_8 + a_{1,10}U_{10} + a_{1,15}U_{15} = 0$$

where a_{11} is the leading diagonal coefficient, and $a_{12} \cdots a_{1,15}$ are the sub-coefficients. Similarly, when considering node 2:

$$a_{21}U_1 + a_{22}U_2 + a_{23}U_3 + a_{27}U_7 + a_{2,9}U_9 + a_{2,15}U_{15} = 0$$

where a_{22} is the leading diagonal coefficient, and a_{21}, a_{23} ... $a_{2,15}$ are the sub-coefficients, but because the coefficients a_{12} and a_{21} are both dependent upon the same nodal positions 1 and 2, it can be easily shown from Eqn. (3.10) that:

$$a_{21} = a_{12}$$

and, similarly:

$$a_{31} = a_{13}, \text{ etc.}$$

This gives a symmetric matrix which facilitates the solution process.

The source terms of the matrix are derived from the end-winding excitation, and from nodes which form the boundary surfaces. These terms are discussed in the following section.

3.4 Winding Representation and Boundary Conditions

3.4.1 Stator and rotor winding currents

The scalar potential approach cannot treat the finite thickness of the conductor, but assumes that the excitation winding can be represented by an infinitely thin current sheet situated at the mid-depth of the actual conductor. (The depth of the conductor can be approximated by a series of such current sheets distributed across the depth.)

The current sheet is represented by an infinitely thin, magnetically insulating shell having a scalar potential difference (ΔU) between the shell surfaces. This is illustrated in Fig. 3.4 by the example of a single coil per pole. The coil is represented by a magnetically insulating shell, and the coil current is allowed for by making the outer and inner surfaces of the shell differ in potential by an amount corresponding to that produced by the coil. This is shown in Fig. 3.5, where the peak fundamental potential difference is given by:

$$\Delta U = \frac{4}{\pi} \hat{I} \sin p\theta$$

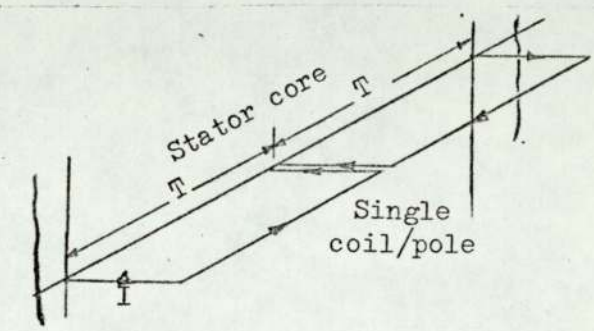

Fig. 3.4: Single coil per pole

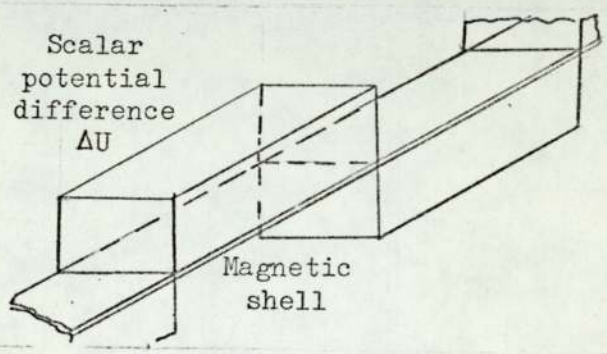

Fig. 3.5: Scalar potential equivalent of the single coil

The expressions for the ampere-turn distribution of the more complex stator and rotor end-windings of a turbine-generator have been derived by Tegapoulos[18], and are as follows:-

(i) Stator winding

The expression for ΔU is derived for a single current sheet, representing the 2-layer end-winding, as shown in Fig. 3.6.

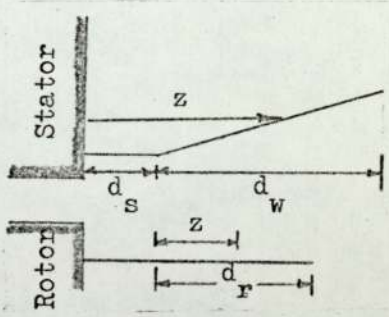

Fig. 3.6

The peak stator ampere-turns for the evolute section are given as:

$$\Delta U = \frac{2.7 \cdot I_{rms} \cdot T_{ph} \cdot K_d \cdot \sin}{poles} \left[\frac{\rho' \pi}{2} \left\{ 1 - \frac{(z - ds)}{dw} \right\} \right]$$

..... (3.11)

where: I_{rms} = stator terminal current

T_{ph} = turns per phase

K_d = distribution factor

ρ' = coil pitch factor

ds = axial length of straight portion of winding

dw = axial length of evolute portion of winding

Similar expressions, having sine and cosine components respectively, can be derived for the individual layers. This simple extension is discussed in Section 8.5.

(ii) Rotor windings

The peak rotor ampere-turns

$$= C_1 \cdot I_r \cdot T_r \cdot \frac{dr - z}{dr} \text{ (AT/pole)} \qquad \ldots\ldots\ldots (3.12)$$

where: C_1 = $\frac{\text{rotor fundamental mmf}}{\text{rotor peak mmf}}$

I_r = rotor current

T_r = rotor turns per pole

dr = axial length of bent portion of rotor winding

(iii) Numerical representation of winding currents

To represent the stator or rotor currents in finite-element form, nodes on triangles (Fig. 3.7) lying along either side of the magnetically insulating shell must not be linked in any way, except by the scalar potential difference ΔU. Thus:

U_a (outer) = U_b (inner) $\pm \Delta U$

(+ or - is used, depending on current polarity): U_a and U_b are potentials of adjacent nodes on either side of the insulating magnetic shell used to simulate the current sheet

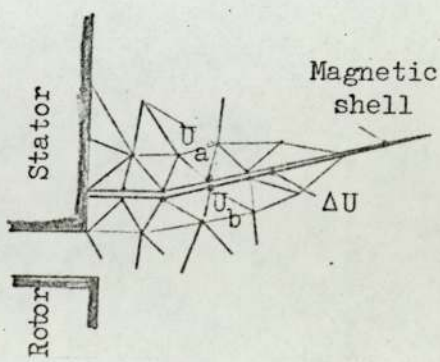

Fig. 3.7: Numerical representation of winding

3.4.2 Outer boundary - except air-gap boundary line

The nodes on the outer boundary can be expressed as a known scalar potential (the Dirichlet condition) related to the ampere-turns appearing across the air-gap. (The exception to this is where the boundary is treated as a screen.)

(i) Stator excitation only

In the air-gap region the difference of potential across the gap will be equal to the peak ampere-turns produced by the stator winding. Thus the stator surface up to the winding can conveniently be defined as having a potential equal to the mmf present on the straight surface of the winding, whilst the other surfaces will have a zero potential. The potential difference across the winding surface will fall off in accordance with Eqn. (3.11).

Fig. 3.8 shows that the boundary line A-B will have a maximum potential specified, and the boundary C-D a zero potential.

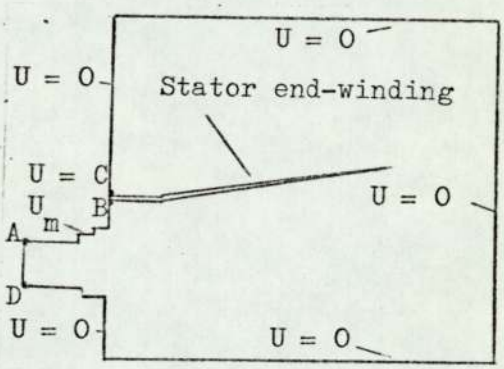

Fig. 3.8: Outline of end-region for stator only excitation

(ii) Rotor excitation only

Similarly, the peak ampere-turns produced by the rotor will set up a difference of potential, Eqn. (3.12), across the air-gap. Again, one surface can be expressed as a zero potential, and the other (rotor surface) assigned a potential equal to the rotor ampere-turns. The potential difference across the rotor winding falls off, as defined by Eqn. (3.12).

Fig. 3.9 shows the maximum potential boundary as line C-D, and the zero potential line as A-B.

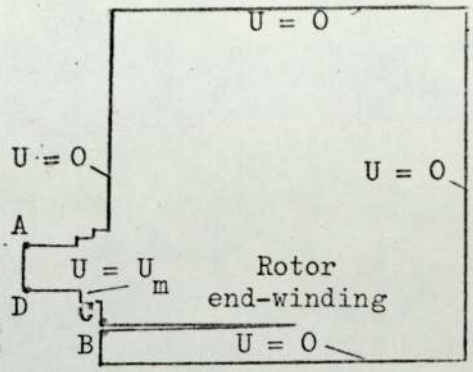

Fig. 3.9: Outline of end-region for rotor only excitation

3.4.3 Air-gap boundary line

The air-gap boundary line is taken at a position so far removed axially from the ends of the core that $\hat{B}_z$ can be taken as zero.

$$\therefore \quad \frac{\partial U}{\partial z} = - \hat{B}_z$$

$$= 0$$

It can be shown that the side of the triangular element lying along this type of boundary will automatically adopt the condition of $\hat{B}_z = 0$ if the nodes are treated as unknown potentials.

3.4.4 Screens

Since the screen is assumed to be infinitely conducting, the flux will flow parallel to the screen surface. The normal flux density is zero at this surface therefore.

$$- \frac{\partial U}{\partial n} = \hat{B}_n$$

$$= 0 \quad \text{(equivalent to an infinitely conducting surface)}$$

Flux penetration into a practical screen can be allowed for approximately by situating the sides of the triangle, representing the screen boundary, at a depth equivalent to $d/\sqrt{2}$, as suggested by Dreyfus[19] - see Fig. 3.10.

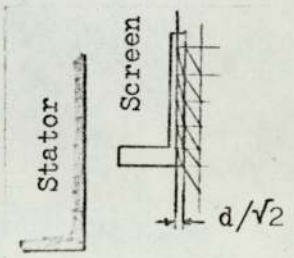

Fig. 3.10: Numerical treatment of screen

The structural components which are represented by the screen-type boundary within the end-region are those members with induced currents circulating in them. For the fundamental field the copper screen, clamping plate and the aluminium baffle-guides on the outer boundary can be approximated to by a screen surface. For the harmonic fields, most conducting surfaces within and enclosing the end-region are treated as screens.

3.4.5 Internal iron members

These are structural members within the end-region which can be treated as magnetic components with negligible eddy currents circulating within them.

(i) Infinitely permeable iron, $\mu = \infty$

The flux flows normally into this type of member, thus the tangential flux density is zero,

i.e. $-\frac{\partial U}{\partial t} = 0$

This condition is obtained within the finite-element solution by allowing all nodes on the surface to have the same scalar potential value.

(ii) Finite permeable iron, $\mu = \mu_0 \mu_r$

The correct density boundary conditions at the iron/air interface are given simply by specifying elements within this region and allocating the finite permeability to the elements.

3.4.6 End-rings

As the end-rings are normally non-magnetic, they only need consideration when investigating stator-produced harmonic fields. Magnetic end-rings would be represented by a region of finite permeability.

3.5 Conclusions

The numerical equations used to determine the scalar potential distribution in the end-region have been developed from the finite-element approach. Possible ways of dealing with the excitation and boundary conditions have been discussed.

From the numerical study of the end-region problem, a large number of simultaneous equations are formed; it is the aim of the following chapter to look into possible methods for solving these equations.

CHAPTER 4

SOLUTION OF LARGE SPARSE SYMMETRICAL MATRICES

4.1 General

The finite-element determination of the scalar potential in turbine-generator end-zones leads to a large set of simultaneous equations of the type given by Eqn. (3.10). In matrix form they may be written as:

$$\begin{bmatrix} a_{11} & a_{12} & & & \\ a_{21} & a_{22} & & & \\ a_{31} & & a_{3j} & & \\ \vdots & & \vdots & & \\ a_i & a_i & a_{ij} & a_{ii} & \\ & & & & a_{nn} \end{bmatrix} \cdot \begin{bmatrix} U_1 \\ U_2 \\ \\ \\ U_i \\ \\ U_n \end{bmatrix} = \begin{bmatrix} V_1 \\ \\ \\ \\ V_i \\ \\ V_n \end{bmatrix} \qquad \ldots\ldots\ldots (4.1)$$

Coefficient array — Unknowns — Source array

The coefficient terms, a_{ij}, are determined from the algebraic expressions associated with the unknown terms, U, in Eqn. (3.10), and the source term coefficients, V_i, are formed from the excitation and boundary conditions of the end-region.

The coefficient matrix is symmetric about the leading diagonal, and as the numerical formulation produces relatively few non-zero coefficients, the matrix is said to be sparse.

The following sections briefly discuss possible methods of solving large sparse symmetric matrices, and describe the method selected for the present study.

4.2 Types of Matrix Solution

4.2.1 Iterative methods

Iterative methods, of which Gauss-Seidel iteration, successive over-relaxation and line iteration are examples, have been used extensively for solving large sparse matrices. They have the advantage that only the non-zero coefficients have to be stored, so that large matrices can be solved on a relatively small computer. However, the disadvantages are that the number of iterations required for a reasonably accurate solution is dependent on the method of iteration chosen, the initial starting values, and the convergence characteristics of the equations.

4.2.2 Direct methods

Two methods for solving the matrix equation, (4.1), are:

(i) Transforming the matrix equation, such that $[A] \cdot x = [B]$ becomes $x = [B] \cdot [A]^{-1}$.

(ii) Eliminating the unknown values, x, until all the coefficients below the leading diagonal are zero: the values, x, are then determined by back-substituting. A method using this approach is the Gaussian elimination scheme.

Both approaches are suitable for solution by a large fast digital computer, but the inversion process of Method (i) tends to give a longer computer time because more arithmetic operations are needed.

4.2.3 Selection of method

Although iterative methods are more economical in computer storage, the direct approach overcomes the uncertainty of convergence. Past experience has shown that the direct method developed by Jennings[20], which is a modified version of the Gaussian elimination, is an efficient and economical method for solving large sparse symmetrical matrices of up to 3,000 unknowns,

provided the computer storage is available. The number of nodes that are required for an end-zone study is unlikely to exceed 1,000. For the solution of more than 3,000 unknowns, the iterative solution is far superior.

To show the advantages of this method, known as the "Compact Storage Scheme", it is compared with the Gaussian Elimination Method.

4.3 Gaussian Elimination Method

Let:

$$a_{11}x_1 + a_{12}x_2 + a_{13}x_3 + \ldots + a_{1m}x_m + \ldots + a_{1n}x_n = y_1 \quad \ldots (4.2)$$

$$a_{21}x_1 + a_{22}x_2 + a_{23}x_3 + \ldots + a_{2m}x_m + \ldots + a_{2n}x_n = y_2 \quad \ldots (4.3)$$

$$\vdots \qquad \vdots \qquad \vdots \qquad \vdots \qquad \vdots \qquad \vdots$$

(A)
$$a_{m1}x_1 + a_{m2}x_2 + a_{m3}x_3 + \ldots + a_{mm}x_m + \ldots + a_{mn}x_n = y_m \quad \ldots (4.4)$$

$$\vdots \qquad \vdots \qquad \vdots \qquad \vdots \qquad \vdots \qquad \vdots$$

$$a_{n1}x_1 + a_{n2}x_2 + a_{n3}x_3 + \ldots + a_{nm}x_m + \ldots + a_{nn}x_n = y_n \quad \ldots (4.5)$$

be a system of 'n' linear equations, where:

a_{11}, a_{12}, a_{13}, etc. are the coefficient terms

x_1, x_2, x_3, etc. are the unknown terms

y_1, y_2, y_3, etc. are the source terms

The process starts by eliminating x_1 from all equations but (4.2); then x_2 from all but (4.2) and (4.3), and so on, until only x_n is left.

To eliminate x_1 from Eqn. (4.3), it is necessary to add Eqn. (4.3) to Eqn. (4.2) multiplied by $(-a_{21}/a_{11})$, or, in general terms, add the m^{th} equation to Eqn. (4.2) multiplied by $(-a_{m1}/a_{11})$, where $m = 2 \rightarrow n$.

Thus the equations of System (A) are reduced to System (B):

$$a_{11}x_1 + a_{12}x_2 + a_{13}x_3 + \ldots + a_{1m}x_m + \ldots + a_{1n}x_n = y_1$$

$$a_{22}^{(1)}x_2 + a_{23}^{(1)}x_3 + \ldots + a_{2m}^{(1)}x_m + \ldots + a_{2n}^{(1)}x_n = y_2^{(1)} \quad \ldots (4.6)$$

$$\vdots \qquad \vdots \qquad \vdots \qquad \vdots \qquad \vdots$$

(B)
$$a_{m2}^{(1)}x_2 + a_{m3}^{(1)}x_3 + \ldots + a_{mm}^{(1)}x_m + \ldots + a_{mn}^{(1)}x_n = y_m^{(1)} \quad \ldots (4.7)$$

$$\vdots \qquad \vdots \qquad \vdots \qquad \vdots \qquad \vdots$$

$$a_{n2}^{(1)}x_2 + a_{n3}^{(1)}x_3 + \ldots + a_{nm}^{(1)}x_m + \ldots + a_{nn}^{(1)}x_n = y_n^{(1)} \quad \ldots (4.8)$$

where: $a_{ij}^{(1)} = a_{ij} - \frac{a_{i1}}{a_{11}} a_{1j}$

$y_i^{(1)} = y_i - \frac{a_{i1}}{a_{11}} y_1 \qquad (i, j = 2, 3, \ldots n)$

Similarly, to eliminate x_2, the equations below (4.6) are added, in turn, to (4.6) multiplied by $(- a_{m2}^{(1)}/a_{22}^{(1)})$, where $m = 3, \ldots n)$. The equations reduce to System (C):

$$
\begin{aligned}
a_{11}x_1 + a_{12}x_2 + a_{13}x_3 + \ldots + a_{1m}x_m + \ldots + a_{1n}x_n &= y_1 \\
a_{22}^{(1)}x_2 + a_{23}^{(1)}x_3 + \ldots + a_{2m}^{(1)}x_m + \ldots + a_{2n}^{(1)}x_n &= y_2^{(1)} \\
a_{33}^{(2)}x_3 + \ldots + a_{3m}^{(2)}x_m + \ldots + a_{3n}^{(2)}x_n &= y_3^{(2)} \\
\vdots \qquad\qquad \vdots \qquad\qquad & \vdots \\
a_{m3}^{(2)}x_3 + \ldots + a_{mm}^{(2)}x_m + \ldots + a_{mn}^{(2)}x_n &= y_n^{(2)} \\
\vdots \qquad\qquad \vdots \qquad\qquad & \vdots \\
a_{n3}^{(2)}x_3 + \ldots + a_{nm}^{(2)}x_m + \ldots + a_{nn}^{(2)}x_n &= y_n^{(2)}
\end{aligned}
\qquad (C)
$$

where: $a_{ij}^{(2)} = a_{ij}^{(1)} - \frac{a_{i2}^{(1)}}{a_{22}^{(1)}} a_{2j}^{(1)}$

$y_i^{(2)} = y_i^{(1)} - \frac{a_{i2}^{(1)}}{a_{22}^{(1)}} y_2^{(1)} \qquad (i, j = 3, 4, \ldots n)$

This procedure is repeated until the upper triangular matrix is formed as:

$$
\begin{aligned}
a_{11}x_1 + a_{12}x_2 + a_{13}x_3 + \ldots + a_{1m}x_m + \ldots + a_{1n}x_n &= y_1 \\
a_{22}^{(1)}x_2 + a_{23}^{(1)}x_3 + \ldots + a_{2m}^{(1)}x_m + \ldots + a_{2n}^{(1)}x_n &= y_2^{(1)} \\
a_{33}^{(2)}x_3 + \ldots + a_{3m}^{(2)}x_m + \ldots + a_{3n}^{(2)}x_n &= y_3^{(2)} \\
\vdots \qquad\qquad \vdots \qquad\qquad & \vdots \\
a_{mm}^{(m-1)}x_m + \ldots + a_{mn}^{(m-1)}x_n &= y_m^{(m-1)} \\
\vdots \qquad\qquad \vdots \qquad\qquad & \vdots \\
a_{nn}^{(n-1)}x_n &= y_n^{(n-1)}
\end{aligned}
$$

This gives:

$$x_n = \frac{y_n^{(n-1)}}{a_{nn}^{(n-1)}}$$

and x_{n-1} to x_1 can be obtained by back substitution,

i.e. $$x_{n-1} = \frac{y_{n-1}^{(n-2)} - a_{n-1,n}^{(n-2)} \cdot x_n}{a_{n-1,n-1}^{(n-2)}}$$

This is repeated until x_1 is determined.

Although this method is suitable for solution by computer, it does not make the best use of storage and symmetry.

4.4 Compact Storage Scheme

4.4.1 Storage

This method makes use of the fact that the coefficients formed by a finite-element solution give a symmetrically diagonal matrix, so only half the coefficients are considered. Of these, only the coefficients after and including the first non-zero, up to the leading diagonal, are stored.

In the following example of a coefficient array, Fig. 4.1, the coefficients are stored as 2, 1, 1, 0, 3, 1, 4, 2, 0, 0, 2. The correct addressing sequence of the coefficients is retained by forming a one-dimensional array, whose values specify the position of the first non-zero coefficient numbered from the diagonal; this is termed the "bandwidth matrix", and for Fig. 4.1 can be written as:

2	0	1	0	0
0	1	0	0	2
1	0	3	1	0
0	0	1	4	0
0	2	0	0	2

Fig. 4.1

1	1	3	2	4

The positions of the leading diagonal coefficients in the coefficient array are given by summing the bandwidths, i.e.:

Bandwidth matrix: 1, 1, 3, 2, 4

Running sum: 1, 2, 5, 7, 11 (coefficient position in coefficient array)

Coefficients of the leading diagonals: 2, 1, 3, 4, 2

4.4.2 Reduction process

The process is best explained by the reduction of the following set of four simultaneous equations:-

$$\begin{bmatrix} a_{11} & a_{12} & a_{13} & a_{14} \\ a_{21} & a_{22} & a_{23} & a_{24} \\ a_{31} & a_{32} & a_{33} & a_{34} \\ a_{41} & a_{42} & a_{43} & a_{44} \end{bmatrix} \cdot \begin{bmatrix} x_1 \\ x_2 \\ x_3 \\ x_4 \end{bmatrix} = \begin{bmatrix} b_1 \\ b_2 \\ b_3 \\ b_4 \end{bmatrix}$$

The coefficient array is:

a_{11}	a_{21}	a_{22}	a_{31}	a_{32}	a_{33}	a_{41}	a_{42}	a_{43}	a_{44}

R.H.S.

b_1	b_2	b_3	b_4

In the reduction process, a double asterisk, **, indicates a reduced coefficient, and a single asterisk, *, indicates a coefficient held in temporary computer storage.

4.4.2.1 Reduction of the 1st row

The leading diagonal is reduced to unity by dividing the first row by a_{11}, giving:

$$1 \quad a_{12}^{**} \quad a_{13}^{**} \quad a_{14}^{**} \qquad b_1^{**}$$

$$a_{21} \quad a_{22} \quad a_{23} \quad a_{24} \qquad b_2$$

where: $a_{12}^{**} = \frac{a_{12}}{a_{11}}$, etc. are the reduced coefficients.

These double asterisk values cannot be stored until other rows are reduced, but the value $1/a_{11}$ over-writes the leading diagonal value, a_{11}. The coefficient array and R.H.S. becomes:

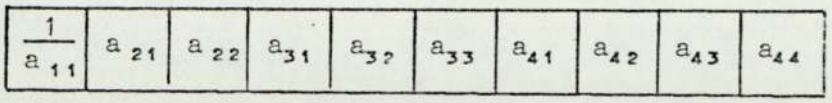

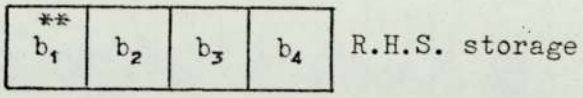

4.4.2.2 Reduction of 2nd row

$$a_{21}^{*} = a_{21}$$

a_{21}^{*} is held in a temporary store

This now releases the storage location filled by a_{21}, so the reduced coefficient $a_{12}^{**} = a_{12}/a_{11}$, which, by symmetry, becomes a_{21}^{*}/a_{11}, and over-writes the a_{21} location. In eliminating the x_1, the following occur:-

$$a_{22}^{*} = a_{22} - a_{12}^{**} a_{21}^{*}$$

$$a_{23}^{*} = a_{23} - a_{13}^{**} a_{21}^{*}$$

$$a_{24}^{*} = a_{24} - a_{14}^{**} a_{21}^{*}$$

$$b_2^{*} = b_2 - b_1^{**} a_{21}^{*}$$

The leading diagonal, a_{22}^{*}, is reduced to 1 by dividing by a_{22}^{*}, and the value $1/a_{22}^{*}$ over-writes a_{22}.

The reduced coefficients become

$$a_{23}^{**} = \frac{a_{23}^{*}}{a_{22}^{*}}, \quad a_{24}^{**} = \frac{a_{24}^{*}}{a_{22}^{*}}, \quad b_2^{**} = \frac{b_2^{*}}{a_{22}^{*}}$$

Again the values a_{23}^{**}, a_{24}^{**} cannot be calculated until Rows 3 and 4 are reduced: the arrays are now as follows:-

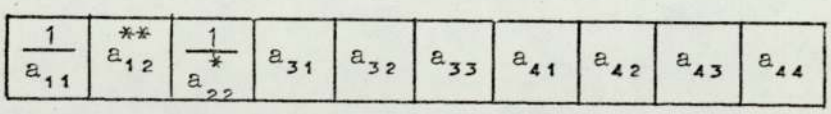

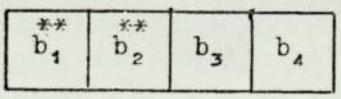

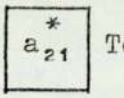

4.4.2.3 Reduction of 3rd row

To eliminate x_1 and x_2 from the 3rd row, the procedure is as follows:-

$$a^{*}_{31} = a_{31}$$

This over-writes a^{*}_{21} in the temporary store, and $a^{**}_{13} = a^{*}_{31}/a_{11}$ over-writes a_{31} in the main store.

$$a^{*}_{32} = a_{32} - a^{*}_{31}\, a^{**}_{12}$$

and is stored in the temporary store.

This releases the store held by a_{32}, and, because of symmetry, $a^{**}_{23} = a^{*}_{32}/a^{*}_{22}$. Thus a^{**}_{23} over-writes a_{32} in the main store: the other values are:

$$a^{*}_{33} = a_{33} - a^{*}_{31}\, a^{**}_{13} - a^{*}_{32}\, a^{**}_{23}$$

$$a^{*}_{34} = a_{31} - a^{*}_{31}\, a^{**}_{14} - a^{*}_{32}\, a^{**}_{24}$$

$$b^{*}_{3} = b_3 - a^{*}_{31}\, b^{**}_{1} - a^{*}_{32}\, b^{**}_{2}$$

The diagonal a^{*}_{33} is reduced to 1 by dividing throughout by a^{*}_{33}, and the value $1/a^{*}_{33}$ over-writes a_{33}. The reduced values are $a^{**}_{34} = a^{*}_{34}/a^{*}_{33}$, and $b^{**}_{3} = b^{*}_{3}/a^{*}_{33}$. The a^{**}_{34} cannot be calculated until the fourth equation has been reduced.

The state of the arrays after the third reduction is:

$\frac{1}{a_{11}}$	a^{**}_{12}	$\frac{1}{a^{*}_{22}}$	a^{**}_{13}	a^{**}_{23}	$\frac{1}{a^{*}_{33}}$	a_{41}	a_{42}	a_{43}	a_{44}	Main store

b^{**}_{1}	b^{**}_{2}	b^{**}_{3}	b_4	R.H.S. store

a^{*}_{31}	a^{*}_{32}	Temporary store

4.4.2.4 Reduction of 4th row

As before, in eliminating x_1, x_2 and x_3 the procedure is:

$a^{*}_{41} = a_{41}$ and over-writes a^{*}_{31}

$a^{**}_{14} = \dfrac{a^{*}_{41}}{a_{11}}$ and over-writes a_{41}

$a^{*}_{42} = a_{42} - a^{*}_{41}\, a^{**}_{12}$ and over-writes a^{*}_{32},

thus $a^{**}_{24} = \dfrac{a^{*}_{42}}{a^{*}_{22}}$ can now be stored in the a_{42} location

$a^{*}_{43} = a_{43} - a^{*}_{41}\, a^{**}_{13} - a^{*}_{42}\, a^{**}_{23}$ and stored in the temporary store

thus $a^{**}_{34} = \dfrac{a^{*}_{43}}{a^{*}_{33}}$ can be stored in the a_{43} location

$a^{*}_{44} = a_{44} - a^{*}_{41}\, a^{**}_{14} - a^{*}_{42}\, a^{**}_{24} - a^{*}_{43}\, a^{**}_{34}$

The value $1/a^{*}_{44}$ is stored in a_{44} location.

$b^{*}_{4} = b_4 - a^{*}_{41}\, b^{**}_{1} - a^{*}_{42}\, b^{**}_{2} - a^{*}_{43}\, b^{**}_{3}$

$b^{**}_{4} = \dfrac{b^{*}_{4}}{a^{*}_{44}}$

Thus the storage is finally:

$\frac{1}{a_{11}}$	a^{**}_{12}	$\frac{1}{a^{*}_{22}}$	a^{**}_{13}	a^{**}_{23}	$\frac{1}{a^{*}_{33}}$	a^{**}_{14}	a^{**}_{24}	a^{**}_{34}	$\frac{1}{a^{*}_{44}}$

Main store

b^{**}_{1}	b^{**}_{2}	b^{**}_{3}	b^{**}_{4}

R.H.S. store

a^{*}_{41}	a^{*}_{42}	a^{*}_{43}

Temporary store

The final reduced matrix is:

$$\begin{vmatrix} 1 & a^{**}_{12} & a^{**}_{13} & a^{**}_{14} \\ & 1 & a^{**}_{23} & a^{**}_{24} \\ & & 1 & a^{**}_{34} \\ & & & 1 \end{vmatrix} \cdot \begin{vmatrix} x_1 \\ x_2 \\ x_3 \\ x_4 \end{vmatrix} = \begin{vmatrix} b^{**}_{1} \\ b^{**}_{2} \\ b^{**}_{3} \\ b^{**}_{4} \end{vmatrix}$$

To obtain x_1, x_2, x_3 and x_4, back-substitution is used, i.e.:

$$x_4 = b_4^{**}$$

$$x_3 = b_3^{**} - a_{34}^{**} x_4$$

etc.

4.4.3 Merits of the Compact Storage Method

Besides the advantage of storage as mentioned in Section 4.4.1, the reduction process of the coefficient array is more efficient than the Gaussian Elimination Method, since there is less "jumping" around within the main sequence store. This is shown in Fig. 4.2:

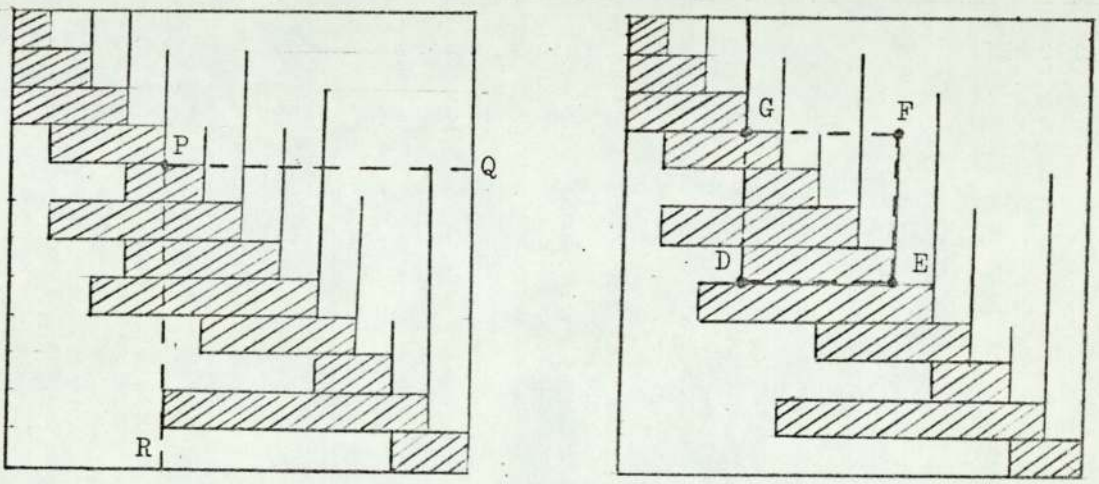

Fig. 4.2: Typical coefficient array of a sparse matrix

Fig. 4.2 shows diagrammatically the coefficient arrangement for a typical sparse matrix. Considering the Gaussian Elimination first, at some stage the coefficients of column PR will be eliminated by using the coefficients of row PQ. In order to discover which rows are affected, the address sequence for the whole of the latter part of the matrix will have to be inspected, and the appropriate rows operated on. However, in the Compact Storage Scheme the elimination of one row - DE (Fig. 4.2) - is performed by referring to the coefficients within the square DEFG.

4.5 Solution by the Compact Storage Scheme

The method is used to solve the following equations:-

$$2x + 2y + 0z + 2w = 14$$

$$2x + y + z + 0w = 7$$

$$0x + y + 2z + 0w = 8$$

$$2w + 0y + 0z + 3w = 14$$

The storage is as follows:-

2	2	1	1	2	2	0	0	3	Main store

14	7	8	14	R.H.S. store

After the reduction of the 1st row:

$$\begin{vmatrix} 1 & 1 & 0 & 1 \\ 2 & 1 & 1 & 0 \\ 0 & 1 & 2 & 0 \\ 2 & 0 & 0 & 3 \end{vmatrix} \cdot \begin{vmatrix} x \\ y \\ z \\ w \end{vmatrix} = \begin{vmatrix} 7 \\ 7 \\ 8 \\ 14 \end{vmatrix}$$

$\frac{1}{2}$	2	1	1	2	2	0	0	3	Main store

7	7	8	14	R.H.S. store

After the 2nd row reduction:

$$\begin{vmatrix} 1 & 1 & 0 & 1 \\ & 1 & -1 & 2 \\ 0 & 1 & 2 & 0 \\ 2 & 0 & 0 & 3 \end{vmatrix} \cdot \begin{vmatrix} x \\ y \\ z \\ w \end{vmatrix} = \begin{vmatrix} 7 \\ 7 \\ 8 \\ 14 \end{vmatrix}$$

$\frac{1}{2}$	1	-1	1	2	2	0	0	3	Main store

7	7	8	14	R.H.S. store

2	Temporary store

After the 3rd row reduction:

$$\begin{vmatrix} 1 & 1 & 0 & 1 \\ & 1 & -1 & 2 \\ & & 1 & -\frac{2}{3} \\ 2 & 0 & 0 & 3 \end{vmatrix} \cdot \begin{vmatrix} x \\ y \\ z \\ w \end{vmatrix} = \begin{vmatrix} 7 \\ 7 \\ \frac{1}{3} \\ 14 \end{vmatrix}$$

$\frac{1}{2}$	1	-1	-1	$\frac{1}{3}$	2	0	0	3

Main store

7	7	$\frac{1}{3}$	14

R.H.S. store

1	

Temporary store

After the 4th row reduction:

$$\begin{vmatrix} 1 & 1 & 0 & 1 \\ & 1 & -1 & 2 \\ & & 1 & -\frac{2}{3} \\ & & & 1 \end{vmatrix} \cdot \begin{vmatrix} x \\ y \\ z \\ w \end{vmatrix} = \begin{vmatrix} 7 \\ 7 \\ \frac{1}{3} \\ 4 \end{vmatrix}$$

$\frac{1}{2}$	1	-1	-1	$\frac{1}{3}$	1	2	$-\frac{2}{3}$	$\frac{3}{11}$

Main store

7	7	$\frac{1}{3}$	4

R.H.S. store

2	-2	-2

Temporary store

The solution to the above reduced matrix is:

$x = 1, \quad y = 2, \quad z = 3, \quad w = 4.$

4.6 Conclusions

End-zone studies can adequately be represented by 1,000 nodes or less, and for this size of problem experience has shown that the Compact Storage Direct Method is simple and economical to use.

A computer program has been written, and all the end-region problems studied within this thesis have been solved using this method.

CHAPTER 5

VERIFICATION OF THE FINITE-ELEMENT METHOD

5.1 General

The finite-element approach has been formulated in numerical terms, but before solving a generator end-zone problem, it is desirable to demonstrate the working of the method, and to indicate its accuracy compared with an analytical approach. Two examples for which analytical solutions are obtainable will be considered, viz.:

(i) Scalar potential distribution in a rectangular sheet with a specified potential on one edge and zero potential on the other three.

(ii) Scalar potential distribution between two concentric cylinders, with a specified potential varying sinusoidally round the periphery on one, and zero potential on the other (applicable to the open-circuit condition in the air-gap of a machine).

5.2 Rectangular Plate

5.2.1 Finite-element solution

The problem is illustrated in Fig. 5.1, and is symmetric about the line 'AA'.

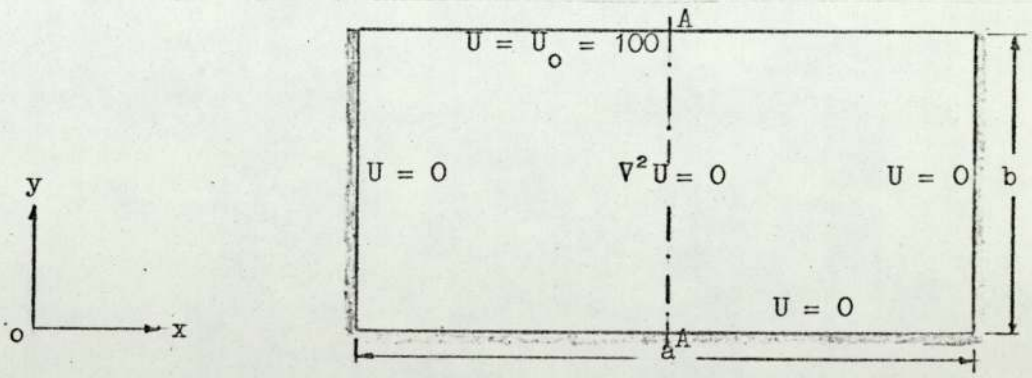

Fig. 5.1: Rectangular plate

The potential within the plate is described by Laplace's equation, which in cartesian co-ordinates is:

$$\frac{\partial^2 U}{\partial x^2} + \frac{\partial^2 U}{\partial y^2} = 0 \qquad \ldots\ldots\ldots (5.1)$$

The functional corresponding to Eqn. (5.1) is obtained by applying Euler's equation, as described in Section 8.3:

$$\text{i.e.} \quad \frac{\partial}{\partial x}\left[\frac{\partial f_x}{\partial\left\{\frac{\partial U}{\partial x}\right\}}\right] = \frac{\partial}{\partial x}\left\{\frac{\partial U}{\partial x}\right\}$$

$$\text{leads to} \int \partial f_x = \int \frac{\partial U}{\partial x}\,\partial\left\{\frac{\partial U}{\partial x}\right\}$$

$$f_x = \tfrac{1}{2}\left\{\frac{\partial U}{\partial x}\right\}^2$$

Similarly:

$$f_y = \tfrac{1}{2}\left\{\frac{\partial U}{\partial y}\right\}^2$$

giving the functional as:

$$X = \iint_S \tfrac{1}{2}\left[\left\{\frac{\partial U}{\partial x}\right\}^2 + \left\{\frac{\partial U}{\partial y}\right\}^2\right] dx,\, dy \qquad \ldots\ldots\ (5.2)$$

The functional is extremised by differentiating Eqn. (5.2) with respect to U, and equating to zero. This gives:

$$\frac{\partial X}{\partial U} = \iint_S \left[\left\{\frac{\partial U}{\partial x}\right\}\frac{\partial}{\partial U_i}\left\{\frac{\partial U}{\partial x}\right\} + \left\{\frac{\partial U}{\partial y}\right\}\frac{\partial}{\partial U}\left\{\frac{\partial U}{\partial y}\right\}\right] dx\, dy$$

$$= 0 \qquad \ldots\ldots\ (5.3)$$

To solve Eqn. (5.3) numerically, the rectangular plate is divided into triangular elements, as shown in Fig. 5.2, and the potential is assumed to vary linearly over each triangle. This can be written as:

$$U = \alpha_1 + \alpha_2 x + \alpha_3 y$$

which, expressing the coefficients α in terms of the nodal potentials and co-ordinates of the general triangle i, j, m, gives:

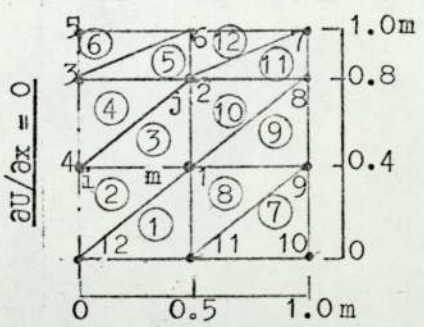

Fig. 5.2: Element sub-division

$$U = \frac{1}{2\Delta}\left\{(a_i + b_i x + c_i y)U_i + (a_j + b_j x + c_j y)U_j + (a_m + b_m x + c_m y)U_m\right\} \qquad \ldots\ldots\ (5.4)$$

where: $a_i = x_j y_m - x_m y_j$, $b_i = y_j - y_m$, $c_i = x_m - x_j$

$a_j = x_m y_i - x_i y_m$, $b_j = y_m - y_i$, $c_j = x_i - x_m$

$a_m = x_i y_j - x_j y_i$, $b_m = y_i - y_j$, $c_m = x_j - x_i$

In the numerical treatment, the functional is extremised with respect to potentials at all the nodes. Thus, for node 'i' of the general triangle (Fig. 5.2) extremisation is carried out by differentiating Eqn. (5.2) with respect to U_i, summing similar equations formed from all triangles connected with node 'i', and equating to zero; i.e.

$$\sum \frac{\partial X^e}{\partial U_i} = \sum \iint_s \left[\left\{ \frac{\partial U}{\partial x} \right\} \frac{\partial}{\partial U_i} \left\{ \frac{\partial U}{\partial x} \right\} + \left\{ \frac{\partial U}{\partial y} \right\} \frac{\partial}{\partial U_i} \left\{ \frac{\partial U}{\partial y} \right\} \right] dx\, dy$$

$$= 0 \qquad \ldots\ldots\ldots (5.5)$$

where $\sum$ represents the summation of all connected triangles.

Substituting for U from Eqn. (5.4) gives the final numerical equation as:

$$\sum \frac{\partial X^e}{\partial U_i} = \sum \frac{1}{4\Delta} \left\{ (b_i^2 + c_i^2) U_i + (b_i b_j + c_i c_j) U_j + (b_i b_m + c_i c_m) U_m \right\}$$

$$= 0 \qquad \ldots\ldots\ldots (5.6)$$

For the example in Fig. 5.2, the extremisation of the functional leads to the following equations:-

Node 1: $\frac{\partial X_1}{\partial U_1} + \frac{\partial X_2}{\partial U_1} + \frac{\partial X_3}{\partial U_1} + \frac{\partial X_8}{\partial U_1} + \frac{\partial X_9}{\partial U_1} + \frac{\partial X_{10}}{\partial U_1} = 0$ ..... (5.7)

Node 2: $\frac{\partial X_3}{\partial U_2} + \frac{\partial X_4}{\partial U_2} + \frac{\partial X_5}{\partial U_2} + \frac{\partial X_{10}}{\partial U_2} + \frac{\partial X_{11}}{\partial U_2} + \frac{\partial X_{12}}{\partial U_2} = 0$ ..... (5.8)

Node 3: $\frac{\partial X_4}{\partial U_3} + \frac{\partial X_5}{\partial U_3} + \frac{\partial X_6}{\partial U_3} = 0$ ..... (5.9)

Node 4: $\frac{\partial X_2}{\partial U_4} + \frac{\partial X_3}{\partial U_4} + \frac{\partial X_4}{\partial U_4} = 0$ ..... (5.10)

(Nodes 3 and 4 actually lie on the line of symmetry, where the boundary condition is $\partial U/\partial x = 0$, but, as discussed in Section 3.4.4, these can be treated as unknown values.)

Each component of Eqns. (5.7) - (5.10) is given by the general equation, (5.6), and from the dimensions of Fig. 5.2, they reduce to:

$$4.1U_1 - 1.25U_2 + 0.0U_3 - 0.8U_4 = 0$$

$$-1.25U_1 + 4.95U_2 - 0.6U_3 + 0.0U_4 = 250$$

$$0.0U_1 - 0.6U_2 + 2.475U_3 - 0.625U_4 = 125$$

$$-0.8U_1 + 0.0U_2 - 0.625U_3 + 2.05U_4 = 0$$

In matrix form these become:

$$\begin{bmatrix} 4.1 & -1.25 & 0 & -0.8 \\ -1.25 & 4.95 & -0.6 & 0 \\ 0 & -0.6 & 2.475 & -0.625 \\ -0.8 & 0 & -0.625 & 2.05 \end{bmatrix} \cdot \begin{bmatrix} U_1 \\ U_2 \\ U_3 \\ U_4 \end{bmatrix} = \begin{bmatrix} 0 \\ 250 \\ 125 \\ 0 \end{bmatrix} \quad \ldots\ldots\ldots (5.11)$$

(The coefficient matrix is symmetrical about the leading diagonal.)

Solving Eqn. (5.11) gives:

$U_1 = 27$

$U_2 = 69.5$

$U_3 = 75.6$

$U_4 = 31.4$

A computer program has been written to enable calculations to be made with finer mesh systems. Fig. 5.3 shows two degrees

of sub-division, one having 121 nodes, and the other 286. The latter has small elements concentrated in the area of rapidly changing potential.

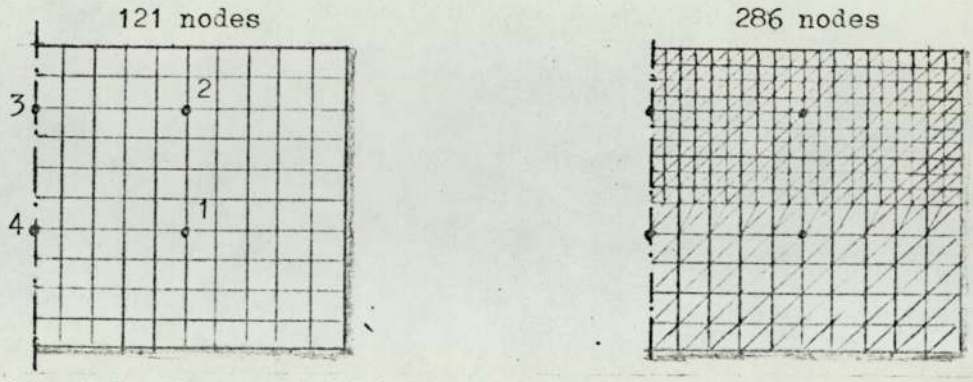

Fig. 5.3: Finer sub-divisions of the rectangular plate

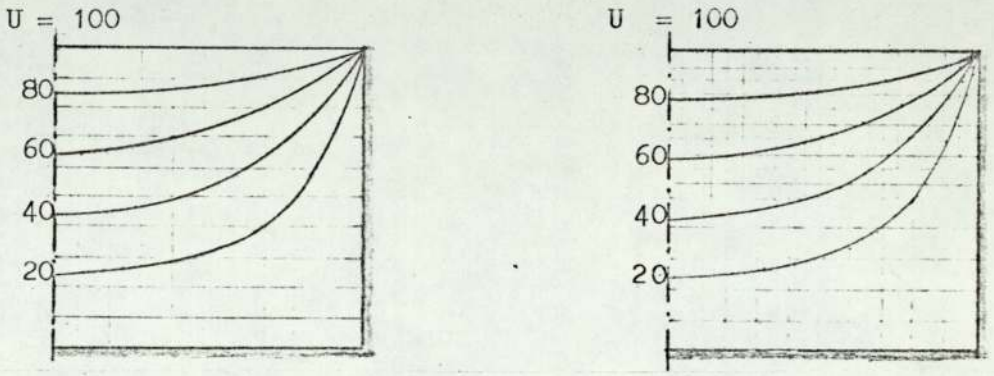

Fig. 5.4: Scalar potential distribution

The resulting scalar potential plots are given in Fig. 5.4.

5.2.2 Analytical solution

The problem to be solved is illustrated in Fig. 5.1.

The potential has a constant value of U_0 on the upper surface, but goes to zero at the vertical edges. This can be represented by a Fourier series of half-wavelength 'a' and odd harmonics only, since U is symmetrical about a/2.

$$\therefore \quad U = \sum_{n=1,3,5,..}^{\infty} \frac{4}{\pi} \frac{U_0}{n} \sin \frac{n\pi x}{a}$$

The potential within the plate is obtained by substituting

$$U = U'(y) \sin \frac{n\pi x}{a}$$

into Eqn. (5.1), giving:

$$\frac{\partial^2 U'}{\partial y^2} - \frac{n^2\pi^2}{a^2} U' = 0$$

for which the solution is:

$$U' = \sum_{n=1,3,5,\ldots}^{\infty} \left\{ A\, e^{\frac{n\pi}{a}y} + B\, e^{-\frac{n\pi}{a}y} \right\} \sin \frac{n\pi x}{a}$$

Constants A and B are determined from the following boundary conditions:-

At $y = 0$, $U' = 0$

$y = b$, $U' = U_o$

These give:

$$A = \frac{2U_o}{\sinh \frac{n\pi b}{a}} \quad \text{and} \quad B = -\frac{2U_o}{\sinh \frac{n\pi b}{a}}$$

The final equation is:

$$U = \sum_{n=1,3,5,\ldots}^{\infty} \frac{4U_o}{n\pi} \frac{\sinh \left\{ \frac{n\pi y}{a} \right\}}{\sinh \left\{ \frac{n\pi b}{a} \right\}} \sin \left\{ \frac{n\pi x}{a} \right\} \qquad \ldots\ldots\ldots (5.12)$$

Eqn. (5.12) was used to calculate the potential at nodes corresponding to those used in the finite-element studies. Results are compared in the following section.

5.2.3 Comparison

The potentials at the four nodes indicated in Fig. 5.2 are used to assess the accuracy of the numerical study.

Node No.	Analytic	Finite-element Study		
		Total number of nodes		
		12	121	287
1	27.7	27.0	27.78	27.74
2	70.4	69.5	70.2	70.3
3	76.6	75.6	76.57	76.6
4	34.8	31.4	34.77	34.78

Table 1

The results of the numerical and analytical methods agree well, even for the coarse mesh with only four internal nodes.

5.3 Concentric Cylinders

This problem corresponds to the situation in the air-gap of a turbine-generator if the following assumptions are made:-

(i) Slotting on stator and rotor surfaces is ignored.

(ii) The stator iron and rotor iron are infinitely permeable.

(iii) The stator and rotor are infinitely long.

(iv) The potential is sinusoidally distributed around the periphery, and has no axial variation.

(When comparing the numeric and analytic solutions, a peak scalar potential of 100 is assumed on the inner cylindrical surface, and zero on the outer surface. The radii used for the inner and outer cylinders are 0.573m and 0.7m respectively: values typical of a large turbine-generator.)

5.3.1 Finite-element solution

Using the quasi-3-dimensional approach, the peripheral variation of potential is built into the functional, and since there is no axial variation of potential, the problem reduces to the numerical solution of Laplace's equation in the region shown in Fig. 5.5. This region was divided into 36 triangular elements, and the equations derived in Section 3.3. were used to determine the potential distribution.

Variation of peak scalar potential across the gap between the cylinders is shown in Fig. 5.7.

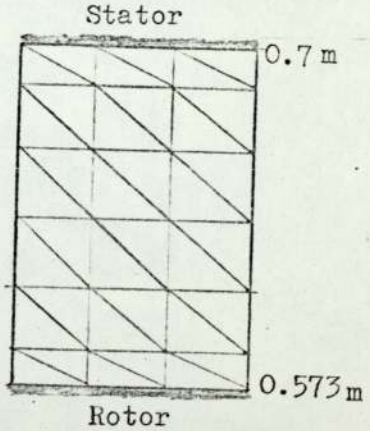

Fig. 5.5: Element division

5.3.2 Analytic solution

The assumptions of Section 5.3 reduce the analytic problem to the solution of Laplace's equation between two concentric cylinders, as shown in Fig. 5.6.

Laplace's equation in cylindrical co-ordinates is:

$$\frac{\partial^2 U}{\partial r^2} + \frac{1}{r}\frac{\partial U}{\partial r} + \frac{1}{r^2}\frac{\partial^2 U}{\partial \theta^2} = 0$$

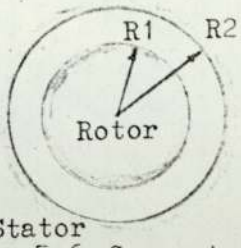

Fig. 5.6: Concentric cylinders

Using Assumption (iv) leads to:

$$\frac{\partial^2 U'}{\partial r^2} + \frac{1}{r}\frac{\partial U'}{\partial r} - \frac{p^2}{r^2} U' = 0 \qquad \ldots\ldots\ldots (5.13)$$

where: $U = U' \sin p\theta$

p = number of poles

The solution of Eqn. (5.13) is:

$$U = \sum_{n=1}^{p} (A r^n + B r^{-n}) \sin p\theta$$

The constants A and B are determined from the following boundary conditions:-

At $r = R_2$, $U = 0$

At $r = R_1$, $U = U_0 \sin p\theta$

giving the final solution as:

$$U = \frac{U_0 \left\{ r - \frac{R_2^2}{r} \right\} \sin p\theta}{\left\{ R_1 - \frac{R_2^2}{R_1} \right\}} \qquad \ldots\ldots\ldots (5.14)$$

Substituting for the values given in Section 5.3 gives the distribution of potential as shown in Fig. 5.7.

5.3.3 Comparison

Fig 5.7 compares the numeric and analytic values of potential across the gap, and shows very satisfactory agreement.

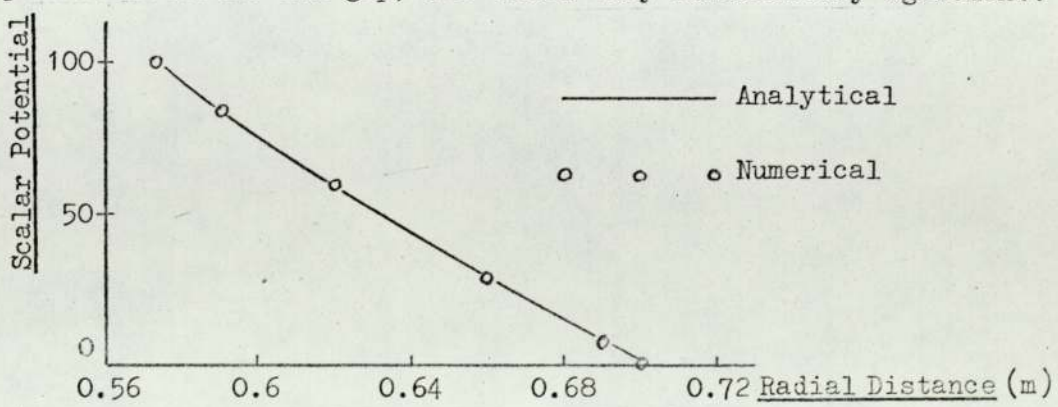

Fig. 5.7: Comparison of analytical and numerical potentials

5.4 Conclusions

The two relatively simple examples considered have demonstrated that the results obtained from the finite-element numerical approach give good agreement with the analytically-derived values. This encourages confidence in the method which, in the next chapter, will be applied to the calculation of end-zone fluxes in conventional and novel forms of generators.

CHAPTER 6

APPLICATION OF THE FINITE-ELEMENT METHOD TO MACHINE PROBLEMS

6.1 General

The earlier chapters have shown how the finite-element approach is formulated and applied to geometrically simple problems. The results were found to compare well with analytical values.

This chapter establishes the validity of the method for machine end-region problems by comparison of test and calculated results on the following machines:-

(i) A short-core replica of a 500 MW turbine-generator, where the flux density normal to the inner winding surface has been measured.

(ii) A 660 MW turbine-generator, where the flux density normal to the support fingers has been measured.

The method is also applied to open-circuit, short-circuit, and load conditions on a 660 MW turbine-generator, with particular attention being given to the calculation of the flux density normal to the stator-core surface. The effect of power factor variation on core-end-surface flux densities is shown.

Examples are also given of the determination of end-region flux distributions on the following machines:-

(a) A generator with a rotating superconducting field winding.

(b) A fully slotless turbine-generator.

6.2 Short-core Replica of a 500 MW Turbine-generator

6.2.1 Machine details

The radial dimensions were the same as for a production 500 MW generator, but the core length was only 0.3m and there was no rotor. One end-winding was conical, the other cylindrical: the arrangement of the replica is shown in Fig. 6.1.

The replica was tested, several years ago, to investigate the behaviour of the end-winding bracing under short-circuit

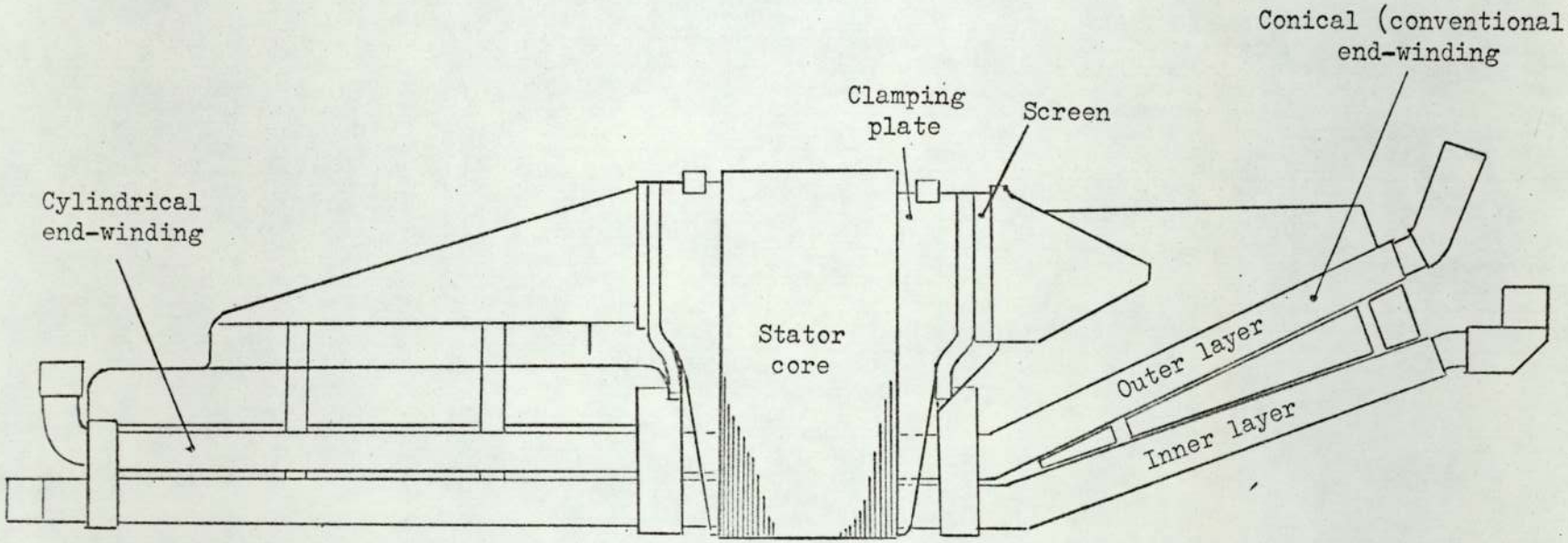

Fig. 6.1: Short-core replica of a 500 MW turbine-generator

conditions, but only a limited number of flux density values were obtained. Of these, the values measured normal to the inner surface of the end-winding conductors nearest the stator bore will be used for comparison purposes.

The measurements were made with the stator windings excited, as shown in Fig. 6.2: this gives a stationary pulsating field. The flux densities were measured with low stator currents, but, to indicate the levels arising in service, they were scaled up for the rated stator phase current of a production 500 MW generator. Fig. 6.3 shows the resulting flux density distribution:

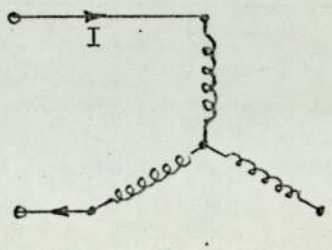

Fig. 6.2: Stator winding excitation used in tests

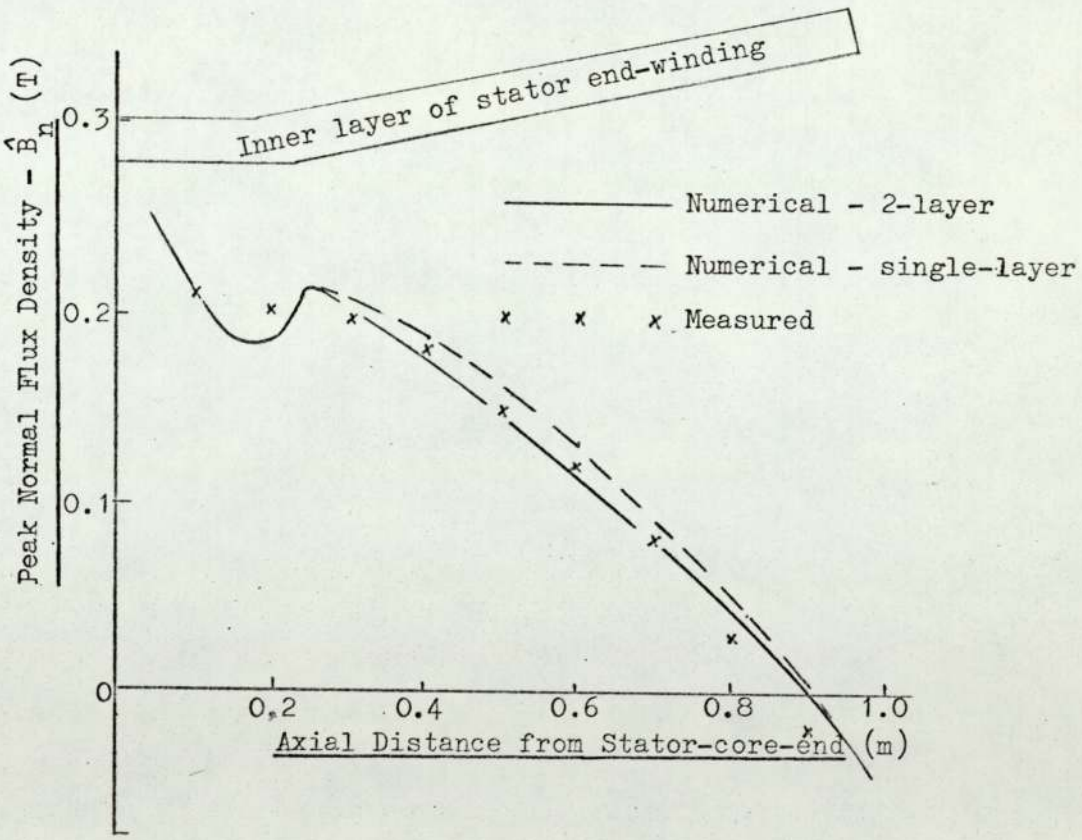

Fig. 6.3: Comparison of numerical with measured values of flux density normal to the inner surface of the end-winding cone

6.2.2 Finite-element solution

Before solving by the finite-element method, certain simplifying assumptions had to be made, viz.:

(i) The stator-core end-surface from the bore to the innermost part of the clamping-plate was considered as infinitely permeable ($\mu = \infty$).

(ii) Both clamping-plate and screen form part of the outer boundary, and were assumed to be infinitely conducting.

(iii) As the replica had no outer casing or end-cover to form natural boundaries for the numerical study, infinitely-permeable magnetic boundaries were assumed sufficiently far away for their influence in the vicinity of the stator winding to be small. (The axial outer boundary was situated at a distance equivalent to $2\frac{1}{2}$ times the end-winding length, and the radial outer boundary at a distance equivalent to twice the average end-winding radius.)

(iv) In the absence of a rotor, the centre-line of the machine was treated as an equipotential surface, i.e. $\mu = \infty$.

(v) The air-gap boundary line was set at the axial centre of the stator core where the axial flux density was zero, giving the boundary condition of $\partial U/\partial n = 0$.

(vi) The stator windings were represented by either

(a) a single current sheet situated between the two layers of the end-winding; or

(b) current sheets situated at the mid-depth of each end-winding layer.

With these approximations, the end-region reduces to the outlines as shown in Figs. 6.4 and 6.5:

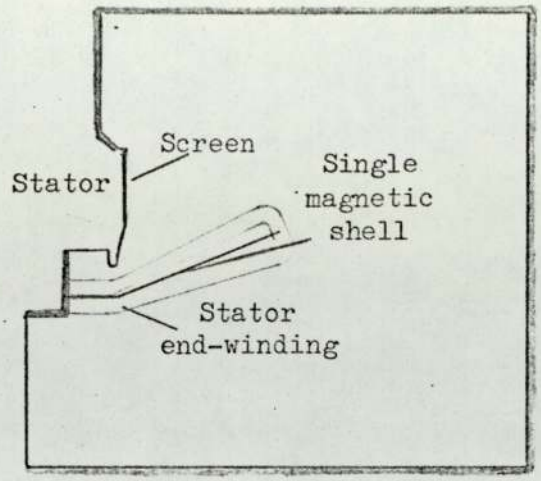

Fig. 6.4: Single-layer reprèsentation of end-winding

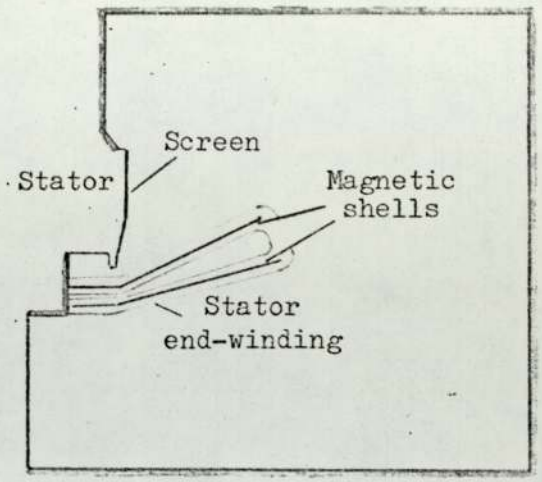

Fig. 6.5: 2-layer representation of end-winding

In each study the end-region was divided into 845 elements, and contained (with boundary points) 521 nodes. The element distribution is shown in Figs. 6.6 and 6.7, with concentration in the vicinity of the winding area so as to obtain accurate results for comparison with the measured values.

Solutions were obtained for a stator excitation equivalent to the rated stator current of the production machine. Flux densities normal to the inner surface of the stator winding were calculated from the scalar potential distribution, as shown in Fig. 6.8.

6.2.3 Comparison with measured values

Fig. 6.3 compares normal flux densities from the finite-element studies with the measured values. The agreement is good, with the 2-layer representation giving slightly better results.

6.3 660 MW Production Turbine-generator

Scalar potential distributions were calculated for the end-region of the production 660 MW turbine-generator of Fig. 1.2 for the following excitations:-

(i) Open-circuit - rotor only excited.

(ii) "Ideal" short-circuit - equal and opposite excitation on stator and rotor windings.

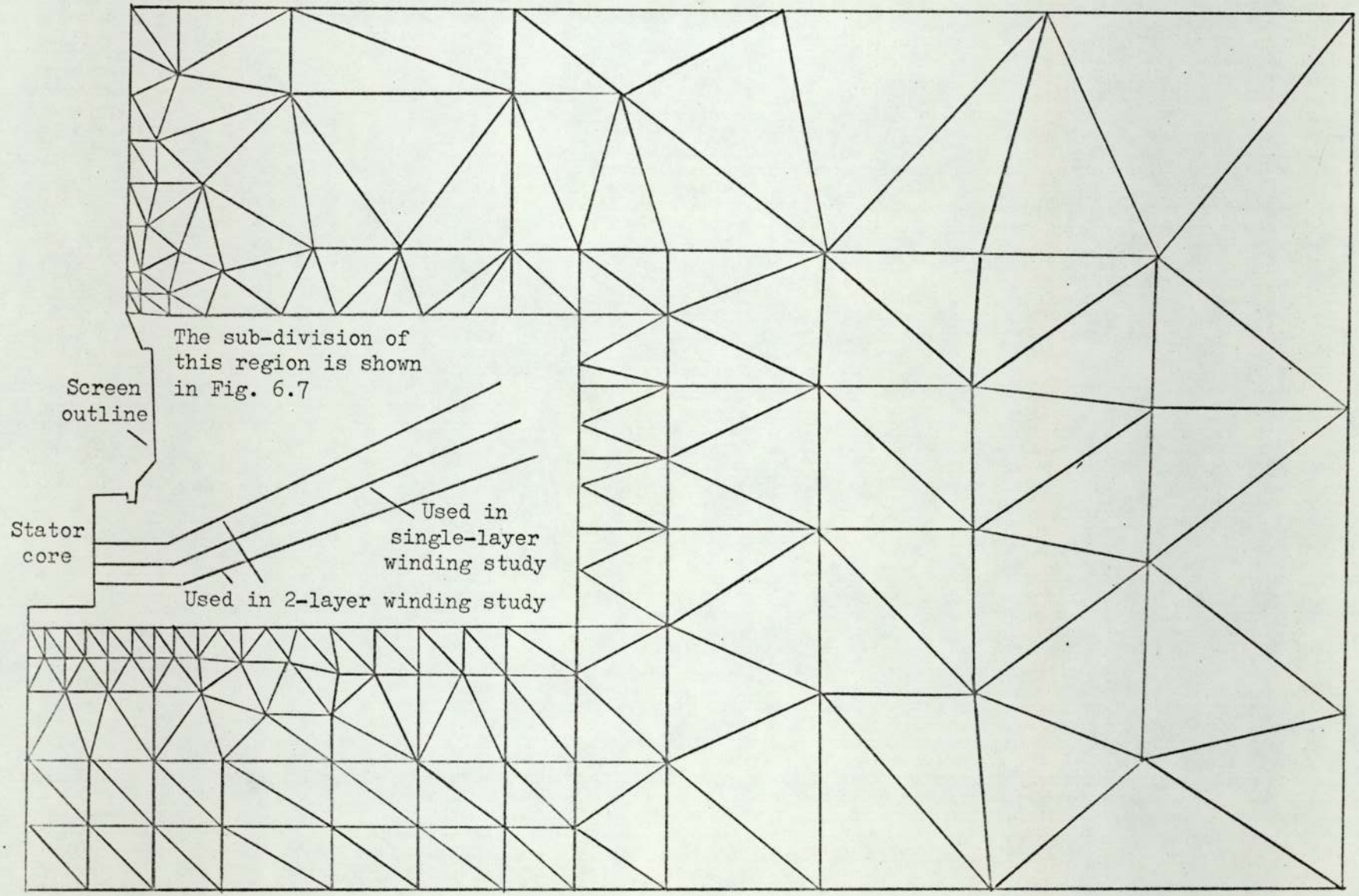

Fig. 6.6: Triangular element sub-division of the short-core replica end-region

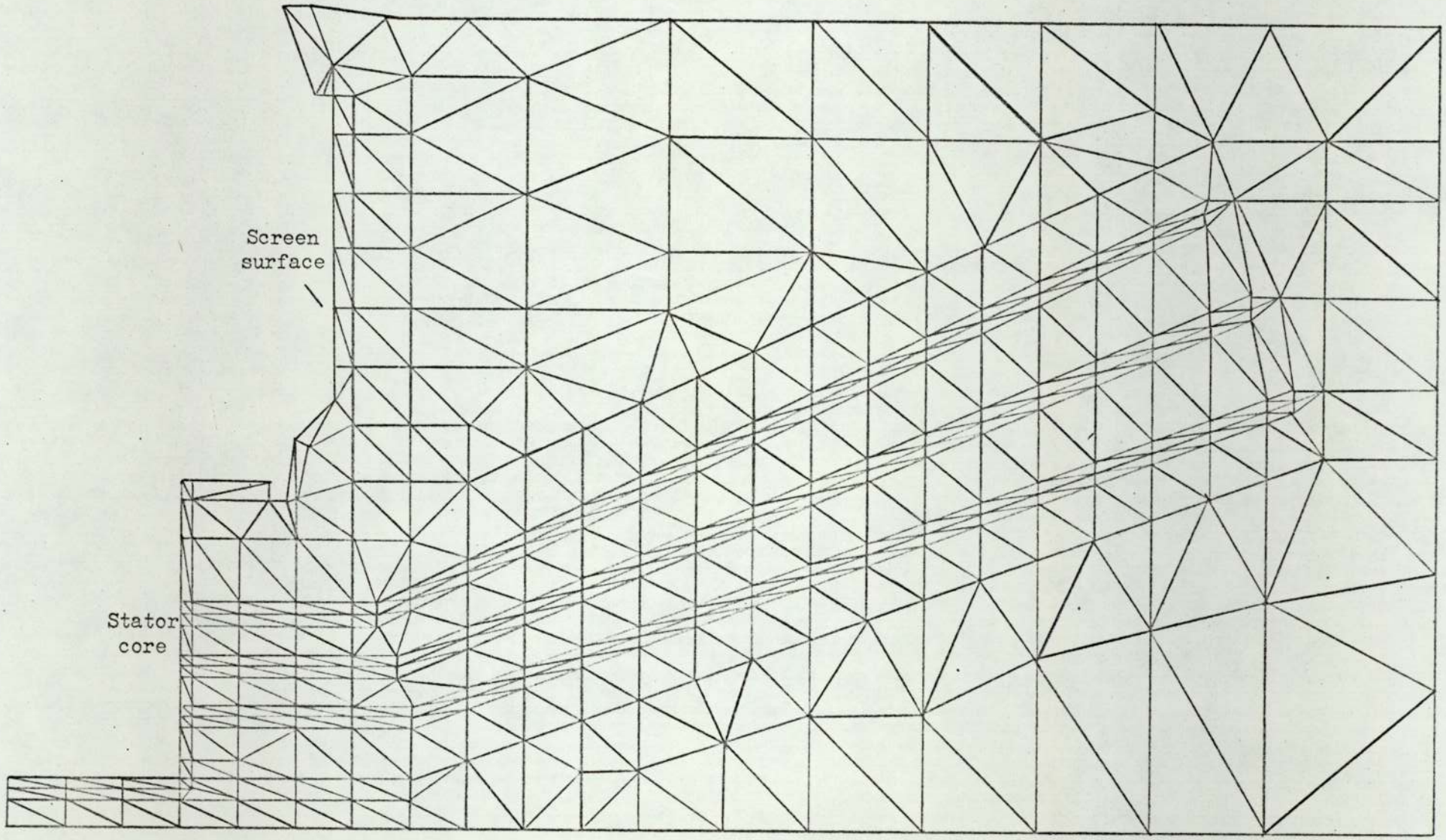

Fig. 6.7: Element sub-division of insert of Fig. 6.6

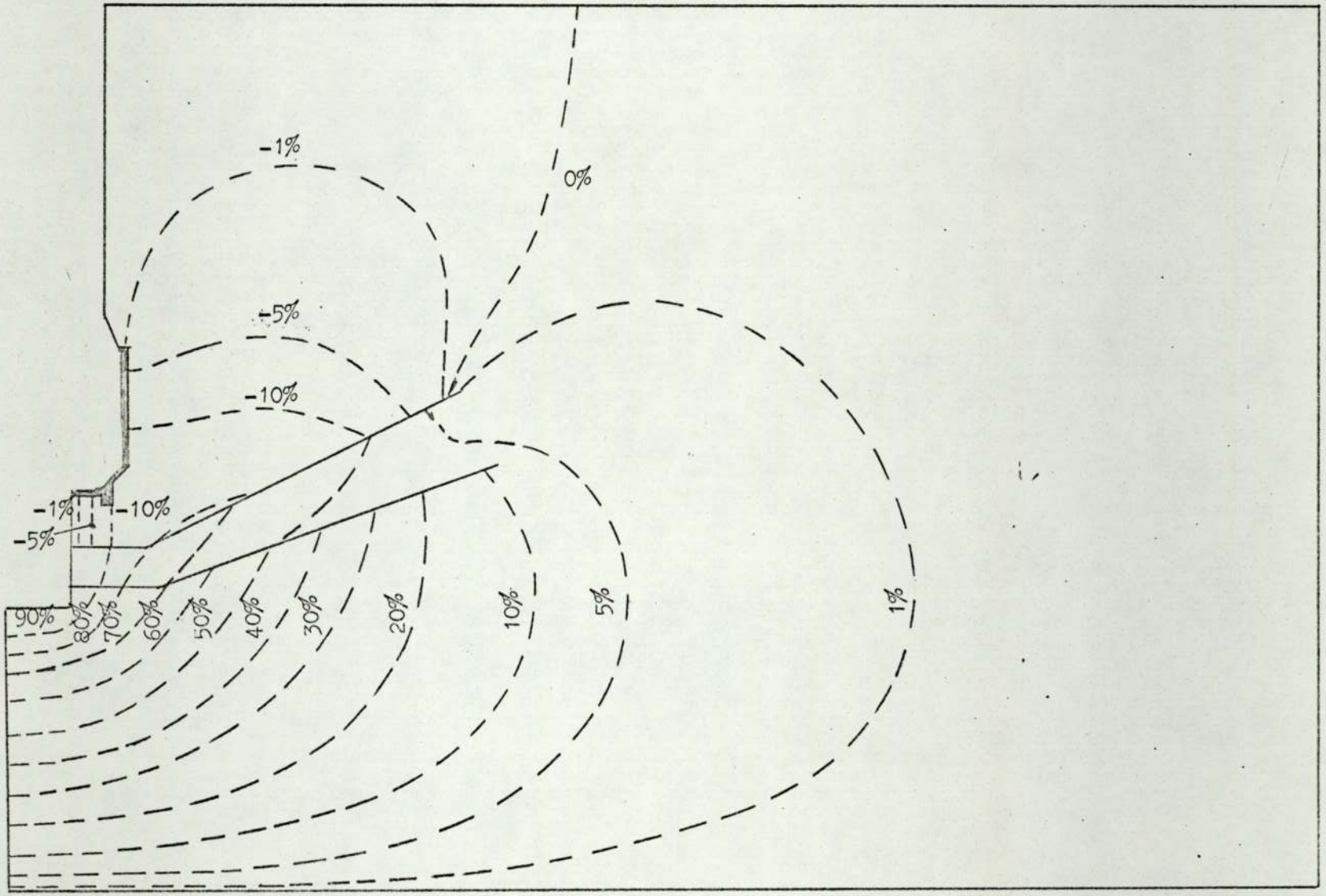

Fig. 6.8: Scalar potential distribution within the end-region of the short-core replica for the 2-layer winding study

(iii) Load - for a variation of power factors from 0.85 lag to 0.85 lead.

These studies gave:

(a) Open-circuit flux density normal to the support fingers for comparison with measured values.

(b) Flux densities normal to the stator-core end-surfaces for all excitation conditions.

(c) Comparison of open-circuit potential distributions of the quasi-3-dimensional study with a 2-dimensional finite-element study.

6.3.1 Open-circuit study

The open-circuit test is part of the Works test, and gives information on magnetisation, losses and temperature rises.

The following assumptions were required, in addition to those given in Section 2.3.5:-

(i) The outside boundary of the screen and clamping-plate were combined to form one large screen surface, and assumed to be infinitely conducting.

(ii) Eddy current and saturation effects in the stator core were ignored.

(iii) The end-ring cover was taken as a magnetic region, of $\mu_r = 500$.

(iv) The effect of rotor and stator slotting was allowed for by increasing the air-gap by Carter's coefficient, which was 1.086.

The potential difference, ΔU, between the magnetic shell representing the rotor winding current sheet is calculated in accordance with Eqn. (3.12). The peak ampere-turns of potential difference must be sufficient to give an air-gap flux density consistent with the open-circuit terminal voltage.

With these additional assumptions, the end-region is reduced to that of Fig. 6.9:

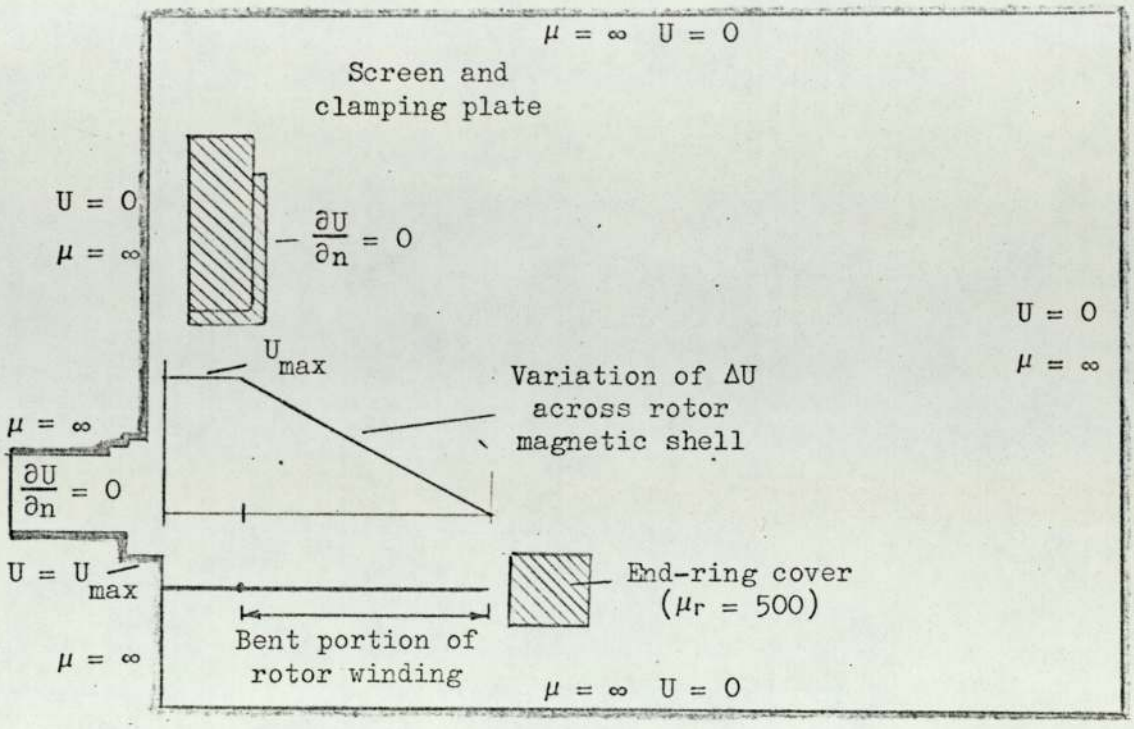

Fig. 6.9: Outline of the end-region of a 660 MW generator for solution purposes

The end-region was divided into 456 elements by 302 nodes, including the boundary nodes, as shown in Fig. 6.10.

The scalar potential distribution for this study is shown in Fig. 6.11, and the comparison of calculated with measured flux density normal to the support fingers is shown in Fig. 6.12:

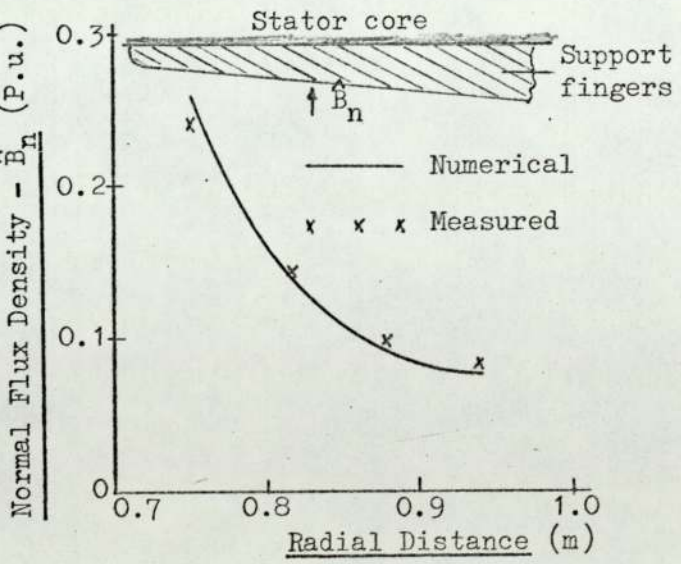

Note: In this and subsequent figures relating to the 660 MW generator flux densities are normalised, with rated voltage, open-circuit air-gap density as reference.

Fig. 6.12: Comparison of numerical with measured values of flux density normal to the support fingers

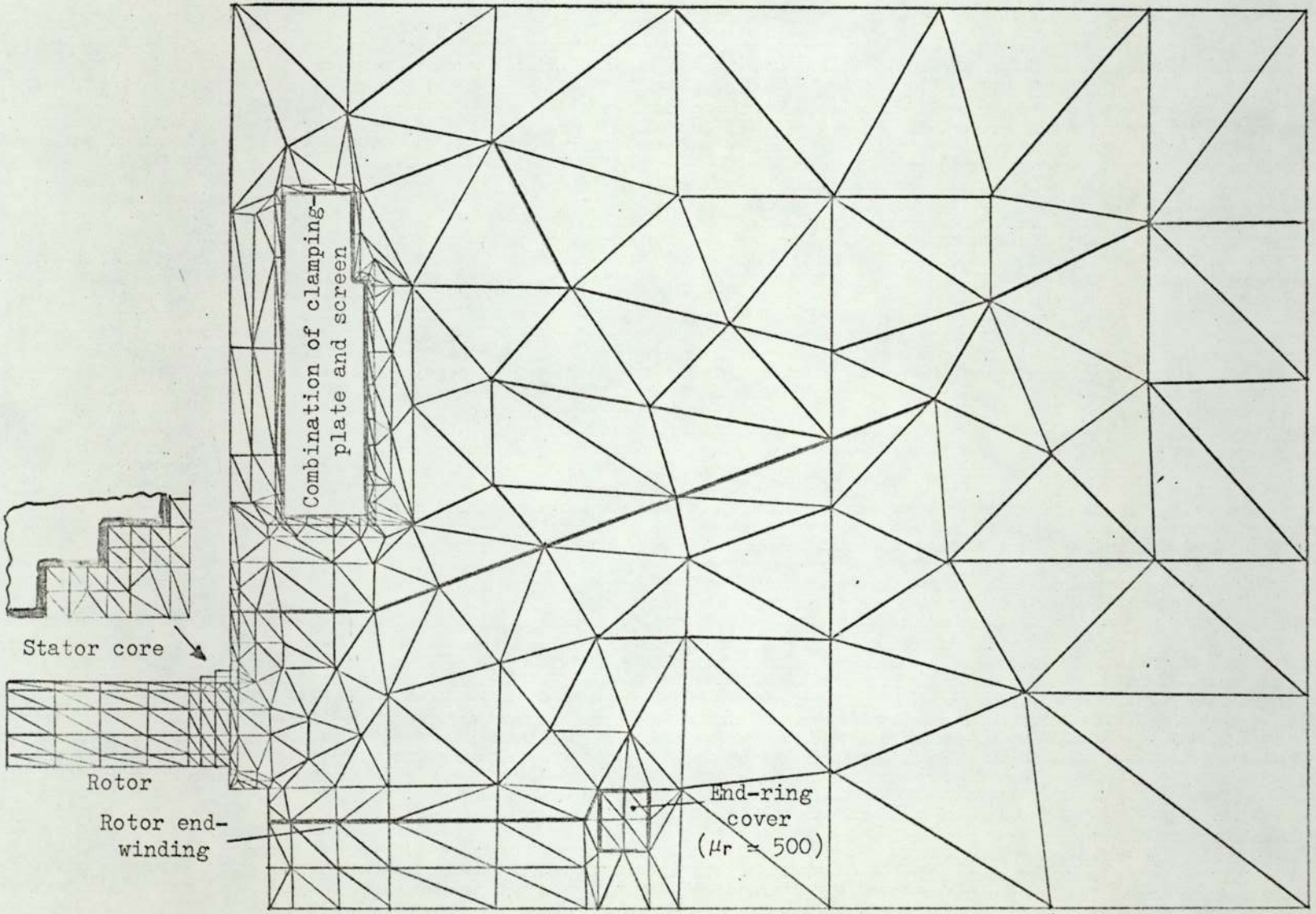

Fig. 6.10: Element sub-division of the end-region of a 660 MW turbine-generator

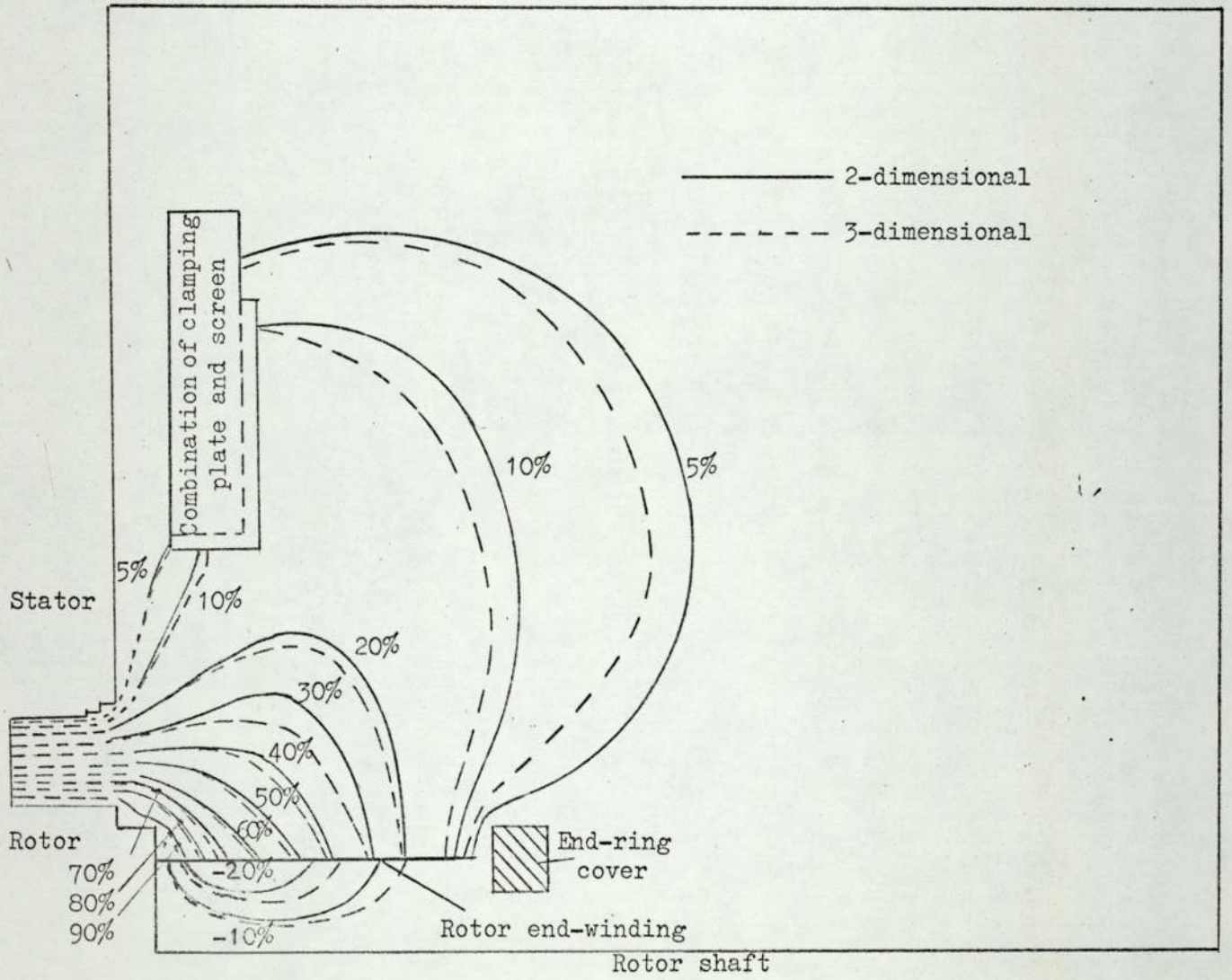

Fig. 6.11: Scalar potential distribution within the end-region of a 660 MW turbine-generator for open-circuit excitation

The core-end heating is dependent upon the magnitude and distribution of the axial flux density along the core end-surface: Fig. 6.13 shows this variation, together with the radial density variation along the stator bore:

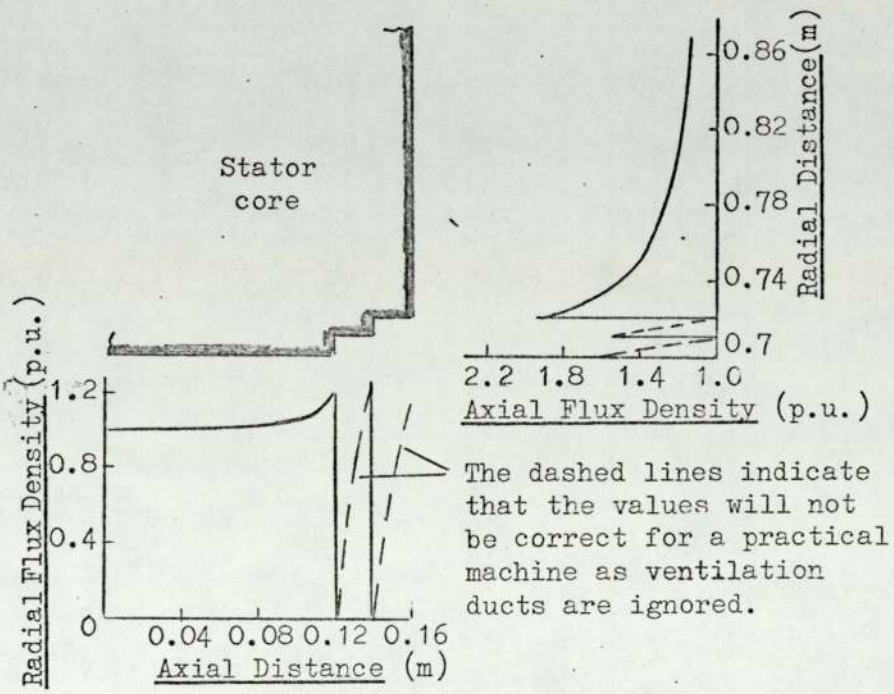

Fig. 6.13: Variation of open-circuit flux density normal to the stator-core end-surface

6.3.2 "Ideal" short-circuit excitation

This excitation requires the stator winding ampere-turns to be equal, but of opposite sign, to the rotor winding ampere-turns. This differs from the Works short-circuit test in that no allowance is made for the induced voltage needed to overcome the stator leakage reactance volts drop. All calculations for this excitation are done for rated stator winding current.

To solve numerically, using the finite-element method, the assumptions of Section 6.3.1 were adopted. The stator winding was represented by a single current sheet situated mid-way between the end-winding layers, and the potential difference distribution

simulating the effect of the winding current was given by Eqn. (3.11). Similarly, for the rotor winding, the potential difference distribution was given by Eqn. (3.12).

The element division was the same as for the open-circuit study, and the resulting potential distribution is given in Fig. 6.14.

6.3.3 Load study

The load flux densities within the end-region can be obtained for any power factor by adding vectorially the appropriately scaled values of flux density from the open-circuit and short-circuit studies. An example is given in Fig. 6.15 for a power factor of 0.85 lagging:

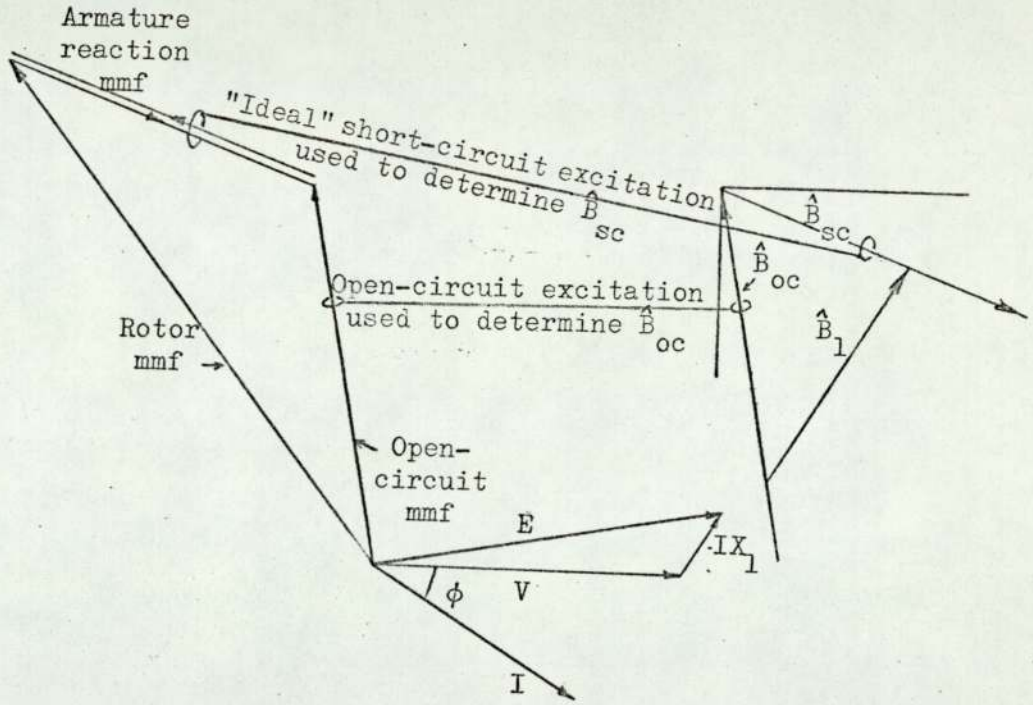

Fig. 6.15: Vector diagram for obtaining load flux densities

The calculated flux density normal to the stator-core end-surface is plotted in Fig. 6.16 for a range of power factors for a constant power output. These results show clearly the detrimental effect of leading power factor operation, since the axial fluxes increase, leading to higher stator core temperatures:

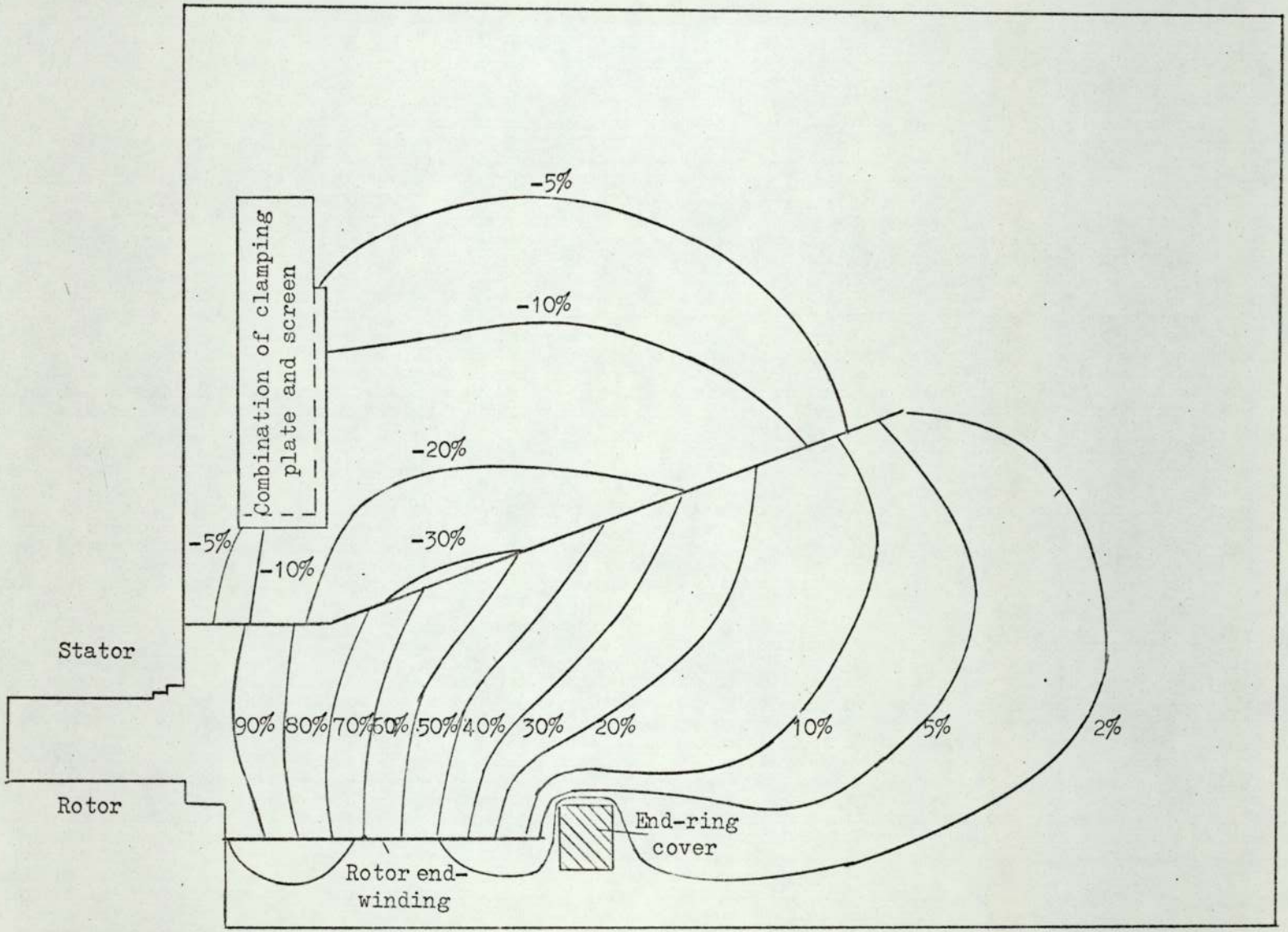

Fig. 6.14: Scalar potential distribution within the end-region of a 660 MW turbine-generator for "ideal" short-circuit excitation

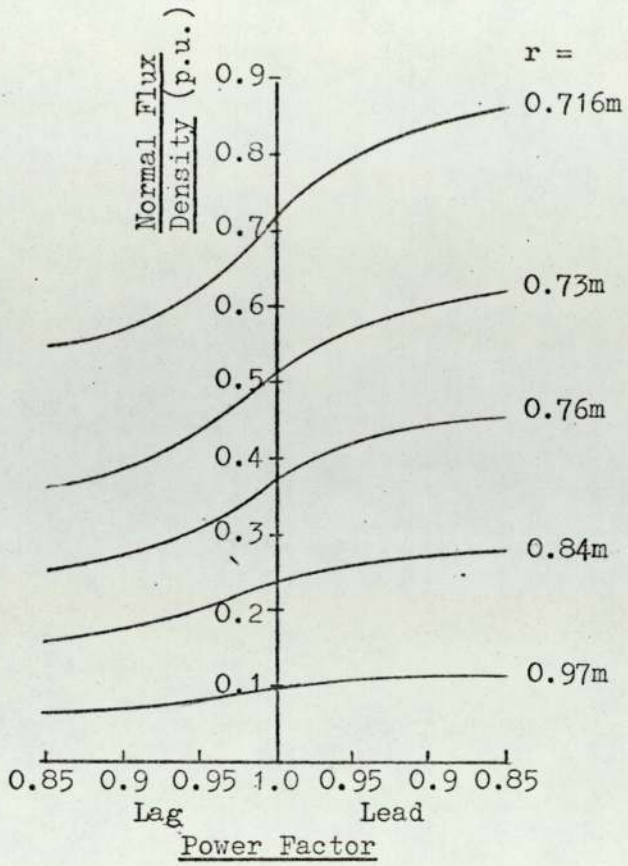

Fig. 6.16: Variation with power factor of flux density normal to the stator-core end-surface

6.3.4 Comparison of the quasi-3-dimensional approach with a 2-dimensional approach

The governing differential equation, (2.7), for the quasi-3-dimensional solution reduces to the axially symmetric case by substituting $p = 0$: this eliminates the peripheral term. This approximation is similar to that made in Teledeltos studies, where peripheral leakage is also ignored.

The open-circuit scalar potential distribution was calculated for the 2-dimensional approach and compared (see Fig. 6.11) with the quasi-3-dimensional potential distribution. The difference between the two distributions is small near the air-gap region, but increases towards the ends of the winding. This is because the peripheral leakage flux is dependent upon the ratio of peripheral flux path length to path length in the longitudinal plane. Thus, in the air-gap region, the peripheral distance is about 2.2m, compared to a "within-plane" distance of only 0.2m, which leads to small peripheral fluxes.

6.4 660 MW Generator with a Rotating Superconducting Field Winding

A design concept of considerable interest for very large unit ratings is the rotating superconducting field generator, where the conventional rotor is replaced by a superconducting winding mounted on an insulating core. Since there is no rotor iron, very high excitation ampere-turns are needed to provide the working density in a very much increased air-gap. (These can, of course, be provided with almost negligible loss.) The design of such a generator is described by Lorch[1].

Compared with the conventional generator, the higher field excitation and the increased air-gap tend to give much higher flux densities normal to the core end-surface. In an attempt to reduce these flux densities, the rotor end-winding was moved into the "air gap".

The open-circuit flux densities were calculated, using the finite-element method, for two rotor end-winding positions. Fig. 6.17 shows the boundary outline of the generator end-region, and the element division was such that both studies could be solved with a minimal change in data:

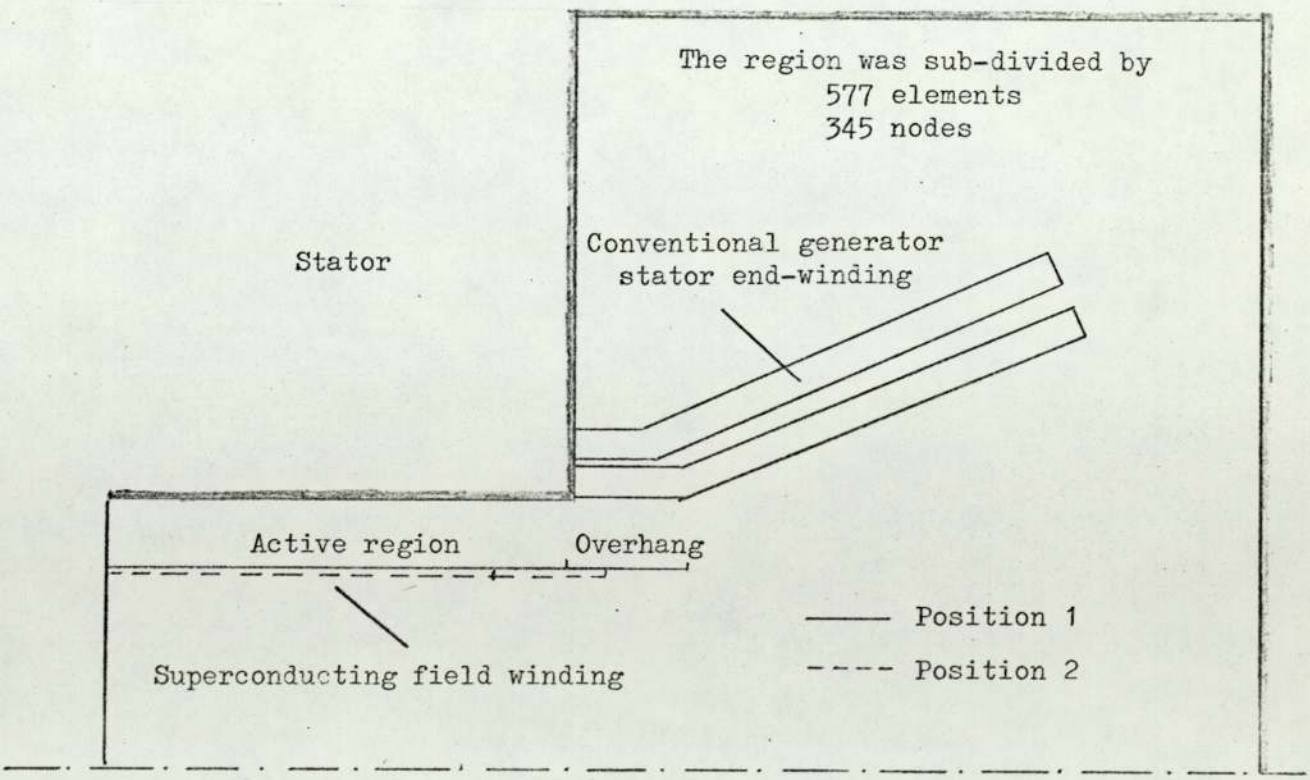

Fig. 6.17: End-region of a 660 MW rotating superconducting field generator

Fig. 6.18 compares the variation of flux densities normal to the stator core-surfaces for both rotor winding positions; it can be seen that the second rotor winding position reduces the flux density greatly. This is because the flux density normal to the core-end laminations are a consequence of fringing and flux due to the peripheral rotor end-winding currents. Thus, in Case 2, the fringe flux is reduced because the rotor winding ampere-turns fall off towards the stator core-end, and since the rotor end-winding is mainly inside the stator core, the core end-surface is effectively shielded from the fluxes due to the peripheral currents. The rotor winding position of Case 2 gives a slight reduction in generator voltage, since the average radial air-gap density is lower.

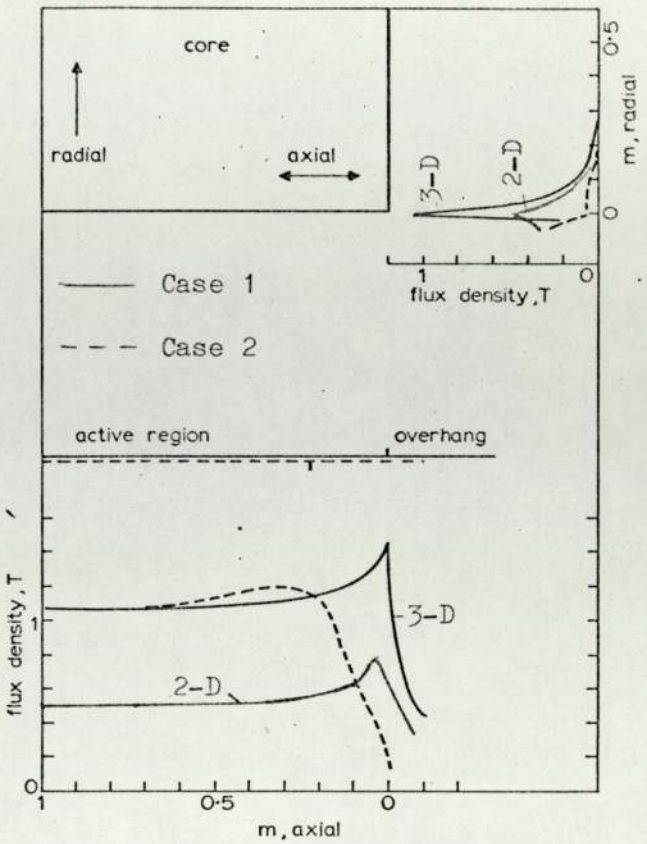

Fig. 6.18: Variation of flux density normal to the stator-end-surface (from discussion of Ref. (1))

The 2-dimensional approach was also used to determine the scalar potential distribution for Case 1, and the values of flux density normal to the stator core surfaces are compared in Fig. 6.18. It shows that there is a very large discrepancy between the two approaches: this is the result of neglecting peripheral leakage flux in the 2-dimensional approach. This can be explained by considering the transverse section at the axial centre of the generator, as shown in Fig. 6.19. Because the 2-dimensional method neglects the peripheral variation, the flux distribution is forced to that shown in Fig. 6.19. The actual distri-

bution, which can be derived analytically, is shown in Fig. 6.20:

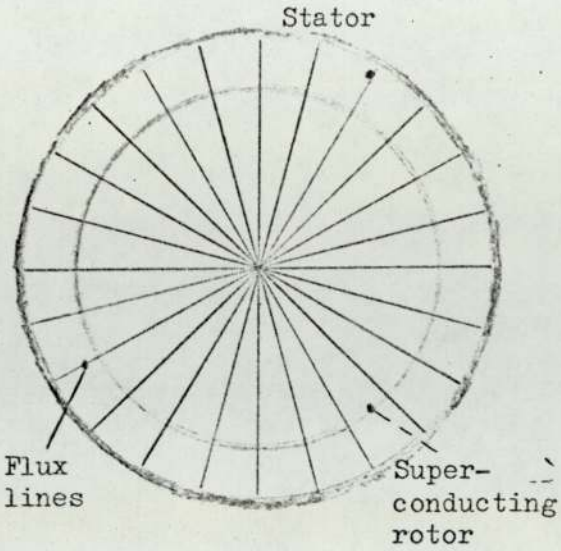

Fig. 6.19: Flux distribution in the core of a rotating superconducting generator, assuming no peripheral flux

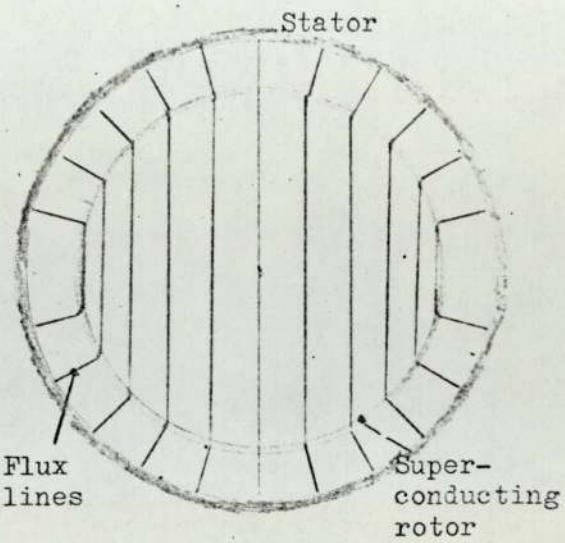

Fig. 6.20: Flux distribution in the core of a rotating superconducting generator, allowing for peripheral flux

6.5 660 MW Fully Slotless Generator

The effect of chamfering the corner of the stator-core-end of a fully slotless generator, so as to reduce the normally directed fluxes entering the core, was investigated by using the finite-element method.

Fig. 6.21 shows a simplified section of the end-region of a 660 MW fully slotless generator:

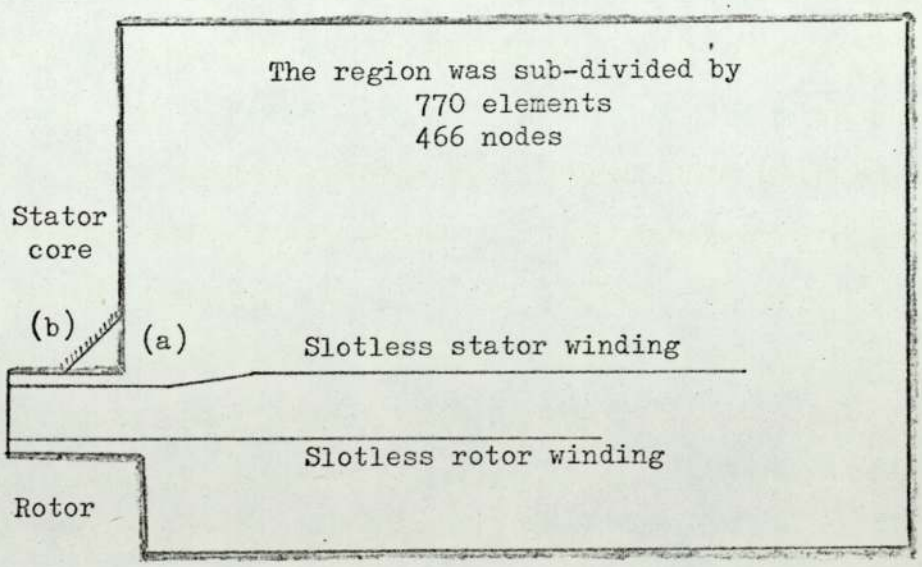

Fig. 6.21: End-region of a 660 MW fully slotless generator

Studies were made for the normal end-surface outline, and also with the corner chamfered. Fig. 6.22 compares the flux densities normal to the stator core, and shows that the effect of chamfering is to force the densities to decay more rapidly, though the peak values are not greatly reduced.

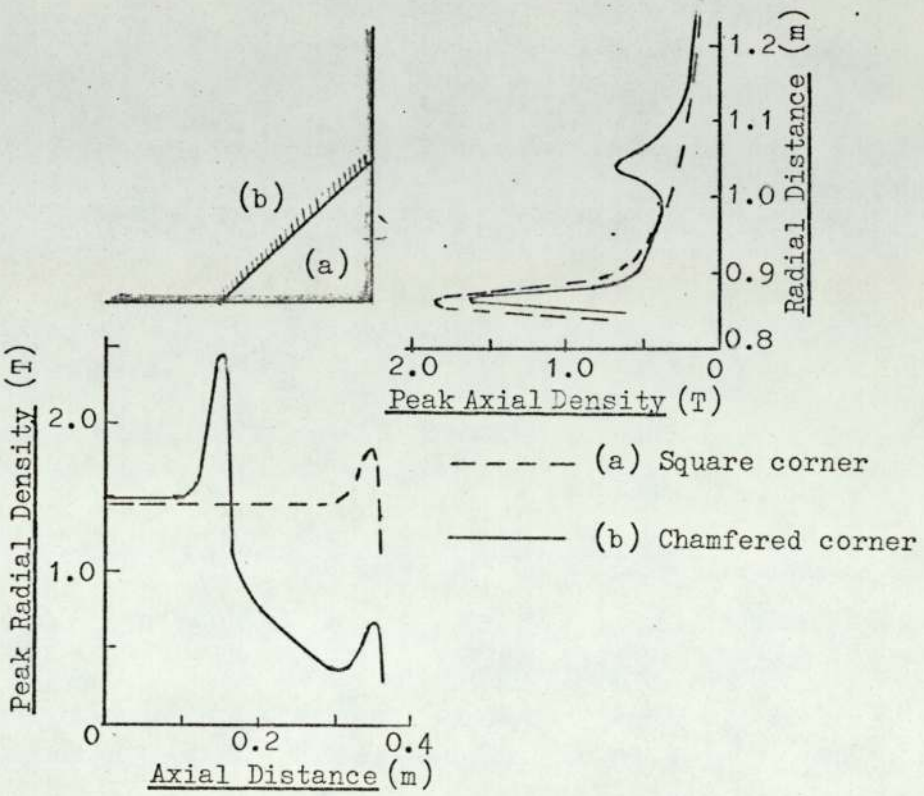

Fig. 6.22: Comparison of open-circuit flux densities normal to the stator-core end-surface of a 660 MW fully slotless generator, for (a) square corner, and (b) chamfered corner

6.6 Conclusions

The finite-element method has been used to determine the end-region flux distributions within two full-size turbine-generator end-regions, for which some measured values of flux density are available. In both cases the agreement with the measured values was good, giving confidence in the approach.

The method has also been applied to the end-region of a production 660 MW generator for several excitation conditions, and the load study showed how the core-end flux density, and hence heating, increases as the power factor varies from lag to lead.

The value of the method in design work on novel machines has been demonstrated by studies on a 660 MW generator with a superconducting field winding and on a 660 MW fully slotless generator.

CHAPTER 7

CONCLUSIONS

7.1 General

The previous chapters have detailed the development of the Finite-element Method for determining the flux distribution within the end-zone of turbine-generators, and have shown it to be an accurate and extremely flexible approach. This method allows for irregular boundary surfaces, mixed boundary conditions on the same surface, screens and clamping-plates, internal iron regions of finite permeability (such as the end-ring cover), and distributed windings. The advantages of the Finite-element Method compared with the Finite-difference Method (Section 1.4) have been demonstrated.

The major disadvantage of the method is the cost of data preparation: the following section discusses possible ways of reducing this, and further improvements in the treatment of eddy current effects and iron saturation.

7.2 Possible Improvements

7.2.1 Data preparation

For a solution by the Finite-element Method, the computer program requires the radial and axial co-ordinates of all nodes and the node numbers of the triangular elements: this results in a vast amount of data. So far, the data has been prepared by hand, but this has proved expensive, as shown by the example of the 660 MW generator study, where the manpower cost for preparing the data exceeded £150, compared with a solution cost of £5.

To reduce the cost of data preparation, it is desirable to generate the geometric and element data by a computer program. A program has been written, but has proved inadequate to cover all the variations in screen and winding shapes, rotor positional changes, etc., that are required when trying to optimise the end-

region design. A more general program could be written, but unless studies need to be made frequently the large development costs would outweigh possible savings in running cost.

A compromise between the hand-prepared and computer-generated data is to prepare the co-ordinates by using a "digitiser". A drawing of the end-region, with element division, is required: on positioning a probe over a node the co-ordinate data is punched onto paper tape. The element data can be prepared by hand, or generated automatically by a computer program: such a program has been written by Frederick et al[21]. Using this approach, the data for the 660 MW generator study could probably be produced for about £40.

7.2.2 Eddy current effects

The circulating eddy currents in conducting members have been simulated by an infinitely-conducting surface. One possible improvement being investigated is to express the flux density normal to the conducting surface in terms of the eddy current relationships beneath the surface. This would allow better representation of permeability, resistivity and frequency effects. Because the expressions are in terms of complex variables, a complex matrix solution is necessary. Providing computer storage is available, this could prove advantageous, as problems with a multi-layer winding representation or load excitation could be solved with one study.

7.2.3 Saturation effects

The saturation of the stator-core end-laminations can have a significant effect on the magnitude of the flux densities normal to the core-end-surface. At present, only the extreme boundary conditions of infinite permeability or infinite conductivity are possible. To incorporate approximately the saturation effect of the stator-core-end laminations into the end-zone solution would

require a knowledge of the ampere-turn distribution within the stator core. This is provided from a separate solution of scalar potential distribution in the stator core, using boundary fluxes calculated from the end-zone program: iteration between the "end-iron" and "end-zone" programs would continue until convergence of boundary potentials was obtained.

So far, only internal iron regions of finite permeability have been considered, but an approximation can be made for the non-linear magnetisation characteristics (by re-calculating the permeability of the elements) within the iron region, based upon the initial scalar potential distribution, and re-solving with the new values. This procedure would be repeated until convergence of all permeabilities is achieved.

7.3 Concluding Remarks

Although further improvements are possible, the method as described is a considerable advance on methods previously available to designers for the solution of end-zone problems. The method will also prove invaluable in the design of advanced forms of generators where previously existing techniques have been inadequate.

8. APPENDICES

8.1 Appendix I: Vector Potential Solution of the End-region Problem

8.1.1 Assumptions

In deriving the vector potential distribution within the end-region, the following assumptions were made:-

(i) All functions are sinusoidally distributed peripherally.

(ii) In the gap region, stator and rotor currents are represented by a thin current sheet on the stator and rotor surfaces.

(iii) All external iron boundaries are infinitely permeable.

(iv) Eddy currents are ignored.

8.1.2 Derivation of the end-region vector potential equations

The vector potential distribution in the end-region is described by Poisson's equation, which is:

$$\nabla^2 \bar{A} = -\mu_o \bar{J} \qquad \ldots\ldots\ldots (8.1)$$

From Assumption (i):

$$\bar{J} = \hat{J}_r \sin p\theta \times \underline{r} + \hat{J}_\theta \cos p\theta \times \underline{\theta} + \hat{J}_z \sin p\theta \times \underline{z}$$

$$\bar{A} = \hat{A}_r \sin p\theta \times \underline{r} + \hat{A}_\theta \cos p\theta \times \underline{\theta} + \hat{A}_z \sin p\theta \times \underline{z}$$

Also:

$$\text{Div } \bar{A} = 0$$

which in terms of the peak quantities is:

$$\frac{A_r}{r} + \frac{\partial A_r}{\partial r} - \frac{p}{r} A_\theta + \frac{\partial A_z}{\partial z} = 0 \qquad \ldots\ldots\ldots (8.2)$$

From the above the following component equations are derived (all vector potentials and current densities are peak values):-

$$\frac{\partial^2 A_r}{\partial r^2} + \frac{1}{r}\frac{\partial A_r}{\partial r} + \frac{\partial^2 A_r}{\partial z^2} - \frac{(1+p^2)}{r^2} A_r + \frac{2p}{r^2} A_\theta = -\mu_o J_r \quad \ldots (8.3)$$

$$\frac{\partial^2 A_\theta}{\partial r^2} + \frac{1}{r}\frac{\partial A_\theta}{\partial r} + \frac{\partial^2 A_\theta}{\partial z^2} - \frac{(1+p^2)}{r^2} A_\theta + \frac{2p}{r^2} A_r = -\mu_o J_\theta \quad \ldots (8.4)$$

$$\frac{\partial^2 A_z}{\partial r^2} + \frac{1}{r}\frac{\partial A_z}{\partial r} + \frac{\partial^2 A_z}{\partial z^2} - \frac{p^2}{r^2} A_z = -\mu_o J_z \qquad \ldots\ldots (8.5)$$

Eqn. (8.3) can be rearranged by substituting for Eqn. (8.2). The resulting equation is:

$$\frac{\partial^2 A_r}{\partial r^2} + \frac{3}{r}\frac{\partial A_r}{\partial r} + \frac{\partial^2 A_r}{\partial z^2} + \frac{(1 - p^2) A_r}{r^2} = -\mu_o J_r - \frac{2}{r}\frac{\partial A_z}{\partial z}$$

This can be more conveniently expressed by writing $A_r' = r A_r$, giving:

$$\frac{\partial^2 A_r'}{\partial r^2} + \frac{1}{r}\frac{\partial A_r'}{\partial r} + \frac{\partial^2 A_r'}{\partial z^2} - \frac{p^2}{r^2} A_r' = -\mu_o J_r r - \frac{2\partial A_z}{\partial z} \quad \ldots. (8.6)$$

Thus A_z can be solved directly from Eqn. (8.5), which then makes possible the solution of A_r' from Eqn. (8.6), because $\partial A_z/\partial z$ can be determined. A_θ is then obtained either from Eqn. (8.2) or Eqn. (8.4).

8.1.3 Numerical formulation

To solve Eqns. (8.4), (8.5) and (8.6) by the finite-element method, the end-region is divided into a number of triangular elements, with the radial and axial co-ordinates of the corners known. It is assumed in this analysis that the vector potential function is linearly distributed over each element, so that A within the element can be expressed as:

$$A = \frac{1}{2\Delta}\left\{(a_i + b_i r + c_i z)A_i + (a_j + b_j r + c_j z)A_j + (a_m + b_m r + c_m z)A_m\right\} \qquad \ldots\ldots (8.7)$$

where: $\dfrac{(a_i + b_i r + c_i z)}{2\Delta} = N_i$ (linear shape function)

also: $A = A_z$ or A_θ or A_r.

a_i, b_i, c_i, etc. are in terms of r and z as defined in Section 3.3.3.

The finite-element method is based upon the minimisation or maximisation of stored energy within the region considered,

and requires the establishment of a "functional", which can be regarded as describing the stored energy relationships within the end-region.

The derivation of the functional from the application of Euler's equation is detailed in Section 8.3.

The functionals corresponding to Eqns. (8.5), (8.6) and (8.4) respectively are:

$$X_z = \iint \left\{ \frac{r}{2} \left[\left(\frac{\partial A_z}{\partial r} \right)^2 + \left(\frac{\partial A_z}{\partial z} \right)^2 \right] + \frac{p^2}{2r} A_z^2 - \mu_o \, r \, J_z \, A_z \right\} dr \, dz \qquad \ldots\ldots\ldots (8.8)$$

$$X_r = \iint \left\{ \frac{r}{2} \left[\left(\frac{\partial A_r'}{\partial r} \right)^2 + r \left(\frac{\partial A_r'}{\partial z} \right)^2 \right] + \frac{p^2}{2r} A_r'^2 - \left(\mu_o \, J_r \, r + 2 \frac{\partial A_z}{\partial z} \right) r \, A_r' \right\} dr \, dz \qquad \ldots\ldots\ldots (8.9)$$

Before X_r can be solved, $\partial A_z / \partial z$ is required.

$$X_\theta = \iint \left\{ \frac{r}{2} \left[\left(\frac{\partial A_\theta}{\partial r} \right)^2 + \left(\frac{\partial A_\theta}{\partial z} \right)^2 \right] + \frac{(1 + p^2) A_\theta^2}{2r} - \left[\mu_o \, J_\theta + \frac{2p}{r^2} A_r \right] r \, A_\theta \right\} dr \, dz \qquad \ldots\ldots (8.10)$$

Before X_θ can be solved, A_r is required.

Since the procedure for obtaining the final numerical form of the equations is the same for A_z, A_r and A_θ, only the solution of A_z is described.

The numerical form of X_z is obtained by substituting Eqn. (8.7) into Eqn. (8.8).

X_z is extremised by differentiating with respect to the nodal vector potential for all triangles associated with the nodal vector potential:

i.e. $$\sum \frac{X_z^e}{A_{z_i}} = 0 \qquad \ldots\ldots (8.11)$$

For example, if node 6 is associated with elements 10, 50, 74, 96 and 107, then Eqn. (8.11) is written as:

$$\frac{\partial X_{z10}}{\partial A_{z_6}} + \frac{\partial X_{z50}}{\partial A_{z_6}} + \frac{\partial X_{z74}}{\partial A_{z_6}} + \frac{\partial X_{z96}}{\partial A_{z_6}} + \frac{\partial X_{z107}}{\partial A_{z_6}} = 0 \qquad \ldots\ldots (8.12)$$

Thus, when all nodes are operated on in accordance with Eqn. (8.11), a complete set of simultaneous equations is formed, defining the distribution of axial vector potential A_z.

A typical component part of Eqn. (8.11) is given as:

$$\begin{aligned}\frac{\partial X_z}{\partial A_{z_i}} = \frac{1}{4\Delta^2}\Big\{&(b_i^2\,\bar{r}\,\Delta + c_i^2\,\bar{r}\,\Delta + p^2 a_i^2 W + p^2 b_i^2\,\bar{r}\,\Delta \\ &+ p^2 c_i^2 S + 2p^2 b_i a_i \Delta + 2p^2 b_i c_i \bar{z}\,\Delta \\ &+ 2p^2 c_i a_i Q)A_{z_i} + (b_i b_j\,\bar{r}\,\Delta + c_i c_j\,\bar{r}\,\Delta + p^2 a_i a_j W \\ &+ p^2 b_i b_j\,\bar{r}\,\Delta + p^2 c_i c_j S + p^2 b_i a_j \Delta + p^2 a_i b_j \Delta \\ &+ p^2 b_i c_j\,\bar{z}\,\Delta + p^2 c_i b_j\,\bar{z}\,\Delta + p^2 c_i a_j Q \\ &+ p^2 a_i c_j Q)A_{z_j} + (b_i b_m\,\bar{r}\,\Delta + c_i c_m\,\bar{r}\,\Delta + p^2 a_i a_m W \\ &+ p^2 b_i b_m\,\bar{r}\,\Delta + p^2 c_i c_m S + p^2 b_i a_m \Delta + p^2 a_i b_m \Delta \\ &+ p^2 b_i c_m\,\bar{z}\,\Delta + p^2 c_i b_m\,\bar{z}\,\Delta + p^2 c_i a_m Q \\ &+ p^2 a_i c_m Q)A_{z_m} - (Y_{z_1})\Big\} \qquad \ldots\ldots (8.13)\end{aligned}$$

where: $$\bar{r} = \frac{r_i + r_j + r_m}{3}$$

$$\bar{z} = \frac{z_i + z_j + z_m}{3}$$

$$Y_{z_1} = + \iint \frac{\partial A_z}{\partial A_{z_i}} \mu_o\, r\, J_z\, dr\, dz$$

These terms are only present when the node considered lies on or within the stator or rotor winding areas.

S, W and Q are areas of integration for the functions described in Section 8.4.

8.1.4 Boundary conditions

Because the air-gap has to extend back into the core, a problem arises in defining boundary condition. In Okuda's[15] work, the core end-surface and rotor were taken as an infinitely permeable continuous surface. This allows the method of images to be applied, and leads to the simple condition that $A_z = 0$. However, the present study is particularly concerned with fluxes near the gap end, and thus it is unwise to make this assumption.

Equating the boundary in full gives:

(i) Radial infinitely permeable iron surfaces

(e.g. stator end-surface)

$$B_r = \frac{p}{r} A_z - \frac{\partial A_\theta}{\partial z} = 0 \quad \text{(from } B = \text{curl } A\text{)} \qquad \ldots\ldots\ldots (8.14)$$

$$B_\theta = \frac{\partial A_r}{\partial z} - \frac{\partial A_z}{\partial r} = 0 \qquad \ldots\ldots\ldots (8.15)$$

(ii) Axial infinitely permeable iron surfaces

(e.g. stator bore)

$$B_z = \frac{1}{r}\left\{\frac{\partial}{\partial r}(r A_\theta) - p A_r\right\} = 0 \qquad \ldots\ldots\ldots (8.16)$$

$$B_\theta = \frac{\partial A_r}{\partial z} - \frac{\partial A_z}{\partial r} = 0 \qquad \ldots\ldots\ldots (8.17)$$

The extreme boundary of the air-gap can be regarded as having the radial flux component only present, i.e. $A_r = A_\theta = 0$, and A_z is calculated from 2-dimensional theory.

The conditions above do not allow a solution to be obtained. It appears that the assumption made by Okuda is necessary for the solution to be formulated.

The assumption made is that the stator and rotor end-surfaces are infinitely permeable and form one continuous straight boundary. Based on this assumption, the mirror image currents can be set up as shown in Fig. 8.1:

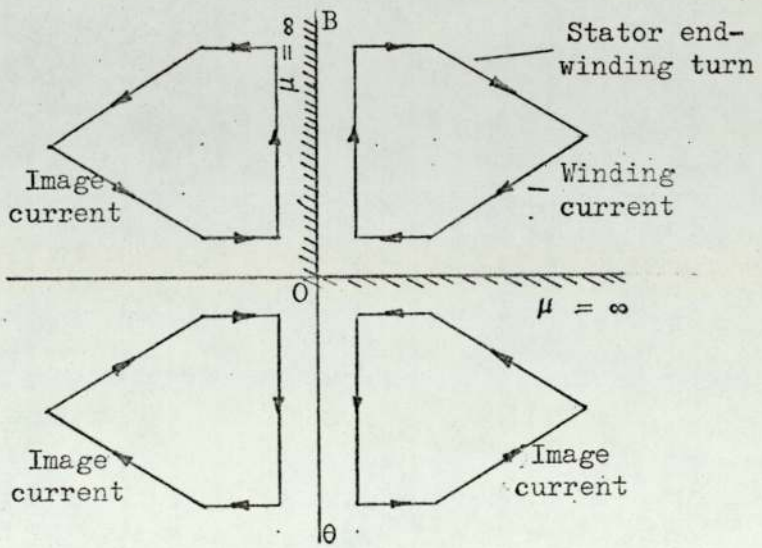

Fig. 8.1: Mirror image currents

Thus on surface OB the axial component of the vector potential vanishes, giving $A_z = 0$. Similarly, on the axial surfaces the radial component vanishes, giving $A_r = 0$.

This leads directly to the following boundary conditions:-

(a) Radial surfaces (core end-surface, etc.)

$$A_z = 0$$

$$\frac{\partial A_\theta}{\partial z} = 0 \qquad \text{... from (8.14)}$$

$$\frac{\partial A_r}{\partial z} = 0 \qquad \text{... from (8.15)}$$

(b) Axial surfaces (rotor shaft, etc.)

$$\frac{\partial A_z}{\partial r} = 0 \qquad \text{... from (8.17)}$$

$$\frac{\partial}{\partial r}(r A_\theta) = 0 \qquad \text{... from (8.16)}$$

$A_r = 0$

8.1.5 Advantages of vector potential

Current in the stator and rotor windings can accurately be represented in amplitude and distribution; also, the actual thickness of the winding can be considered.

8.1.6 Disadvantages of vector potential

(i) Three solutions are required for A_z, A_r and A_θ.

(ii) To derive A_r, the term $\partial A_z/\partial z$ is required; thus any error in the A_z solution is transferred to the A_r and A_θ solutions. To reduce this effect, a finer mesh would be required, thus increasing the store requirements.

(iii) The boundaries on the radial and axial surfaces have to be approximated so that a direct solution is possible. The effect of this assumption is not known.

(iv) Although the winding currents are accurately represented, the considerable amount of calculation makes the solution costly.

8.2 Appendix II: Flux Density Solution of End-region Problem

8.2.1 Derivation of end-region flux density equations

Because of the difficulty of defining boundary conditions for the vector potential solution, the problem was formulated in terms of flux density, for which boundary conditions are much more definite. The equation describing the flux density in the end-region is:

$\text{Div } \bar{B} = 0$

and expanding gives:

$$\frac{B_r}{r} + \frac{\partial B_r}{\partial r} + \frac{1}{r}\frac{\partial B_\theta}{\partial \theta} + \frac{\partial B_z}{\partial z} = 0$$

Also: $\text{curl } \bar{B} = \mu_o \bar{J}$ (in the winding regions)

This gives the following relationships (all flux densities and current densities are peaks of quantities varying

sinusoidally in the peripheral direction):-

$$\frac{\partial^2 B_z}{\partial r^2} + \frac{\partial^2 B_z}{\partial z^2} + \frac{1}{r}\frac{\partial B_z}{\partial r} - \frac{p^2}{r^2} B_z = \frac{p}{r} \mu_o J_r - \mu_o \frac{\partial J_\theta}{\partial r} - \frac{1}{r} \mu_o J_\theta \quad \ldots\ldots (8.18)$$

and if $B_\theta' = r B_\theta$:

$$\frac{\partial^2 B_\theta'}{\partial r^2} + \frac{1}{r}\frac{\partial B_\theta'}{\partial r} + \frac{\partial^2 B_\theta'}{\partial z^2} - \frac{p^2}{r^2} B_\theta' = \mu_o \frac{\partial}{\partial r}(J_z r) + \mu_o J_z - \mu_o r \frac{\partial J_r}{\partial z} \quad \ldots\ldots (8.19)$$

and if $B_r' = r B_r$:

$$\frac{\partial^2 B_r'}{\partial r^2} + \frac{1}{r}\frac{\partial B_r'}{\partial r} + \frac{\partial^2 B_r'}{\partial z^2} - \frac{p^2}{r^2} B_r' = \mu_o r \frac{\partial J_\theta}{\partial z} - p \mu_o J_z - 2\frac{\partial B_z}{\partial z} \quad \ldots\ldots (8.20)$$

These equations are similar to Eqns. (8.3) - (8.5) of Section 8.1, and thus the solution procedure is the same.

8.2.2 Numerical formulation

The flux density is assumed to vary linearly over the triangular elements, thus giving:

$$B = \frac{1}{2\Delta}\left\{(a_i + b_i r + c_i z) B_i + (a_j + b_j r + c_j z) B_j + (a_m + b_m r + c_m z) B_m\right\} \quad \ldots\ldots (8.21)$$

where: $B = B_z$ or B_r' or B_θ'.

The functionals for Eqns. (8.18) - (8.20) are:

$$X_z = \iint \left\{\frac{r}{2}\left[\left(\frac{\partial B_z}{\partial r}\right)^2 + \left(\frac{\partial B_z}{\partial z}\right)^2\right] + \frac{p^2}{2r} B_z^2 - \mu_o J_\theta B_z + p \mu_o J_r B_z - \mu_o r \frac{\partial J_\theta}{\partial r} B_z\right\} dr\, dz \quad \ldots\ldots (8.22)$$

$$X_r = \iint \left\{\frac{r}{2}\left[\left(\frac{\partial B_r'}{\partial r}\right)^2 + \left(\frac{\partial B_r'}{\partial z}\right)^2\right] + \frac{p^2}{2r} B_r'^2 - p \mu_o r J_z B_r' + \mu_o r^2 \frac{\partial J_\theta}{\partial z} B_r' - 2r \frac{\partial B_z}{\partial z} B_r'\right\} dr\, dz \quad \ldots\ldots (8.23)$$

$$X_\theta = \iint \left\{ \frac{r}{2} \left[\left(\frac{\partial B_\theta'}{\partial r} \right)^2 + \left(\frac{\partial B_\theta'}{\partial z} \right)^2 \right] + \frac{p^2}{2r} B_\theta'^2 + \mu_o \, r \, J_z \, B_\theta' \right.$$

$$\left. - \mu_o \, r^2 \frac{\partial J_r}{\partial z} B_\theta' + \mu_o \, r \frac{\partial}{\partial r} (r \, J_z) \, B_\theta' \right\} dr \, dz \quad \ldots\ldots (8.24)$$

Eqns. (8.22) - (8.24) are reduced to the finite-element form by substituting for Eqn. (8.21), and extremising as described in Section 8.1.3.

8.2.3 Boundary conditions

(i) Axial surfaces ($\mu = \infty$)

$$B_z = B_\theta = 0$$

$$\therefore \text{ from Div } B = 0, \frac{\partial}{\partial r} (r \, B_r) = 0$$

$$\therefore \frac{\partial B_r'}{\partial r} = 0$$

(ii) Radial surfaces ($\mu = \infty$)

$$B_r' = B_\theta = 0$$

$$\therefore \frac{\partial B_z}{\partial z} = 0$$

(iii) Air-gap boundary line

$$B_z = B_\theta = 0$$

B_r' is determined from 2-dimensional theory for the flux density variation between two concentric cylinders.

(iv) Corners on outside boundaries

(a) Internal corners: Both B_r' and B_z are taken as zero.

(b) External corners: Since the values of B_r' and B_z cannot be defined, values are chosen consistent with saturation levels at the corners.

8.2.4 Advantages of the flux density solution

(i) Flux density conditions on the outer boundaries can be specified exactly, except at the corner points.

(ii) Current sources can be accurately represented.

8.2.5 Disadvantages of the flux density solution

(i) When deriving B_r', the axial gradient of B_z is required, thus any errors in B_z are transmitted to B_r'.

(ii) In Eqn. (8.18), for B_z the R.H. side contains a term $\partial J_\theta/\partial r$. The distribution of this term is such that the derivative gives a zero value over the radial width of the winding, but an infinite value on the boundaries of the winding. This leads to difficulty in the finite-element formulation, and it is necessary to approximate the true distribution by one for which the gradient is finite on the winding edges. This involves extra computation.

8.3 Appendix III: Determination of the "Functional" from Euler's Equation

It is required to find the functional, X, corresponding to the differential equation (2.7):

$$\frac{\partial^2 U'}{\partial r^2} + \frac{1}{r}\frac{\partial U'}{\partial r} + \frac{1}{r^2}\frac{\partial^2 U'}{\partial \theta^2} + \frac{\partial^2 U'}{\partial z^2} = 0$$

For convenience, the above equation can be written as:

$$r\frac{\partial^2 U'}{\partial r^2} + \frac{\partial U'}{\partial r} + \frac{1}{r}\frac{\partial^2 U'}{\partial \theta^2} + r\frac{\partial^2 U'}{\partial z^2} = 0 \qquad \ldots\ldots (8.25)$$

The general form of the functional is as follows:-

$$X = \iiint_V (Q)\, dr\, dz\, d\theta \qquad \ldots\ldots (8.26)$$

$$\text{where: } Q = f\left\{r,\ z,\ \theta,\ U',\ \frac{\partial U'}{\partial r},\ \frac{\partial U'}{\partial z},\ \frac{\partial U'}{\partial \theta}\right\} \qquad \ldots\ldots (8.27)$$

From Euler's theorem, the necessary condition for X to be the functional for Eqn. (8.25) is that Eqn. (8.28) should be identical to the differential equation to be solved, viz. (8.25):

$$\frac{\partial}{\partial r}\left[\frac{\partial Q}{\partial\left(\frac{\partial U'}{\partial r}\right)}\right] + \frac{\partial}{\partial \theta}\left[\frac{\partial Q}{\partial\left(\frac{\partial U'}{\partial \theta}\right)}\right] + \frac{\partial}{\partial z}\left[\frac{\partial Q}{\partial\left(\frac{\partial U'}{\partial z}\right)}\right] - \frac{\partial Q}{\partial U'} = 0 \quad \ldots. (8.28)$$

Comparing Eqns. (8.28) and (8.25) term-by-term, it follows that:

$$\frac{\partial}{\partial r}\left[\frac{\partial Q}{\partial\left(\frac{\partial U'}{\partial r}\right)}\right] = r\frac{\partial^2 U'}{\partial r^2} + \frac{\partial U'}{\partial r} = \frac{\partial}{\partial r}\left\{r\frac{\partial U'}{\partial r}\right\} \qquad \ldots\ldots\ldots (8.29)$$

$$\frac{\partial}{\partial \theta}\left[\frac{\partial Q}{\partial\left(\frac{\partial U'}{\partial \theta}\right)}\right] = \frac{1}{r}\frac{\partial^2 U'}{\partial \theta^2} = \frac{1}{r}\frac{\partial}{\partial \theta}\left\{\frac{\partial U'}{\partial \theta}\right\}$$

$$\frac{\partial}{\partial z}\left[\frac{\partial Q}{\partial\left(\frac{\partial U'}{\partial z}\right)}\right] = r\frac{\partial^2 U'}{\partial z^2} = r\frac{\partial}{\partial z}\left\{\frac{\partial U'}{\partial z}\right\}$$

$$\frac{\partial Q}{\partial U'} = 0$$

Thus the values of Q (say, Q_1, Q_2, Q_3 and Q_4) for all four parts of Eqn. (8.25) are:

$$\frac{\partial Q_1}{\partial\left(\frac{\partial U'}{\partial r}\right)} = r\frac{\partial U'}{\partial r}$$

$$\therefore \quad Q_1 = \frac{r}{2}\left\{\frac{\partial U'}{\partial r}\right\}^2$$

Similarly:

$$Q_2 = \frac{1}{2r}\left\{\frac{\partial U'}{\partial \theta}\right\}^2$$

$$Q_3 = \frac{r}{2}\left\{\frac{\partial U'}{\partial z}\right\}^2$$

$$Q_4 = 0$$

then $Q = Q_1 + Q_2 + Q_3 + Q_4$, and a check will indicate that this value of Q satisfies the Euler condition.

From Eqn. (8.26) the required functional becomes:

$$X = \iiint \left\{ \frac{r}{2}\left[\left(\frac{\partial U'}{\partial r}\right)^2 + \left(\frac{\partial U'}{\partial z}\right)^2\right] + \frac{1}{2r}\left(\frac{\partial U'}{\partial \theta}\right)^2 \right\} dr\, dz\, d\theta.$$

8.4 Appendix IV: Evaluation of Area Integrals

When formulating the numerical expressions of the extremised functional equation, (3.10), terms arise which are of the form:

$$\iint f(r, z)\, dr\, dz$$

In deriving the final numerical equations, it is necessary to evaluate these functions over the area of the triangle being considered.

To describe the integration procedure, the function

$$f(r, z) = \frac{1}{r}$$

is evaluated,

i.e. $$W = \iint \frac{1}{r}\, dr\, dz$$

The integration over the area of the triangle is performed by taking each side in turn and adding their contributions. (The sequence of integration must be consistent with that used for deriving the general distribution of scalar potential over the triangle, i.e. clockwise. If this is not done, a sign error will appear, giving incorrect numerical equations.)

Considering side ij (Fig. 8.2):

This line can be expressed in terms of the nodal co-ordinates,

i.e. $z = a + br$

where: $$a = -\frac{a_m}{c_m} = -\frac{(r_i z_j - r_j z_i)}{(r_j - r_i)}$$

$$b = -\frac{b_m}{c_m} = -\frac{(z_i - z_j)}{(r_j - r_i)}$$

$$\therefore \quad W = \iint \frac{1}{r}\, dr\, dz$$

$$= \int_{r_i}^{r_j} \frac{z}{r}\, dr$$

$$= \int_{r_i}^{r_j} \frac{1}{r}(a + br)\, dr$$

$$= \Big[a \log_e r + b r \Big]_{r_i}^{r_j}$$

$$= -\frac{a_m}{c_m}\Big[\log_e r_j - \log_e r_i \Big] - b_m$$

$$\therefore \quad W = \frac{a_m}{c_m} \log_e \frac{r_i}{r_j} - (z_i - z_j)$$

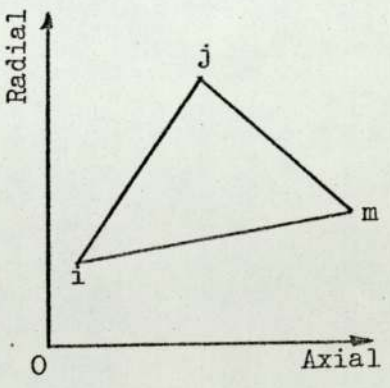

Fig. 8.2: Triangle over which the area integrals are calculated

This procedure is repeated for the sides jk and ki respectively, and these components added to the expression for side ij, giving:

$$W = \frac{a_m}{c_m} \log_e \frac{r_i}{r_j} + \frac{a_i}{c_i} \log_e \frac{r_j}{r_m} + \frac{a_j}{c_j} \log_e \frac{r_m}{r_i}$$

(Since $\{(z_i - z_j) + (z_j - z_k) + (z_k - z_i)\} = 0.$)

The other functions arising in the numerical equations are evaluated, using the same procedure, and are as follows:-

$$Q = \iint \frac{z}{r} \, dr \, dz$$

$$= -\left\{\frac{a_m^2}{2c_m^2} \log_e \frac{r_i}{r_j} + \frac{a_i^2}{2c_i^2} \log \frac{r_j}{r_m} + \frac{a_j^2}{2c_j^2} \log_e \frac{r_m}{r_i}\right\}$$

$$+ \left\{\frac{b_m^2}{4c_m} (r_i + r_j) + \frac{a_m b_m}{c_m} + \frac{b_i^2}{4c_i} (r_j + r_m) + \frac{a_i b_i}{c_i}\right.$$

$$\left. + \frac{b_j^2}{4c_j} (r_m + r_i) + \frac{a_j b_j}{c_j}\right\}$$

and $$S = \iint \frac{z^2}{r} \, dr \, dz$$

$$= \frac{a_m^3}{3c_m^3} \log_e \frac{r_i}{r_j} + \frac{a_i^3}{3c_i^3} \log_e \frac{r_j}{r_m} + \frac{a_j^3}{3c_j^3} \log_e \frac{r_m}{r_i}$$

$$- \left\{\frac{b_m}{c_m^2}\left[\frac{b_m^2}{9} (r_i^2 + r_i r_j + r_j^2) + \frac{a_m b_m}{2} (r_i + r_j) + a_m^2\right]\right.$$

$$+ \frac{b_i}{c_i^2}\left[\frac{b_i^2}{9} (r_j^2 + r_j r_m + r_m^2) + \frac{a_i b_i}{2} (r_j + r_m) + a_i^2\right]$$

$$\left. + \frac{b_j}{c_j^2}\left[\frac{b_j^2}{9} (r_m^2 + r_m r_i + r_i^2) + \frac{a_j b_j}{2} (r_m + r_i) + a_j^2\right]\right\}$$

8.5 Appendix V: Two-layer Representation of the Stator End-winding

Section 3.4.1.1 has shown how a single current sheet can be used to represent the end-winding, but for more accurate studies it is possible to represent the winding by two current sheets, one for each winding layer. A difficulty arises because the mmf distributions set up by each current sheet are displaced peripherally relative to each other, although their

magnitudes are the same. Thus a single solution is not possible, as the quasi-3-dimensional study does not allow for a peripheral phase shift in potentials at different positions throughout the end-region.

This difficulty is overcome by resolving the individual mmfs into sine and cosine components, and solving for these distributions separately. The final solution is obtained by adding vectorially the potentials from the two numerical studies.

The potential difference, ΔU, across the magnetically insulating shell, which represents the current sheet, is given directly from the mmf distribution relationships.

These equations are given by Nomura, but for convenience they are listed below:

The layout of a typical end-turn is shown in Fig. 8.3, and only the fundamental component of potential difference is considered.

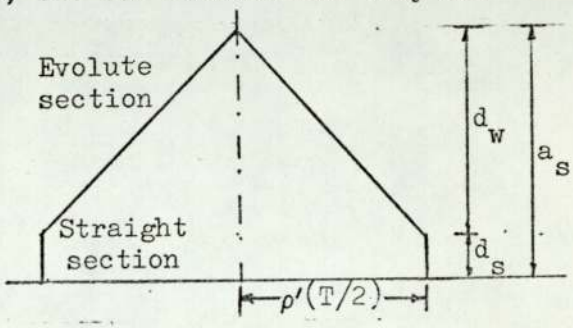

Fig. 8.3: Stator end-winding turn

(a) Cosine potential difference distribution

(i) Straight section: $0 < z \leq d_s$

$$\Delta U = \frac{1.35 \times I_{rms} \times T_{ph} \times K_d}{poles} \cos (1 - \rho') \frac{\pi}{2}$$

(ii) Evolute section: $d_s < z \leq a_s$

$$\Delta U = \frac{1.35 \times I_{rms} \times T_{ph} \times K_d}{poles} \cos \frac{\pi}{2} \left\{ \frac{\rho' (z - a_s)}{dw} + 1 \right\}$$

(b) Sine potential difference distribution

(i) Straight section: $0 < z \leq d_s$

$$\Delta U = \pm \frac{1.35 \times I_{rms} \times T_{ph} \times K_d}{poles} \sin (1 - \rho') \frac{\pi}{2}$$

(ii) Evolute section: $d_s < z \leq a_s$

$$\Delta U = \pm \frac{1.35 \times I_{rms} \times T_{ph} \times K_d}{poles} \sin \frac{\pi}{2} \left\{ \frac{\rho' (z - a_s)}{dw} + 1 \right\}$$

(The plus and minus signs apply to the inner and outer layers respectively.)

REFERENCES

1. Lorch, H.O. "Feasibility of turbo-generator with super-conducting rotor and conventional stator", Proc. I.E.E., 1973, 120, (2), p.221.

2. Smith, R.T. "End component of armature leakage reactance of round-rotor generators", Trans. Amer. Inst. Elect. Engrs., 1958, 77, Pt. III, p.636.

3. Honsinger, V.B. "Theory of end-winding leakage reactance", ibid, 1959, 78, Pt. III, p.417.

4. Honsinger, V.B. "Measurement of end-winding leakage reactance, ibid, 1959, 78, Pt. III, p.426.

5. Reece, A.B.J. and Pramanik, A. "Calculation of the end-region field of a.c. machines", Proc. I.E.E., 1965, 112, (7), p.1355.

6. Ashworth, D.S. and Hammond, P. "The calculation of the magnetic field of rotating machines. Pt. 2 - The field of turbo-generator end-windings", ibid, 1961, 108A, p.527.

7. Tegopoulos, J.A. "Determination of the magnetic field in the end zone of turbine generators", I.E.E.E. Trans. Power Apparatus Syst. (U.S.A.), 1963, 82, p.562.

8. Lawrenson, P.J. "The magnetic field of the end-windings of turbo-generators", Proc. I.E.E., 1961, 108A, p.538.

9. Tegopoulos, J.A. "Flux impinging on the end plate of turbine generators", A.I.E.E. Trans., Pt. III, 1962, 81, p.700.

10. Darrieus, G. "Determination and plotting of three-dimensional fields. Application to end windings, especially turbo-alternators", Rev. Gen. Electr. (France), 1967, 76, p.333.

11. Winchester, R.L. "Stray losses in the armature end iron of large turbine generators", Trans. Amer. Inst. Elect. Engrs., 1955, 74, Pt. III, p.384.

12. Hawley, R., Edwards, I.M., Healton, J.M. and Stoll, R.L. "Turbogenerator end region magnetic fields - Qualitative prediction by field plotting", Proc. I.E.E., 1967, 114, (8), p.1107.

13. Oberretl, K. "Magnetic fields, eddy currents, and losses, taking the variable permeability into account", I.E.E.E. Trans. Power Apparatus Syst. (U.S.A.), 1969, 88, p.1646.

14. Sarma, M.S., Wilson, J.C., Lawrenson, P.J. and Jokl, A.L. "End-winding leakage of high-speed alternators by three-dimensional field determination", ibid, 1971, 90, p.465.

15. Okuda, H. "Calculation of magnetic field distribution in the end zone of a generator winding", J. Inst. Electr. Jap. (Japan), 1969, 89, p.27.

16. Nomura, T. "Calculation of the magnetic field in the end zone of turbine generators", I.E.E.E., Paper CP 513-PWR, 1971.

17. Franklin, P. 'Methods of Advanced Calculus', McGraw-Hill Book Co., 1944.

18. Tegopoulos, J.A. "Current sheets equivalent to end winding currents of turbine generator stator and rotor", A.I.E.E. Trans., Pt. III, 1962, 81, p.695.

19. Dreyfus, L. "The calculation of eddy current losses in non-magnetic clamping plates of large turbo-generators", Compte. Rendus de Congres International d'Electricite, 1932, 1, p.273.

20. Jenning, A. "A compact storage scheme for the solution of symmetric linear simultaneous equations", Comput. J. (G.B.), 1966, 9, p.281.

21. Frederick, C.O., Wong, Y.C. and Edge, F.W. "Two-dimensional automatic mesh generation for structural analysis", Int. J. Numer. Methods Eng., 1970, 2, p.133.